Ab Initio Molecular Vibrations Enable Reliable Exciton Dynamics Simulations

Ab Initio Molecular Vibrations Enable Reliable Exciton Dynamics Simulations

A DISSERTATION PRESENTED
BY
SAMUEL MELTZER BLAU
TO
THE DEPARTMENT OF CHEMISTRY AND CHEMICAL BIOLOGY

IN PARTIAL FULFILLMENT OF THE REQUIREMENTS
FOR THE DEGREE OF
DOCTOR OF PHILOSOPHY
IN THE SUBJECT OF
CHEMICAL PHYSICS

HARVARD UNIVERSITY
CAMBRIDGE, MASSACHUSETTS

DECEMBER 2017

Dissertation Advisor: Professor Alán Aspuru-Guzik Samuel Meltzer Blau

Ab Initio Molecular Vibrations Enable Reliable Exciton Dynamics Simulations

Abstract

In 2007, Engel's proposal of long-lived coherence in photosynthesis precipitated substantial efforts to understand the role of quantum effects in biology. While much progress has been made in the last decade, the timescale, type, and functional importance of coherence coupled to thermal vibrations remains poorly understood.

In this dissertation, I simulate and disentangle excitation dynamics in the presence of complex vibrational environments for a light-harvesting protein and a synthetic dimer, both of which are controversial. I develop new techniques and leverage substantial computational resources to employ accurate *ab initio* methods that were previously considered prohibitively expensive.

I examine phycobiliprotein PC645, a light-harvesting complex found in cryptophyte algae and, contrary to previous literature, I show that the protein's key function proceeds via an incoherent mechanism. For the first time, I extract spectral densities from *ab initio* molecular dynamics (AIMD) combined with density functional theory excited state calculations. I obtain the first-ever quantitative reproduction of experimental linear spectra from first principles for a pigment-protein complex and find that stronger than expected environmental vibrations control the pathways of excitation transport. I generalize my findings using a model vibronic dimer, defining regimes of vibronic transport and demonstrating that biological systems are outside of the coherent regime.

I then investigate three controversial synthetic fluorescein heterodimers that were engineered with the goal of providing a model system for understanding coherent energy

transfer in multichromophoric systems. I extract Hamiltonians and spectral densities using AIMD and find electronic couplings an order of magnitude larger than previously thought. I calculate coherence dynamics and a trajectory of 2D spectra and demonstrate that electronic coherence persists for just 100-150 femtoseconds, after which long-lived vibrationally driven coherences persist for hundreds of femtoseconds. Thus, I resolve the controversy and confirm that while electronic coherence can be engineered in artificial molecular systems, it will not persist for a picosecond, as previously claimed.

Leveraging *ab initio* methods, I have extracted mechanistic detail and clarified the presence and functional relevance of coherence in two controversial systems. However, significant experimental and computational challenges remain to enable the rational design of next-generation materials for light-harvesting and energy transport.

Contents

I dedicate this dissertation to my father Leonard Blau

who would have loved nothing more than to see his son become a Dr.

Acknowledgments

My five-and-a-half years in graduate school have been incredibly enjoyable and intellectually satisfying. I feel as though a truckload of knowledge has been funneled into my brain, and there have been so many wonderful people that helped to prepare me and have supported me throughout the journey.

The first person that I have to thank is my advisor, Professor Alán Aspuru-Guzik. I still remember the first time I met Alán at Haverford, because we immediately clicked. Since that first encounter, we've always had such a warm and natural connection, and we consistently seem to be on the same mental wavelength. I think that I have had an abnormally positive graduate school experience due to my wonderful relationship with Alán, and I am incredibly grateful for that. He has struck the perfect balance between supporting me and challenging me, giving me scientific direction and forcing me to come up with my own, and being both my boss and my mentor. I know that we will stay in touch and that this is just the beginning of a lifelong friendship.

Of course, I never would have met Alán or been so ready to tackle the immense task of a PhD without the fantastic scientific foundation instilled in me by two undergraduate advisors, Professor Alex Norquist and Professor Josh Schrier. Alex and Josh gave me the confidence that was critical to my graduate success because they always treated me like an equal and empowered me to direct much of my own undergraduate research. They perfectly fostered my scientific passion, and along the way somehow managed to put up with my very immature antics as an 18- and 19-year-old. I could not have asked for a better environment to launch my scientific career, and it has been such a treat catching up in person each time I've been back at Haverford.

I must also extend my sincere thanks to Professor Tim Kaxiras and Professor Rick Heller for being part of my graduate advising committee throughout my PhD. Despite

their packed schedules and many responsibilities, they took the time to listen to my research updates and provide crucial feedback that helped me along my journey. A special thanks to Professor Dudley Herschbach, who agreed to fill a last-minute vacancy on my defense committee, for which I am incredibily grateful.

My graduate school experience was also enriched tremendously by the postdoctoral fellows and other graduate students in my lab with whom I worked every day. Thomas Markovich, Nicolas Sawaya, and I all started in Alán's lab at the same time, and it was such a pleasure to have them as friends and colleagues throughout this journey. Thomas got me interested in going on long bike rides, which ended up being crucial to maintaining my sanity throughout graduate school, and he also pushed me to be a better scientist by showing me what is possible if you are truly relentless. Nico was a constant source of positivity around the lab, and was always available to grab a drink or to be a sounding board for a wacky idea or point of confusion. Martin Forsythe joined the lab in my second year of graduate school and quickly became another close friend and colleague. Besides being a brilliant and hard-working scientist, Martin is one of the most thoughtful and honest people I've ever met, and for that I've always looked up to him. Other graduate students in the Aspuru-Guzik group that were particularly important to my experience include Ryan Babbush, Jarrod McClean, Stephanie Valleau, Jacob Sanders, Joey Goodknight, Adrian Jinich, Jennifer Wei, and Florian Hase. My sincere thanks to them and to all of the other graduate students who made this such a great place to do science.

Of course I didn't only interact with graduate students in my lab but also became great friends with students in other labs as well. I am particularly thankful for my friendships with Micah Maetani, Jeff Bessen, Tristan Owens, Katie Schaefer, and Fred Rubino. They ensured that I didn't stay trapped in the bubble of my lab and helped me stay sane through games, outings, and wonderful conversations. I also want to acknowledge Julia Szabo and John Majoris, my two best Boston-based friends outside of Harvard who I saw almost every weekend throughout my PhD. I will always remember their love and support,

frequent brainstorming sessions, and many wonderful adventures over the last five years.

I am also incredibly grateful for the funding I received through my Department of Energy Computational Sciences Graduate Fellowship as well as the connections and friendships I formed at the yearly conferences. I am particularly thankful for the mentorship of Jeff Hammond, who advised my research practicum at Argonne National Lab and taught me everything I know about coupled cluster quantum chemistry while also helping me secure essential computer time for my main research projects.

Returning to my lab, I owe a unique debt of gratitude to the postdoctoral fellows that I worked with throughout graduate school. While Alán provided the overarching vision, and other graduate students joined me in the scientific trenches, several postdocs provided essential direct scientific guidance. Dr. John Parkhill took me under his wing when I first arrived at Harvard, and pushed me forward as a scientist and a programmer, helping me to build a solid foundational understanding of open quantum systems that was essential to the rest of my graduate work. Dr. Christoph Kreisbeck mentored me on and off throughout graduate school, and his expertise in HEOM enabled much of my research. While Dr. Dmitrij Rappoport didn't mentor me quite as directly as John or Christoph, his expertise in TDDFT was critical at multiple points throughout my PhD.

And then there's Dr. Doran Bennett. When Doran joined the group roughly two years ago, I couldn't have imagined how much he would shape me as a scientist. At the time, I had laid the foundation for what would become the core of this dissertation, but confusing data analysis, a detour through coupled cluster with Jeff Hammond, demanding classes and the departure of both John and Christoph combined to knocked me off course and send me along some fruitless research directions. Doran helped me find my bearings once again, and his expertise in spectroscopy and photosynthetic mechanisms was exactly what I needed to uncover the gems of understanding and impact that had been buried in the mountains of data I had produced. We spent months working together to write the PC645 manuscript, and in the process I learned a tremendous amount about what makes a good

sentence, a good paragraph, a good paper, and a good scientist.

To conclude, I have to thank the most important people of all, my parents and my wife.

My dad passed away during my PhD, but I still feel his love and support with me every day. He was a role model of compassion and kindness, and he was always pushing me to follow my dreams. He seemed to become even more proud of me each day that went by. I miss him a lot.

My mother has been a driving force in my life, and a large part of every one of my successes is due to her. She has worked incredibly hard to pass her best attributes onto me, and has tirelessly advocated for me every step of the way. She has been my best teacher, my biggest fan, and my most reliable support system for the last 27 years, and I cannot possibly express how grateful and lucky I am to call her my mom.

Finally, there's my incredible life partner, Becca. Moving to Boston together and making a home here has been a dream come true, and knowing that I would come home to see my best friend every night made each day so much easier. I never thought I would get so lucky as to have such a fun, funny and supportive partner who simultaneously made me feel wonderful and brought out the best in me while also pushing me to be an even better person and friend to those around me. I definitely could not have completed this PhD without her and cannot wait to see what life has in store for us next.

Further Acknowledgements by Chapter

Chapter 1 contains content that has been previously published in the following article: Thomas Markovich, Samuel M. Blau, John Parkhill, Christoph Kreisbeck, Jacob N. Sanders, Xavier Andrade, Alán Aspuru-Guzik. "Accelerating the Computation of Bath Spectral Densities with Super-resolution." Theor. Chem. Acc. (2016) 135: 215

Chapter 2 contains content that has been previously published in the following article: Samuel M. Blau, Doran I. G. Bennett, Christoph Kreisbeck, Gregory D. Scholes, Alán Aspuru-Guzik. "Local protein solvation drives direct down-conversion in phycobiliprotein PC645 via incoherent vibronic transport." arXiv (2017).

Chapter 3 contains content that will be submitted separately for publication as "*Ab Initio* Simulations of a Synthetic Fluorescein Dimer Reveal Electronic Coherence" with the following author list: Samuel M. Blau, Christoph Kreisbeck, Doran I. G. Bennett, Alán Aspuru-Guzik.

Other publications completed during my PhD, but not included in the text of this dissertation, include:

- Thomas Markovich, Samuel M. Blau, Jacob N. Sanders, Alán Aspuru-Guzik. "Benchmarking Compressed Sensing, Super-Resolution, and Filter Diagonalization" Int. J. Quantum Chem. (2016) 116, 10971106.
- Doran I. G. Bennett, Pavel Malý, Samuel M. Blau, Christoph Kreisbeck, Alán Aspuru-Guzik. "Regimes of vibronic transport revealed by a model vibronic dimer." In preparation.

Introduction

Photosynthesis is one of the natural wonders of the world, and is arguably the most important chemical process on our planet. Photosynthetic light-harvesting provides the vast majority of the energy that drives life on earth, creates all of the necessary organic compounds for life, and maintains the oxygen content of the atmosphere on which most organisms depend. Furthermore, over the course of evolution, natural photosynthesis has adapted to incredibly different conditions, allowing photosynthetic organisms to thrive at very high and very low temperatures, vastly different altitudes, in fresh, salt, and brackish water, and both when there is far too much light and when there is almost no light at all. These organisms, in turn, provide the foundation for totally unique ecosystems that facilitate earth's wonderous biodiversity.

The immense importance of photosynthesis to humanity has made it a frequent area of research for biologists and chemists over the last century. Beyond merely satisfying intellectual curiousity, a thorough understanding of different types of photosynthesis could allow us to bioengineer crops with higher yield[1] and could lead to novel bioinspired technologies. More specifically, learning how nature efficiently captures and transports energy could allow us to improve our equivalent technologies, an essential step towards curbing the human-induced climate change that threatens the entire planet. However, if our goal is to determine the mechanisms that facilitate efficient light-harvesting, then the systems of particular interest are algae and bacteria that survive under very low-light conditions and have thus evolved particularly efficient photosynthetic machinery.

The process of photosynthetic light-harvesting in bacteria begins with the absorption of a photon in an antenna complex made from proteins containing optically-active pigments such as bacteriochlorophyll or phycobilins. This generates a bound electron-hole pair, known as a Frenkel exciton, which represents a pigment in its excited state. The exciton

then migrates through various pigment-containing biological complexes until it reaches the reaction center, where the excitation energy is used to drive the formation of a molecule containing a high-energy chemical bond which carries redox potential to down-stream metabolites.

The organism for which natural light-harvesting has been most rigorously studied is green sulfur bacteria, which can survive in very low light and exhibits photosynthetic machinery with high quantum efficiency.[2] Followig the absorption of a photon in the antenna complex, the resulting exciton migrates through the chlorosome to the base plate and through the Fenna-Matthews-Olsen (FMO) complex to the reaction center. Since FMO serves as the last link in the energy transfer cascade, it is assumed to be the most efficient energy transporter.[3] FMO is by far the most studied protein that performs excitation energy transfer (EET), in part because it was the first pigment-protein complex (PPC) to be structurally analyzed by x-ray spectroscopy.[4]

In 2007, Engel et al. probed the energy transfer dynamics of FMO using 2D echo spectroscopy and observed long-lived off-diagonal oscillations that they interpreted as evidence of wave-like excitation transport.[5] Their argument was twofold: they suggested that an excited state could remain a coherent quantum superposition delocalized over multiple chromophores fluctuating at physiological temperatures for up to a picosecond, and they proposed that such a long-lived coherence could functionally enhance excitation energy transport (EET) in photosynthesis. Engel precipitated a massive research effort to better understand quantum effects in biology, and the resulting field eventually became known as excitonics.

Engel's work was immediately controversial, in part due to his use of 2D echo spectroscopy. 2D echo spectra simultaneously probe all possible excitation pathways and all relevant coupled environmental vibrations, making them extremely information-rich while convoluting their analysis. The controversy thus prompted the use of theoretical methods that can disentagle the pathways present in experimental 2D spectra, allowing

for corroboration or contradiction of experimentally assigned mechanisms. Unfortunately, simulating the exciton dynamics of multiple pigments (eight, in the case of FMO) bound in a fluctuating protein scaffold at physiological temperature is incredibly computationally demanding and necessitates uncontrolled approximations that may yield unreliable results. Despite the limitations, theoreticians were eventually able to show that coherence between purely electronic excited states could not last a picosecond in biological systems.[6] It was instead proposed that long-lived 2D oscillations were due to the interplay between electronic excitations and environmental vibrations, which came to be known as vibronic coherence.[7,8] Soon afterwards, vibronic coherence was suggested to be functionally relevant for EET in both the photosynthetic reaction center[9,10] and in phycobiliprotein PC645.[11]

In this dissertation, I simulate and disentangle the excitation dynamics in the presence of complex vibrational environments for phycobiliprotein PC645. I also apply an equivalent procedure to examine three synthetic fluorescein dimers that were engineered to be a model system for investigating exciton coherence. I have gone beyond the standard approximations in the field by developing new techniques and leveraging substantial computational resources to employ reliable *ab initio* methods that were previously considered too costly.

In the first part of this dissertation, I demonstrate that a signal processing technique called super-resolution can reduce the computational effort required to extract accurate spectral densities by a factor of four. A spectral density definies the frequency-dependent coupling of an excited state to its thermal environment. Spectral densities and the system Hamiltonian, which defines the excited state energies and their electronic coupling, are the necessary ingredients for simulating excitation dynamics at finite temperature. Both components can be extracted by propagating an equilibrated nuclear dynamics trajectory and performing thousands of excited state and electronic coupling calculations on geometry snapshots at regular intervals. Averaging the excitation energy and coupling

trajectories yields the system Hamiltonian, while constructing and Fourier-transforming energy-gap correlation functions from the excited state trajectories yields the site spectral densities. Exciton dynamics can then be propagated with a range of different open quantum systems methods with accuracies proportional to their computational cost.

In the second part of this dissertation, I simulate the excitation dynamics of phycobiliprotein PC645, a light-harvesting complex found in cryptophyte algae that is one of the two systems for which vibronic coherence has been assigned functional relevance. I instead show that the protein's key action, directly down-converting excitations from the highest-energy pigments to the lowest-energy pigments, proceeds via an incoherent mechanism. For the first time in the field of excitonics, I extract spectral densities from *ab initio* molecular dynamics (AIMD) combined with QM/MM time-dependent density functional theory (TDDFT) excited state calculations, resolving the potential energy surface mismatch that has plagued all previous atomistic spectral densities. I then employ a high-performance implementation of the numerically-exact hierarchical equations of motion (HEOM) non-Markovian exciton dynamics method[12–14] to simulate spectra and dynamics. I obtain the first-ever quantitative *ab initio* reproduction of experimental linear spectra for a pigment-protein complex and also find that stronger than expected coupling to environmental vibrations critically controls the pathways of excitation transport. Finally, I generalize my findings using a model vibronic dimer, defining regimes of vibronic transport and demonstrating that vibronic coherence cannot be functionally relevant in biological systems.

In the third and fourth parts of this dissertation, I simulate the excitation dynamics of three controversial synthetic fluorescein heterodimers. The dimers were engineered with the goal of providing a model system for investigating coherent energy transfer in multichromophoric systems and were found to exhibit long-lived 2D off-diagonal oscillations.[15] I extract Hamiltonians and spectral densities at great computational cost, again using AIMD, and observe electronic couplings to be an order of magnitude larger

than previously thought. I find that large couplings critically modify the coherent frequencies and yield excellent agreement between simulated and experimental linear spectra. I then simulate coherence dynamics and a trajectory of 2D spectra and demonstrate that electronic coherence persists for just 100-150 femtoseconds, after which long-lived vibrationally driven coherences persist for hundreds of femtoseconds. Thus, I resolve the controversial nature of the coherence in these fluorescein dimers and confirm that while electronic coherence can be engineered in artifical molecular systems, even under ideal conditions it will not persist for a picosecond, as previously claimed.

I hope that the findings outlined in this dissertation will help shift the field of excitonics away from being focused entirely on the importance of coherence in photosynthetic light-harvesting. I instead propose that research should be focused on developing more reliable experimental techniques for probing energy transfer dynamics than 2D echo spectroscopy and more efficient computationial techniques for simulating excitation dynamics than those I employed, which required years of real and computational time to treat only two systems. In concert, these advances would allow us to finally understand larger and more important systems, such as the photosynthetic reaction center, and would also allow smaller systems to be treated en masse in screening applications. This, in turn, would accelerate the development of next-generation excitonic technologies that can help us to improve our energy efficiency and contribute to critical efforts to avoid catastrophic climate change.

1

Accelerating the Computation of Bath Spectral Densities with Super-resolution

Apart from minor modifications, this chapter originally appeared as:

"Accelerating the Computation of Bath Spectral Densities with Super-resolution." Thomas Markovich, Samuel M. Blau, John Parkhill, Christoph Kreisbeck, Jacob N. Sanders, Xavier Andrade, Alán Aspuru-Guzik. Theor. Chem. Acc. (2016) 135: 215

1.1 Abstract

Quantum transport and other phenomena are typically modeled by coupling the system of interest to an environment, or bath, held at thermal equilibrium. Realistic bath models are at least as challenging to construct as models for the quantum systems themselves, since they must incorporate many degrees of freedom that interact with the system on a wide range of timescales. Owing to computational limitations, the environment is often modeled with simple functional forms, with a few parameters fit to experiment to yield semi-quantitative results. Growing computational resources have enabled the construction of more realistic bath models from molecular dynamics (MD) simulations. In this paper, we develop a numerical technique to construct these atomistic bath models with better accuracy and decreased cost. We apply a novel signal processing technique, known as super-resolution, combined with a dictionary of physically-motivated bath modes to derive spectral densities from MD simulations. Our approach reduces the required simulation

time and provides a more accurate spectral density than can be obtained via standard Fourier transform methods. Moreover, the spectral density is provided as a convenient closed-form expression which yields an analytic time-dependent bath kernel. Exciton dynamics of the Fenna-Matthews-Olsen light-harvesting complex are simulated with a second order time-convolutionless master equation, and spectral densities constructed via super-resolution are shown to reproduce the dynamics using only a quarter of the amount of MD data.

1.2 Introduction

Irreversible processes such as solvation, energy transfer, and chemical binding have received renewed interest in recent years. Because these processes involve large systems with many degrees of freedom, the typical approach to studying these processes is the open quantum systems formalism, in which the degrees of freedom are partitioned into a system of interest and a bath held at thermal equilibrium.[16,17] It is commonly assumed that the system only couples weakly to the bath, making the precise nature of the bath a secondary concern in the physical theory. For example, in studying the energy transfer dynamics in a system of chromophores embedded in a protein framework, each chromophore is individually coupled to many thousands of atoms in the protein, but the system-bath formalism dramatically simplifies all of these couplings in order to make the dynamics tractable.[18–20] Renewed interest in the strong and intermediate coupling region, relevant for energy transfer in the exciton dynamics of light-harvesting complexes, has lead to various studies[20–43] on the precise influence of the bath on the higher systems. Higher order phonon processes, non-Markovian effects and structures in the exciton-phonon coupling change the energy transfer.[44–46] Thus, details in the bath are relevant and need to be taken into account in realistic simulations. Accordingly, our goal in this paper is to apply a recent signal-processing technique known as super-resolution to obtain realistic atomistic models of environments containing thousands of atoms at

feasible computational expense. With these atomistic bath models in hand, one can begin to evaluate the importance of a realistic bath model in a physical theory.

In the approach to open quantum systems employed in this work, we model the bath by an ensemble of noninteracting harmonic oscillators. The central mathematical object of such a model is the *spectral density*, $J(\omega)$, which gives the frequency-dependent strength of system-bath coupling. The spectral density can be understood as the density of bath oscillator states at each frequency. Owing to computational limitations, most studies of open quantum systems assume an extremely simple functional form for the spectral density, such as a single broad peak covering all relevant excitonic transitions of the system. With the goal of providing more physically accurate bath models and dynamics, Valleau *et al.* has previously obtained atomistic spectral densities for the Fenna-Matthews-Olson (FMO) complex from combined Molecular Dynamics (MD)[47,48] and time-dependent density functional theory (TDDFT)[49] simulations. However, the difficulty of this more realistic approach is the high computational cost of running expensive TDDFT calculations at every step in an MD simulation. In order to obtain a spectral density of sufficient resolution, the MD-TDDFT simulation must be run for over 40 picoseconds (ps),[50] which may become computationally intractable for larger systems.

To make progress, we first observe that a typical vibrational bath is not an arbitrary function but rather a relatively sparse collection of damped harmonic oscillators. Sparsity enables us to apply a novel numerical technique known as super-resolution in order to reconstruct the spectral density from much shorter MD-TDDFT simulations. Super-resolution has been applied to a broad range of scientific problems, including image[51] and video compression,[52] image denoising,[53] astronomy,[54] microscopy,[55] and medical imaging.[56] To our knowledge, this paper is the first application of super-resolution to quantum dynamics. Super-resolution provides a provably convergent algorithm for the reconstruction of signals from limited time-domain measurements using a total variation minimization procedure. Super-resolution is related to compressed

sensing.[57–68] Compressed sensing is a technique designed to recover sparse signals from randomly-sampled data by minimizing the $\mathcal{L}_1$ norm of an underdetermined system of linear equations. Compressed sensing works by finding the sparsest signals consistent with the underdetermined system of equations. This usually involves an optimization problem. Despite its success in many applications, the $\mathcal{L}_1$-norm minimization of compressed sensing can result in spurious signals as it emphasizes the sparsity of the solution only.
Super-resolution is a numerical method that shares the spirit of compressed sensing. The difference between superresolution and compressed sensing stems from both the choice of objective function and sampling technique. It was developed to recover sparse signals from nonrandomly undersampled data. By minimizing the $\mathcal{L}_1$-norm of the gradient of the function in addition to the $\mathcal{L}_1$ norm of the function itself, super-resolution allows for smoother solutions to the sampling problem.[69–71]

Because of the ample experimental and theoretical data to compare against,[6,20,23–26,28,31–34,36,37,39,42,46,47,72–79] we apply super-resolution to the FMO light-harvesting complex of *C. tepidium* but emphasize that this technique is broadly applicable. While this paper focuses on a vibrational bath which perturbs the energies of molecular electronic states, the techniques we introduce are generic for any model of a bath which is based on time-correlation functions.

1.3 Super-resolution of Spectral Densities

In this section, we briefly review the procedure for simulating the dynamics of open quantum systems and computing spectral densities from combined MD-TDDFT simulations. We then apply the theory of super-resolution to accelerate and improve the accuracy of these computations. Computing spectral densities from atomistic calculations, rather than from semi-empirical functional forms, enables the inclusion of molecular vibrations and other physical effects (such as solvation effects) to produce a more realistic bath model.[47] Super-resolution, in turn, brings the construction of these atomistic bath

models into the realm of computational feasibility.

Armed with our more realistic bath model, we will employ a second-order time-convolutionless master equation (TCL-2) to simulate the dynamics of FMO monomer, allowing us to evaluate the physical impact of different approximations to the spectral density. TCL-2 includes non-Markovian effects up to second order in the system-bath coupling. By comparing TCL-2 with exact methods like the hierarchical equations of motion (HEOM)[80] we show that most of the relevant effects of the structured spectral density of the FMO complex are captured by TCL-2. Here we use TCL-2, since it is numerically more treatable than HEOM, in particular for structured spectral densities where HEOM becomes cumbersome and requires a high performance GPU implementation.[32,46,81] We employ the equation of motion:[16,22,24,39,77,82–88]

$$\frac{d\rho_I(t)}{dt} = -\frac{i}{\hbar}[H_I, \rho_I] - \frac{1}{\hbar^2}\sum_n \int_0^t \mathrm{d}\tau\, D_n(t-\tau)[H_{In}(t), [H_{In}(\tau), \rho_I(t)]] \tag{1.1}$$

$$D_n(t) = \int_0^\infty \mathrm{d}\omega\; J_n(\omega)\left[\coth\left(\frac{\hbar\,\omega\beta}{2}\right)\cos(\omega\,t) - i\sin(\omega\,t)\right] \tag{1.2}$$

where H is the system Hamiltonian, ρ is the system density matrix, D is our bath kernel, the subscript I indicates that we are in the interaction picture, the summation runs over all sites, and $J(\omega)$ is the spectral density computed via super-resolution.[32,78,79,89,90] The bath kernel is heavily dependent on our spectral density, causing it to play a central role in our dynamics. Therefore, a more physical bath picture should provide more physically intuitive dynamics.

In our atomistic bath model, molecular vibrations in the environment (e.g. a protein framework or solvation effects) create fluctuations in the energy gaps between the ground and excited states of the system (e.g. a set of chromophores). These time-dependent energy gaps are computed from TDDFT calculations run on each of the chromophores at

each step of the MD simulation. The key object in the computation of spectral densities is the correlation function of the energy gap time series,

$$C(t) = Tr_b[\hat{\Delta}(t)\hat{\Delta}(0)\hat{\rho}_b], \tag{1.3}$$

where $\hat{\Delta}(t)$ is the time-dependent energy gap between the ground and the first excited state of the system (as calculated with TDDFT), $\hat{\rho}_b$ is the density matrix of the bath at thermal equilibrium, and $C(t)$ is the correlation function obtained after tracing over all the modes of the bath. We discretize this equation by using an unbiased autocorrelation function,

$$C_k = \frac{1}{N-k}\sum_{i=1}^{N-k}(\Delta_i - \bar{\Delta})(\Delta_{i+k} - \bar{\Delta}), \tag{1.4}$$

where $\bar{\Delta}$ is the mean energy gap and i and k denote discrete time indices. Note that C_k involves comparing energy gaps that are k time steps apart (Δ_i and Δ_{i+k}), and $N-k$ is the total number of included comparisons.

The frequency-dependent spectral density, $J(\omega)$, is typically obtained by computing the Fourier transform of the correlation function.[47] From the definition of C_k above, it is easy to check that the correlation function is real and symmetric ($C_k = C_{N-k}$), which implies that the Fourier transform should be real and symmetric as well. Because quantum mechanical spectral densities must instead be antisymmetric and obey detailed balance, it is necessary to introduce a prefactor that enforces these two properties. Many choices are possible,[91] but Valleau *et al.* have previously shown that a harmonic prefactor, $\beta\hbar\omega/2$, produces the most physical temperature dependence.[47] With this choice, the spectral density becomes the cosine transform

$$J(\omega) = \frac{\beta\hbar\omega}{2}\int_{-\infty}^{\infty}\cos(\omega t)C(t)\mathrm{dt}, \tag{1.5}$$

which characterizes the frequency-dependent coupling strength of the system to all of the

nuclear vibrational modes.

The standard approach to performing this integral is the fast Fourier transform. Unfortunately, the fast Fourier transform requires sampling on a uniform grid at the Shannon sampling rate. This means that a relatively long time series, $C(t)$, must be computed in order to obtain good resolution of the spectral density in the frequency domain.[50,92] Given the computational cost of MD simulations, and the even greater expense of running TDDFT calculations on top of these simulations, any method which can reduce the required length of the time series $C(t)$ unplugs the computational bottleneck in deriving physically-accurate atomistic spectral densities. That is our main goal in this paper.

While reducing the amount of time required to reproduce $J(\omega)$ we also choose a basis of functions which has a convenient physical form. When decomposed into a basis of damped cosines,

$$g_{ij}(t) = e^{-\gamma_i t} \cos(\Omega_j t), \tag{1.6}$$

the function $C(t)$ is smooth and sparse. This allows for the use of the machinery of super-resolution.

To apply the super-resolution method, we discretize in time and cast our task as an inversion problem

$$C_k = \lambda_{ij} e^{-\gamma_i t} \cos(\Omega_j t_k), \tag{1.7}$$

where we seek the basis expansion coefficients λ_{ij} and have assumed Einstein summation convention over repeated indices. This can be rewritten as

$$C_k = A_{ijk} \lambda_{ij}, \tag{1.8}$$

where

$$A_{ijk} = e^{-\gamma_i t} cos(\Omega_j t_k) \tag{1.9}$$

is a matrix of damped cosines, and λ_{ij} is the set of basis coefficients we seek to recover.

The central idea of super-resolution is that the sparsity of λ_{ij} enables its full recovery even when the system $C_k = A_{ijk}\lambda_{ij}$ is underdetermined, which is to say the number of time samples C_k is significantly smaller than the number of total expansion coefficients λ_{ij} we seek to recover. Hence, we can recover the expansion coefficients on a dense grid of frequencies Ω_j and damping coefficients γ_i from fewer time samples C_k. Of the many possible solutions to our underdetermined system, super-resolution simply selects a balance between the smoothest and sparsest (with an emphasis on smoothness) set of basis expansion coefficients. Formally, this is done by finding the vector λ_{ij} that minimizes

$$\begin{aligned} &\underset{\lambda_{ij}}{\operatorname{argmin}} \left\{ ||\nabla \lambda_{ij}||_1 + \mu ||\lambda_{ij}||_1 \right\} \\ &\text{subject to } \; ||A_{ijk}\lambda_{ij} - C_k||_2 < \eta, \end{aligned} \tag{1.10}$$

where the subscript 1 represents the $\mathcal{L}_1$ norm (sum of absolute values), μ represents a sparsity penalty, $\nabla\lambda_{ij}$ represents the total variation norm, and η represents the solution tolerance. By minimizing $||\nabla\lambda_{ij}||_1$, or total variation term, we are enforcing smoothness in the time domain on the reconstructed signal. This throws out the "peaky" solutions that can appear with compressed sensing.[93,94] The total variation norm also provides us with a provably exact technique for recovering peak position at the expense of peak amplitude,[69] which solves one of the issues seen previously with compressed sensing.[93]

Recovering the expansion coefficients λ_{ij} in this manner by solving an underdetermined matrix inversion problem takes advantage of the natural sparsity of the problem and, as we will see in the next section, enables the construction of a well-resolved spectral density with far less time-domain data. Even more attractive, with the λ_{ij} coefficients in hand, it is possible to construct an analytical representation of the spectral density by taking the cosine transform of the basis functions $g_{ij}(t)$ and applying the appropriate prefactors:

$$J(\omega) = \frac{\lambda_{ij}}{\sqrt{\pi}} \left(\frac{\beta\hbar\omega\gamma_i}{\gamma_i^2 + (\omega - \Omega_j)^2} + \frac{\beta\hbar\omega\gamma_i}{\gamma_i^2 + (\omega + \Omega_j)^2} \right), \tag{1.11}$$

where the Einstein summation convention has again been assumed. This is an analytical representation of the spectral density in Drude-Lorentz form, and it explicitly provides the oscillation frequencies which characterize the system-bath coupling. We note that the Drude-Lorentz basis naturally provides us with a width parameter, γ, that can be understood as the lifetime of oscillations in the bath. This is seen by examining the time dependent formula, Eq. (1.7), where this γ parameter determines the strength of damping. It is important to note that in the limit as $\gamma \to 0$, we recover the cosine basis in the time domain and a Dirac delta distribution in the frequency domain. By using this super-resolution technique in concert with the Drude-Lorentz basis, we see that we can recover a small set of peaks with physically-relevant information. Additionally, the parameters that characterize the Drude-Lorentz spectral densities can be input directly into both TCL-2 and HEOM without any additional parameter fitting or numerical integration.

1.4 Numerical Methods

We employ the proposed Drude-Lorentz super-resolution method described above and apply it to a monomer of the Fenna-Matthews-Olsen (FMO) photosynthetic energy transfer complex of the green-sulfur bacterium *C. tepidium*. The FMO monomer is a system of seven chlorophyll molecules which are excitonically coupled to each other, as well as to the vibrations of the atoms in the protein framework. It functions as a molecular excitonic wire, passing excitons from the light harvesting antenna complex to the reaction center, where a biochemical cascade is initiated.

To create spectral densities for the FMO complex, we use the MD-TDDFT results of Shim *et al.*[77] The calculations were done in an isothermal-isobaric ensemble at 77 K using the AMBER force field.[95,96] These calculations began with a 2 ns equilibration before performing the production computations. The production steps ran for a total of 40 picoseconds with a 2 femtosecond timestep, and the optical gap was calculated for each

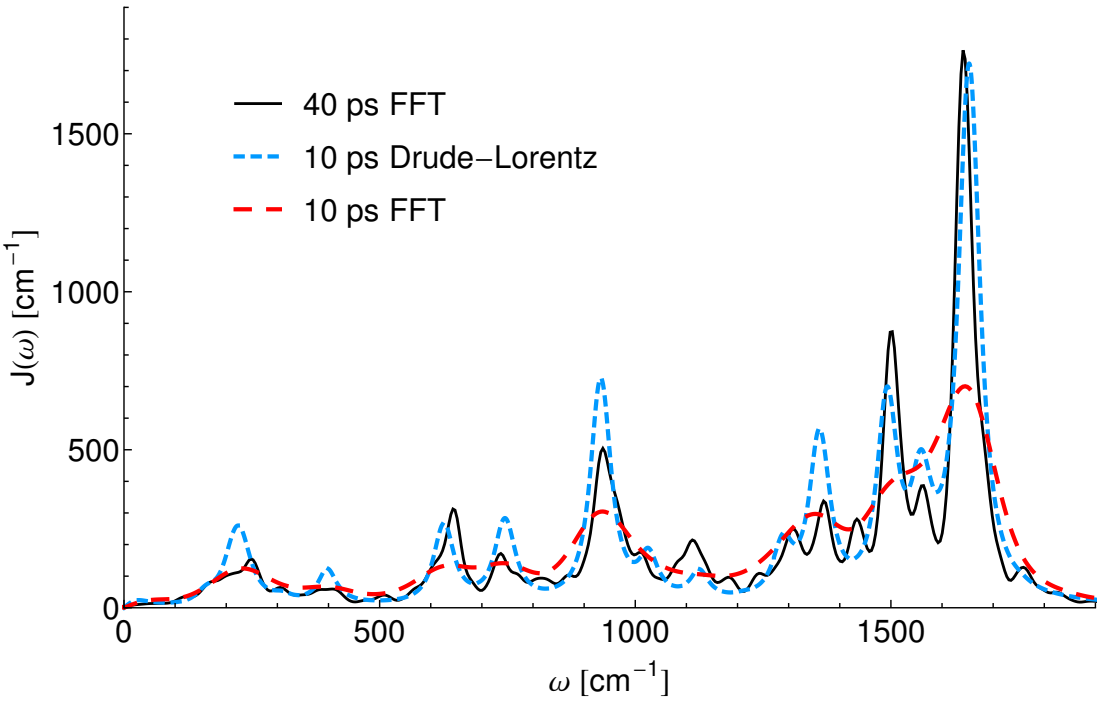

Figure 1.1: Comparison of the spectral density for site 1 of the FMO complex as a function of time and technique for spectral density recovery. Compared to the fast Fourier transform at 40 ps, much of the fine structure is easily recovered by super-resolution in the Drude-Lorentz basis, even with significant undersampling by a factor of four.

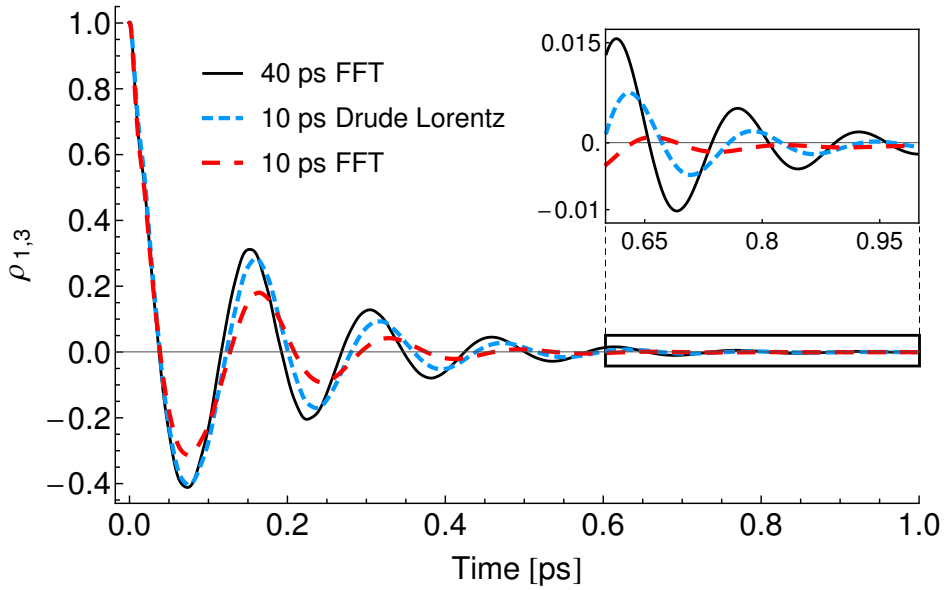

Figure 1.2: Comparison of the coherences between excitonic eigenstates 1 and 3 as a function of time and technique for spectral density recovery. Compared to the fast Fourier transform at 40 ps, the 10 ps Drude-Lorentz decomposition introduces a slight shift in oscillation frequency, but nevertheless yields more accurate dynamics than the equivalently-sampled fast Fourier transform at 10 ps.

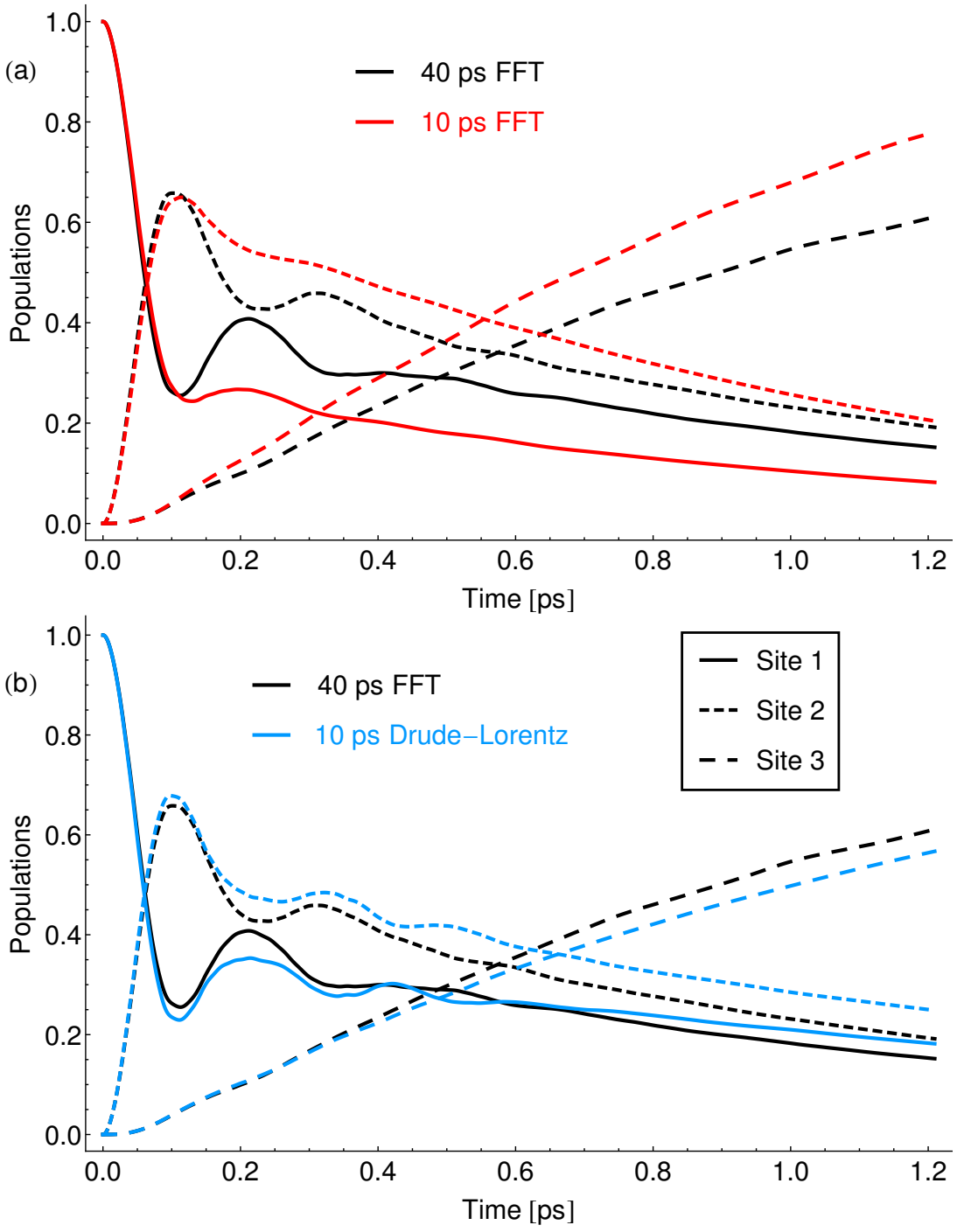

Figure 1.3: Comparison of the populations for sites 1-3 as a function of time and technique for spectral density recovery. Compared to the fast Fourier transform at 40 ps, the 10 ps Drude-Lorentz decomposition recovers the overall shape and provides much more faithful dynamics than the equivalently-sampled fast Fourier transform at 10 ps.

fragment every 4 femtoseconds using TDDFT with the BLYP[97–99] functional in the 3-21G basis set in Q-Chem.[100]

To perform super-resolution numerically, we require an algorithm which minimizes the total variation norm to solve the minimization problem described by eq. (1.10). In our implementation, we use the two step iterative shrinkage thresholding (TwIST) algorithm,[70,71] which combines computational efficiency with strong convergence. To construct the measurement matrix A described in eq. (1.9), we must select a grid of possible frequencies ($\{\Omega_j\}$) and linewidths ($\{\gamma_i\}$). In our implementation, we use a grid of frequencies ranging from 0 to 2000 cm^{-1} in 2 cm^{-1} intervals, and a grid of linewidths ranging from 0 to 160 cm^{-1} in 6 cm^{-1} intervals. We assume that our calculations are converged when $\eta < 10^{-7}$ (in eq. (1.10)), or the solution vector remains constant for 100 iterations. Finally, we perform an $\mathcal{L}_2$ minimization of $A_{ijk}\lambda_{ij} - C_k$ while freezing the recovered nonzero basis functions, allowing us to further minimize the error. We refer to this procedure as debiasing because it partly removes the bias towards sparsity and smoothness introduced by the $\mathcal{L}_1$ minimization. This debiasing procedure reduces our solution tolerance to $\eta < 10^{-9}$, allowing convergence to a better solution. It is important to note that, in general, the super-resolution technique is robust to an over-complete basis.

1.5 Results

Figure 1.1 shows the results of employing the Drude-Lorentz super-resolution method to recover the spectral density for site 1 of FMO. The figure compares Drude-Lorentz super-resolution with 10 ps of MD to a standard fast Fourier transform approach with both 10 and 40 ps of MD. We take the fast Fourier transform with 40 ps of MD as our standard for comparison. By comparing the two methods with 10 ps of MD, it is clear that super-resolution resolves more features of the spectral density than the standard fast Fourier transform from the same amount of time-domain data. Moreover, super-resolution captures most of the features of the fast Fourier transform with the full 40 ps of MD: we

see the expected CO stretch at 1600 cm^{-1}, which we attribute to the amides in the protein scaffold, as well as all of the other major peaks in the spectral density. We attribute a significant amount of the error in our spectral density reconstruction to the fact that the truncated MD series does not explore the phase space as thoroughly in only 10 ps.

The Drude-Lorentz basis also provides significant sparsity gains in comparison to the cosine basis: we require only 56 Drude-Lorentz peaks to create the spectral density given in Figure 1.1. This sparsity provides a significant computational advantage for excitonic propagation in both hierarchical equations of motion (HEOM)[80] and second order time-convolutionless master equation[16](TCL-2) approaches because the propagations scale factorially and linearly, respectively, as a function of the number of peaks included. In the excitonically accessible regime of 0-540cm^{-1}, we recover only 20 Drude-Lorentz peaks, and six of them have amplitudes that are two orders of magnitude smaller than the rest. These Drude-Lorentz peaks can be entered directly into master equation simulations, including HEOM codes, without the need to perform any intermediate fitting.[81] In summary, super-resolution yields a well-resolved spectral density using less time-domain data than is required by the standard fast Fourier transform approach and precludes the need for additional fitting.

As mentioned above, the TCL-2 propagation of the exciton dynamics of the FMO complex, with the Hamiltonian coming from,[73] was carried out using the Drude-Lorenz spectral densities obtained from super-resolution. We propagated 1 ps of dynamics and obtained the populations of sites 1-3, as well as the coherence between sites 1 and 3.

Figure 1.2 shows the coherence between excitonic eigenstates 1 and 3 as a function of time. Compared to the 40 ps fast Fourier transform, we see that the 10 ps Drude-Lorentz super-resolution more faithfully reproduces the coherence dynamics, both in terms of the oscillation frequency and the overall damping. The fast Fourier transform with 10 ps of MD data introduces serious overdamping as well as a significant shift in oscillation frequency. In contrast, the Drude-Lorentz expansion with 10 ps of MD data introduces

only a small shift in oscillation frequency, resulting in more accurate coherence dynamics overall. We attribute most of the discrepancies to slight relative differences in the reorganization of each site between spectral densities constructed with 10 and 40 ps of MD data. It appears that while the oscillations are extremely sensitive to the relative reorganization energies between the sites, the damping is more dependent on the fine structure of the spectral densities. The Drude-Lorentz super-resolution (10 ps MD-TDDFT data) reproduces the coherence life-times obtained by fast Fourier transform recovered using all 40 ps of MD-TDDFT data – representing a factor of four improvement.

The contrast between the two approximation techniques becomes even more significant when we simulate dynamics beginning with an exciton fully localized on site 1. In Figure 1.3, we have plotted the populations of the first three sites as a function of time. The Drude-Lorentz expansion with 10 ps of MD yields good qualitative agreement with our standard of comparison. The fast Fourier transform on 10 ps overestimates population transfer to site 3 at short times and grows much more quickly from there, whereas the Drude-Lorentz expansion slightly under predicts the population transfer at long times. We attribute these errors in the asymptotic behavior to slight differences in the reorganization energies for the spectral densities of each of the sites: Since each site is embedded in a different enviornment, the reorganization process of the individual pigments is different. This sensitivity affects overall dissipation, and even small changes in the spectral density of the Drude-Lorentz expansion (10 ps) when compared to the standard of comparison affects energy relaxation. Beyond that, the Drude-Lorentz expansion is capable of reproducing the oscillations at 0.2 and 0.4 ps in the data for sites 1 and 2, whereas the fast Fourier transform reproduces them less faithfully. In summary, the Drude-Lorentz super-resolution technique provides us with much more physical behavior.

1.6 Conclusions

We have shown that the Drude-Lorentz super-resolution method provides significant computational advantages for the construction of atomistic bath models. In particular, the super-resolution calculations require only 10 ps of MD-TDDFT simulations to obtain reasonable atomistic spectral densities and system dynamics; this is one quarter the amount of data needed in standard fast Fourier transform-based calculations. Ultimately, this will permit the use of more physically accurate calculations or larger systems. Given the computational expense of running TDDFT calculations at every MD simulation step, we believe that the super-resolution method will enable the treatment of larger systems than previously possible.

One of the most significant advantages of our super-resolution method is the decomposition of these atomistic spectral densities into a naturally-sparse basis of Drude-Lorentz oscillators. This makes it easy to perform fast master equation simulations within either the TCL-2 or HEOM formalisms by exploiting analytic integrals of the spectral density. Beyond this, we also directly extract physically-important parameters such as the coherence lifetimes of all the oscillators in the bath. In the future, it is easy to imagine turning this technique on its head to create new spectral densities in a constructive fashion from a set of Drude-Lorentz oscillators.

1.7 Acknowledgements

We acknowledge S. Valleau for useful discussions and computer code. We acknowledge the financial support of Defense Advanced Research Projects Agency grant N66001-10-1-4063 and the Defense Threat Reduction Agency under contract no. HDTRA1-10-1-0046. T.M. acknowledges support from the National Science Foundation (NSF) through the Graduate Research Fellowship Program (GRFP). S.B. acknowledges support from the Department of Energy (DoE) through the Computational Sciences Graduate Fellowship (CSGF).

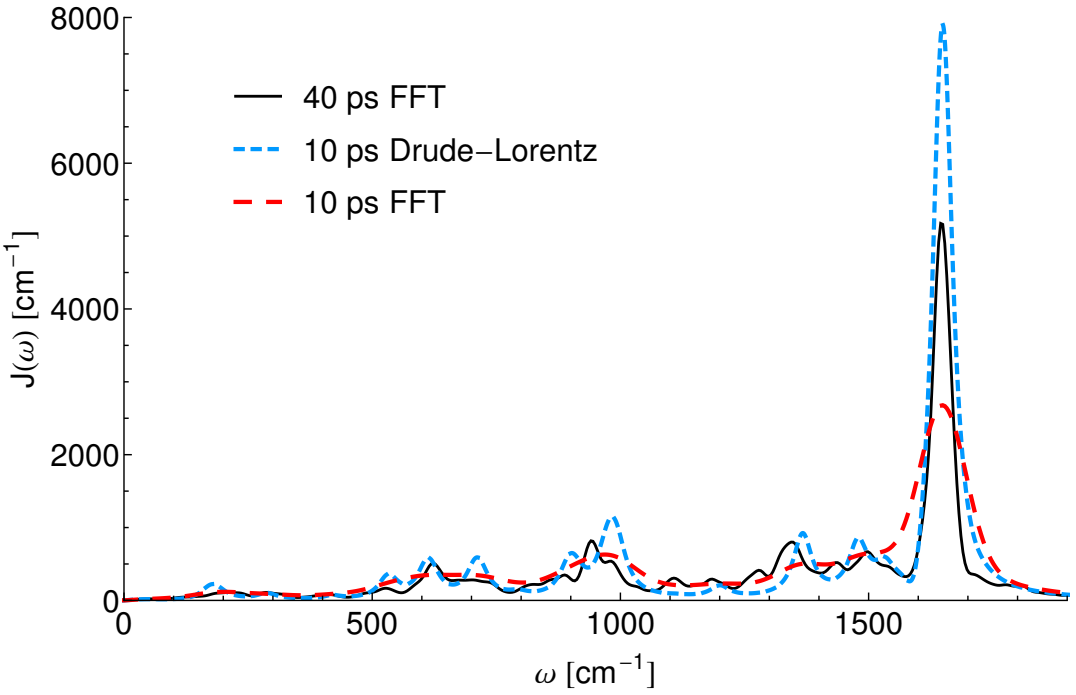

Figure 1.4: Comparison of the spectral density for site 2. We assume our basis to compare against is the fast Fourier transform at 40 ps and can see that much of the fine structure is easily recovered by super-resolution in the Drude-Lorentz basis, even with significant undersampling.

J.N.S. acknowledges support from the Department of Defense (DoD) through the National Defense Science & Engineering Graduate Fellowship (NDSEG) Program. A.A.G. thanks the Corning Foundation.

1.8 Supplementary Information

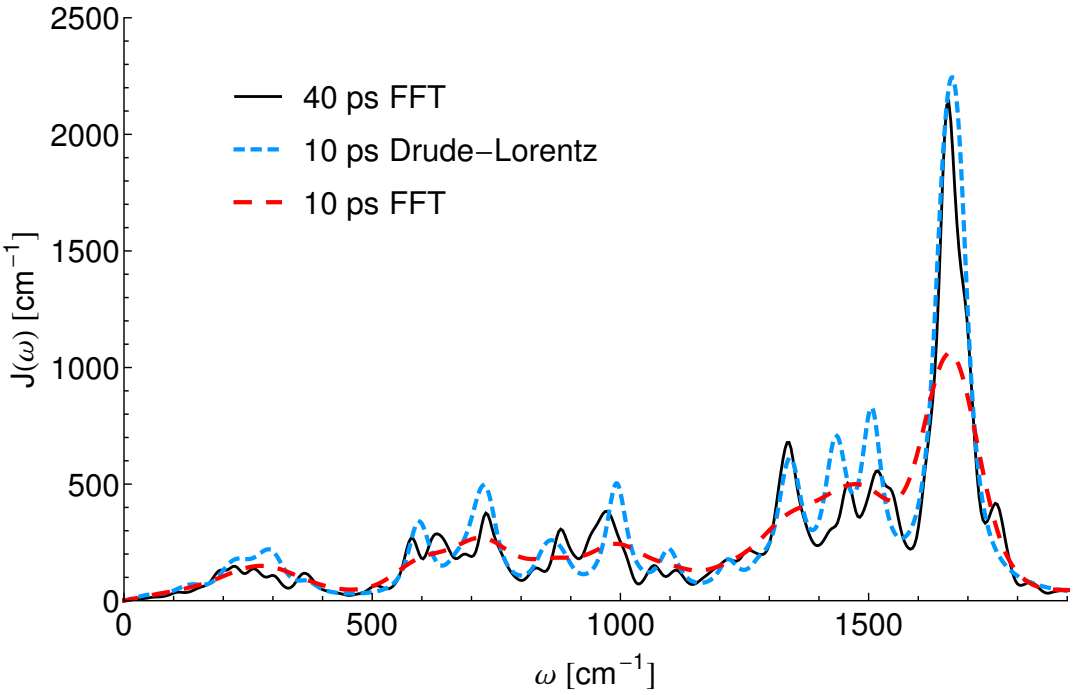

Figure 1.5: Comparison of the spectral density for site 3. We assume our basis to compare against is the fast Fourier transform at 40 ps and can see that much of the fine structure is easily recovered by super-resolution in the Drude-Lorentz basis, even with significant undersampling.

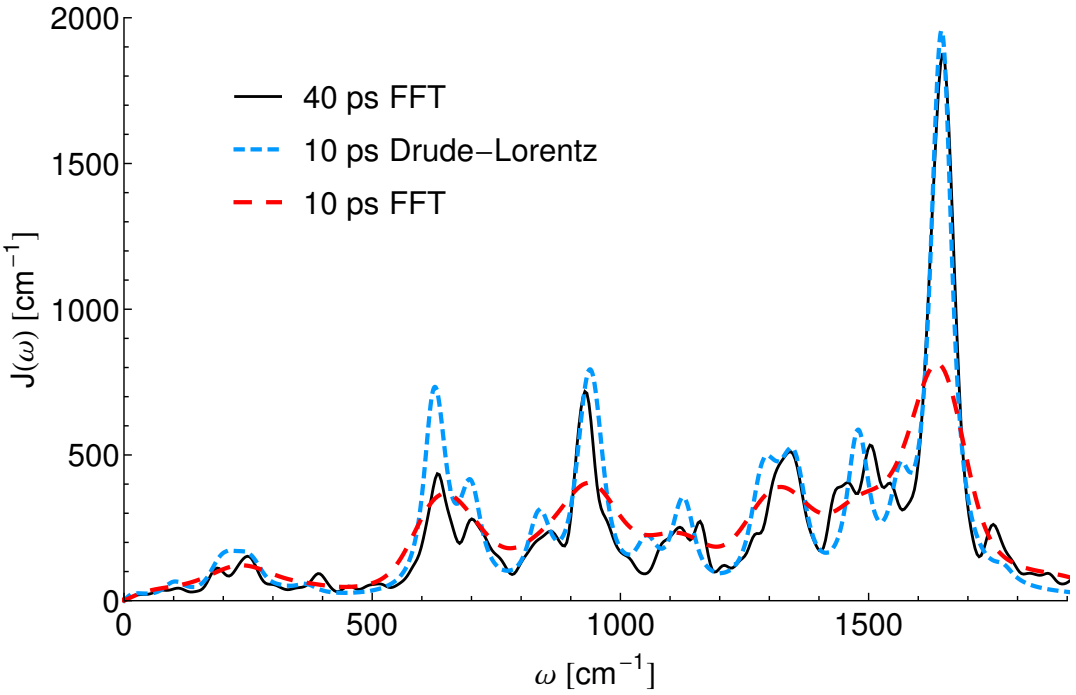

Figure 1.6: Comparison of the spectral density for site 4. We assume our basis to compare against is the fast Fourier transform at 40 ps and can see that much of the fine structure is easily recovered by super-resolution in the Drude-Lorentz basis, even with significant undersampling.

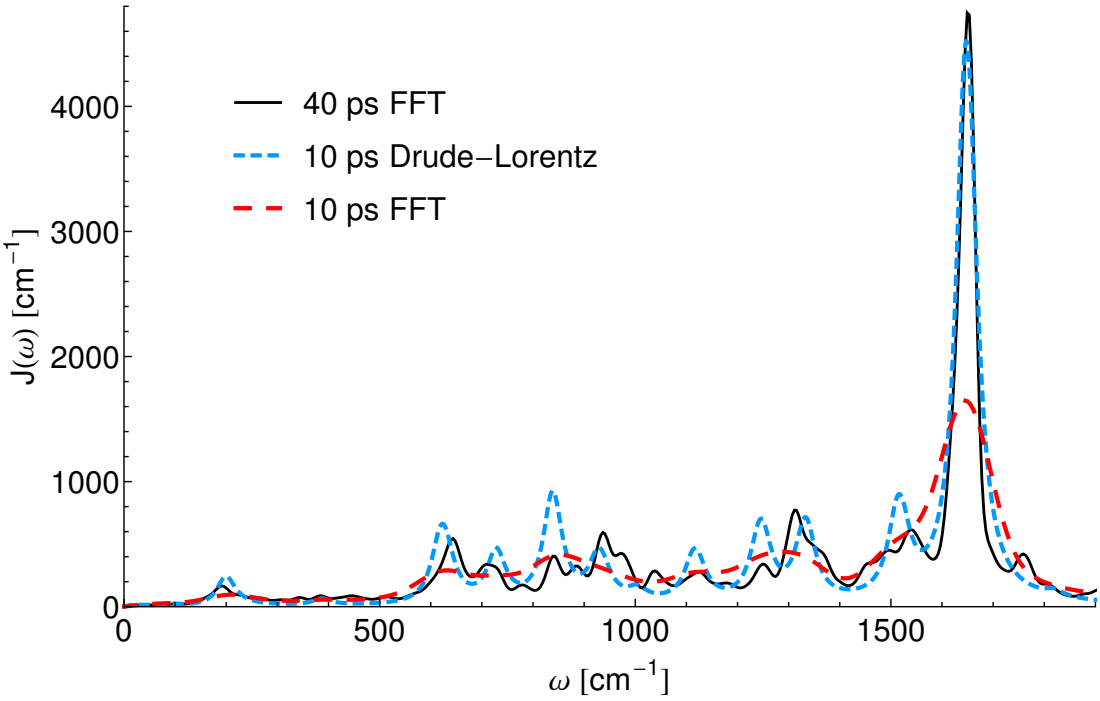

Figure 1.7: Comparison of the spectral density for site 5. We assume our basis to compare against is the fast Fourier transform at 40 ps and can see that much of the fine structure is easily recovered by super-resolution in the Drude-Lorentz basis, even with significant undersampling.

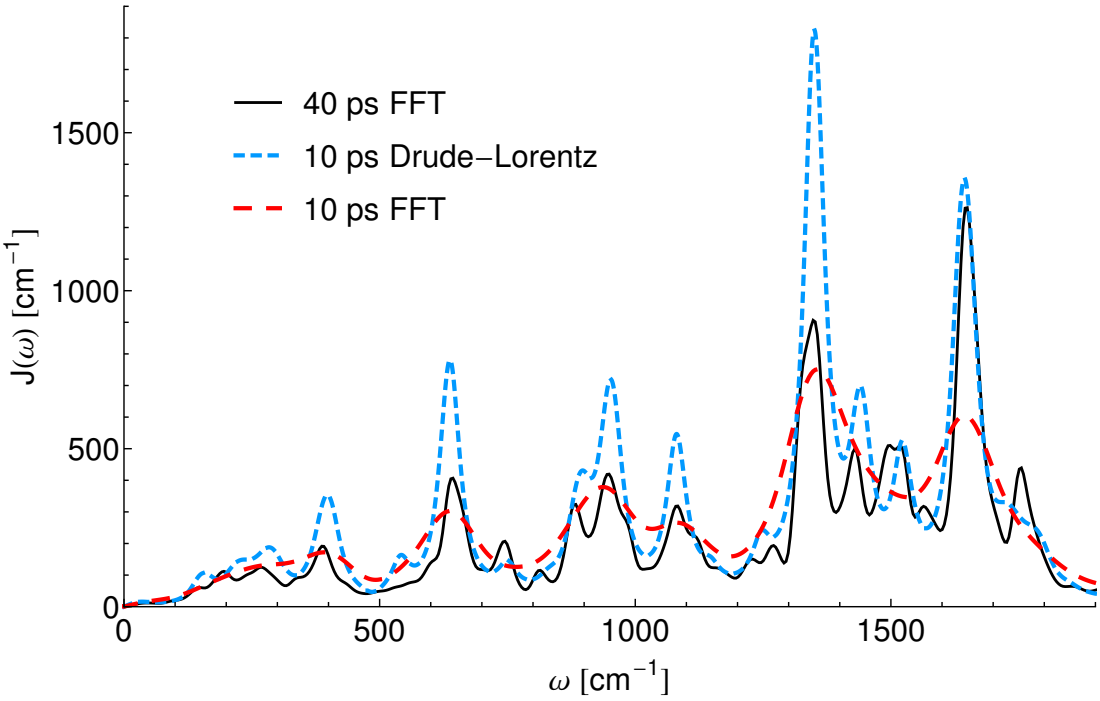

Figure 1.8: Comparison of the spectral density for site 6. We assume our basis to compare against is the fast Fourier transform at 40 ps and can see that much of the fine structure is easily recovered by super-resolution in the Drude-Lorentz basis, even with significant undersampling.

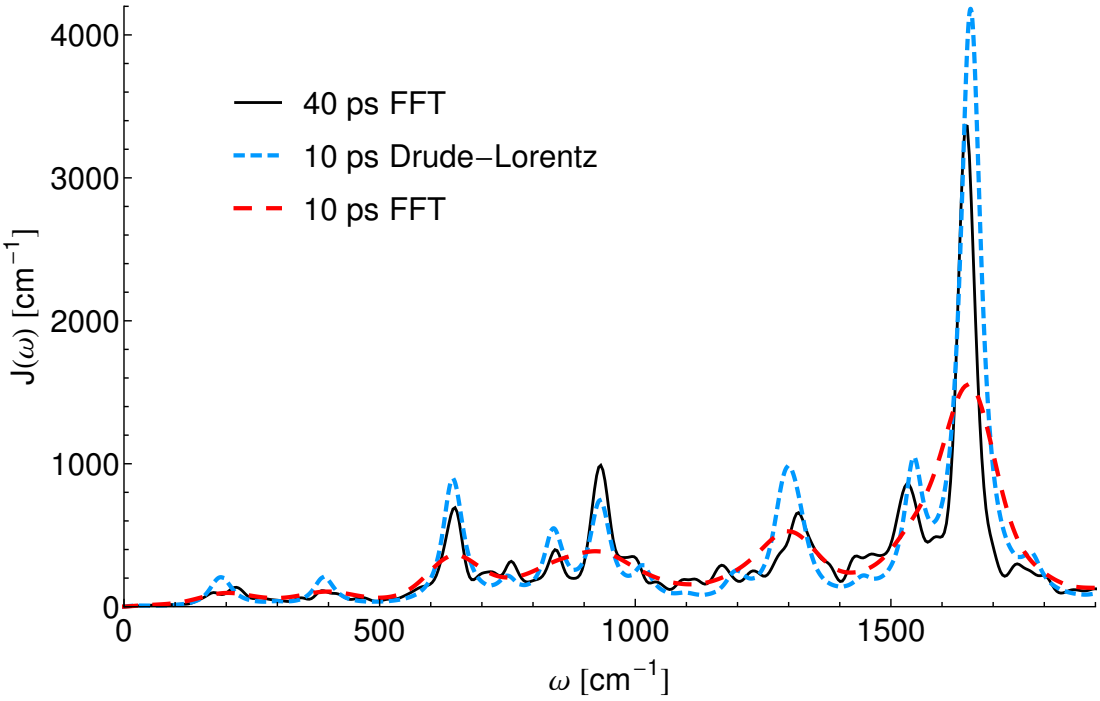

Figure 1.9: Comparison of the spectral density for site 7. We assume our basis to compare against is the fast Fourier transform at 40 ps and can see that much of the fine structure is easily recovered by super-resolution in the Drude-Lorentz basis, even with significant undersampling.

fast Fourier transform		Drude-Lorentz	
γ	Ω	γ	Ω
12.9325	149.473	21.94763	0.0219476
23.3477	379.902	21.94763	9.9230254
12.9826	246.711	21.94763	14.873564
13.1985	192.881	21.94763	19.824103
19.5356	307.654	21.94763	24.774642
11.2336	11.6004	21.94763	153.48865
11.2924	402.653	21.94763	158.43919
11.5613	417.323	21.94763	163.38973
12.9243	507.176	21.94763	168.34026
16.2019	224.982	21.94763	173.29080
23.4460	45.761	21.94763	202.99404
13.8991	208.986	21.94763	207.94458
-	-	21.94763	212.89511
-	-	21.94763	217.84565
-	-	21.94763	222.79619
-	-	21.94763	227.74673
-	-	21.94763	232.69727
-	-	21.94763	237.64781
-	-	21.94763	391.11452
-	-	21.94763	396.06505
-	-	21.94763	401.01559

Table 1.1: Comparison of $\mathcal{L}_2$ fits done by Kreisbeck *et al.* against ours in the excitonically accessible region

2

Local protein solvation drives direct down-conversion in phycobiliprotein PC645 via incoherent vibronic transport

Apart from minor modifications, this chapter originally appeared as:

"Local protein solvation drives direct down-conversion in phycobiliprotein PC645 via incoherent vibronic transport." Samuel M. Blau, Doran I. G. Bennett, Christoph Kreisbeck, Alán Aspuru-Guzik. arXiv (2017)

2.1 Abstract

Mechanisms controlling excitation energy transport (EET) in light-harvesting complexes remain controversial. Following the observation of long-lived beats in two-dimensional electronic spectroscopy of PC645, vibronic coherence, the delocalization of excited states between pigments supported by a resonant vibration, has been proposed to enable direct down-conversion from the highest-energy states to the lowest-energy pigments. Here, we instead show that for phycobiliprotein PC645 an incoherent vibronic transport mechanism is at play. We quantify the solvation dynamics of individual pigments using *ab initio* QM/MM nuclear dynamics. Our atomistic spectral densities reproduce experimental observations ranging from absorption and fluorescence spectra to the timescales and

selectivity of down-conversion observed in transient absorption measurements. We demonstrate that bilin solvation controls EET pathways and that direct down-conversion proceeds incoherently, enhanced by large reorganization energies and a broad collection of high-frequency vibrations. We thus suggest that engineering local solvation dynamics represents a potential design principle for nanoscale control of EET.

2.2 Introduction

Understanding the solvation dynamics of multiple pigments in a heterogeneous medium is essential for being able to control excited state dynamics in artificial materials. Natural photosynthesis demonstrates this capability in light-harvesting complexes, which exert nanoscale control over excitation transport between pigments via the protein environment. However, at present, it is not possible to experimentally disentangle excitation dynamics from the many timescales of the vibrational bath, which include intramolecular pigment vibrations, fluctuations of neighboring amino acids, reorganization of proximate biological water, and reorganization of the bulk water solvent. Thus, quantitatively connecting the atomic scale motions of the pigment-protein environment to the dynamics of excitation transport in light-harvesting complexes remains a grand challenge at the interface of materials science and chemical physics.

It has long been speculated that simple design principles connect the complex atomic structure of pigment environments to the regulation of EET pathways in LHCs.[101–105] Recently, there has been growing interest in understanding the role of the vibrational environment in enhancing transport between energetically detuned pigments. The presence of a vibration with the same frequency as the pigment energy gap can enhance transport either coherently, via delocalization, or incoherently, via discrete hopping. Long-lived beat signals in nonlinear spectroscopic measurements of multiple LHCs have been interpreted as evidence for vibronic coherence, the delocalization of excited states between pigments (excitons) supported by a long-lived resonant vibration.[7,9–11,106–111] To

date, vibronic coherence has been proposed to enhance transport between energetically remote states in two excitation transport processes associated with light-harvesting: charge separation in the reaction center[9,10,106] and direct down-conversion in the bilin-containing protein PC645.[11] Here, we instead show that for phycobiliprotein PC645 an incoherent vibronic transport mechanism is at play. We find that flexible bilins, unlike rigid chlorophylls, exhibit large reorganization energies tuned by individual bilin-protein environments, suggesting that phycobiliproteins undergo incoherent energy transfer enhanced by the presence of a broad collection of high-frequency, intramolecular vibrations.

In vivo, PC645 absorbs high-energy photons and down-converts the excitation to facilitate efficient transfer to the reaction centers of photosystem I and II. Transient absorption measurements on isolated proteins reveal that photoexcitation of the high-energy core dihydrobiliverdins (DBVs, Figure 2.1a blue and green), is followed by transfer to the low-energy phycocyanobilin 82s (PCB82s, Figure 2.1a red and cyan), skipping the energetically intermediate mesobiliverdins (MBVs, Figure 2.1a brown and magenta).[112] Direct down-conversion cannot be explained by inter-pigment electronic couplings,[113] suggesting that the vibrational dynamics determined by local protein environments influence the pathways of EET.

Quantifying the ultrafast vibrational dynamics of specific chromophores in LHCs remains a challenge for both theory and experiment. Using a combination of linear and non-linear spectroscopic data, one can parameterize a model that describes the local vibrational environments of each pigment.[114] However, multiple distinct vibrational environments quickly lead to an intractable number of free parameters. Atomistic nuclear dynamics simulations have the potential to bypass the inverse problem[115–118] but have not previously managed to quantitatively reproduce spectroscopic signals, thus restricting their ability to inform on biological function.

For the first time, we successfully connect unique pigment-protein vibrational

environments to spectroscopic signals by incorporating pigment forces calculated with ground-state density functional theory (DFT). We extract bilin reorganization energies with a wider spread and larger average value than previously expected,[11,113,119] allowing for quantitative reproduction of linear spectra in the absence of free parameters. Additionally, our EET simulations yield transfer pathways and timescales in good agreement with experimental transient absorption measurements. To generalize our findings, we examine the simplest representative model system, a dimer with a resonant vibration, and define a ratio that distinguishes between the coherent and incoherent transport regimes. We find that transport between bilins in PC645 occurs incoherently, suggesting that Förster spectral overlaps tuned by local bilin-protein environments control EET and enable direct down-conversion.

2.3 Results and Discussion

2.3.1 *Ab Initio* Simulations of Protein Solvation Reproduce Linear Spectra

To understand the role of the local pigment environments in controlling EET, we first characterize the atomistic origin of the bilin solvation dynamics. The excitation energy of a pigment bound in a protein pocket, given as the difference between the ground and first excited state energies, fluctuates due to the nuclear motions of the chromophore, the surrounding protein residues, and the proximate water. Simulating excitation energy fluctuations requires performing nuclear dynamics that sample the ground-state potential energy surface (PES) and calculating the excitation energy at regular intervals. These fluctuations can be characterized by a spectral density that describes coupling of the electronic excited state to a continuous distribution of vibrational modes.[120] Given the significant computational cost of obtaining nuclear forces quantum mechanically (QM), previous calculations have always used classical or semi-empirical molecular mechanics

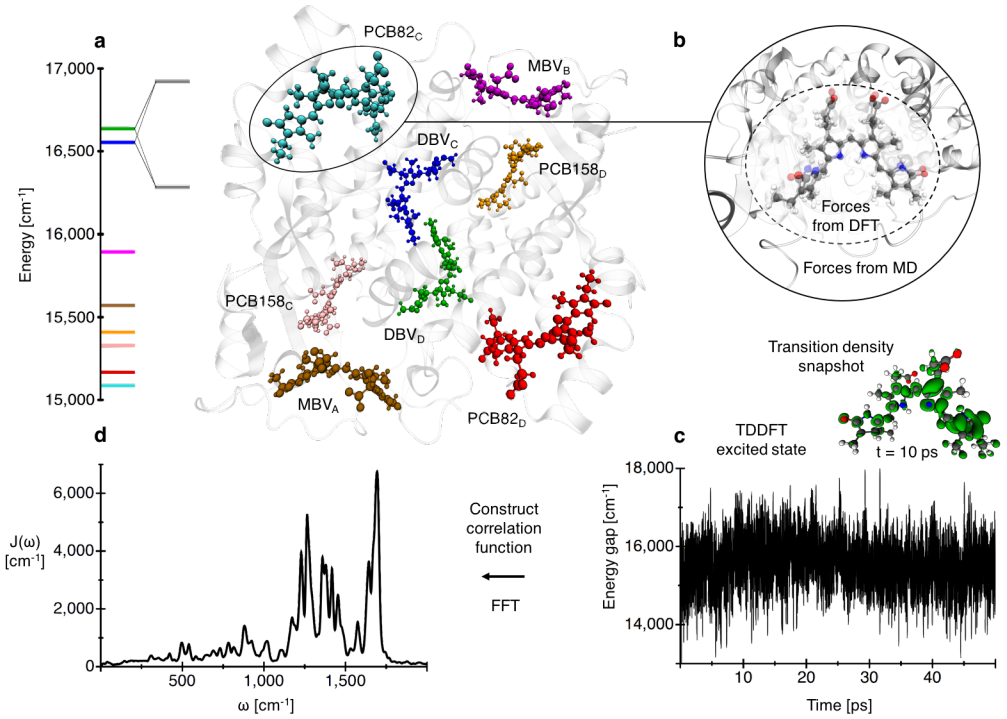

Figure 2.1: PC645 and computational methodology for spectral density construction. **a**, Structure and reorganized energy levels of PC645, where we have defined a bilin color scheme that remains consistent throughout. Gray lines in the energy level diagram are drawn schematically to represent the exciton eigenstates of the core DBVs (blue and green) due to the significant excitonic coupling of 319.4 cm^{-1}, more than three times larger than any other coupling in PC645. **b**, For each bilin, we simulate 50 ps of mixed QM/MM nuclear dynamics in which that bilin is treated quantum mechanically, while the remaining protein is treated with a classical force field. **c**, We construct energy-gap trajectories by calculating full TDDFT excited states for each bilin on geometries extracted at two femtosecond intervals from our QM/MM trajectories. **d**, We construct an energy-gap correlation function for each bilin and Fourier transform to obtain eight unique bilin spectral densities.

(MM) force fields to propagate nuclear dynamics for entire LHCs.[115–118,121] However, in many cases, the MM PES sampled during nuclear dynamics differs substantially from the QM PES on which excitation energies are defined, causing the calculated spectral densities to report incorrect vibrational frequencies and coupling amplitudes.[122]

We construct spectral densities using nuclear dynamics calculated on an *ab initio* QM/MM PES that combines bilin nuclear gradients calculated using DFT with an MM force field to treat the surrounding protein environment (Figure 2.1b), thereby resolving the mismatch between nuclear dynamics trajectories and excited state calculations.

Figure 2.1 provides an overview of our procedure for constructing spectral densities. For each bilin, we construct energy-gap trajectories (Figure 2.1c) by calculating excitation energies with time-dependent density functional theory (TDDFT) on 20,000 geometries extracted at two femtosecond intervals from our 40 picosecond (ps) QM/MM production runs. Fourier transforms of the two-time correlation functions of the energy-gap trajectories define unique spectral densities that characterize individual bilin environments (Figure 2.1d). We note that while TDDFT often incorrectly predicts absolute excitation energies, cancellation of error results in good descriptions of the curvature of the potential energy surface that we depend on here.[123–126]

Spectroscopic signals and EET dynamics depend intimately on the solvation dynamics of individual chromophores. The solvation capacity of the local vibrational environment is quantified by the total reorganization energy (λ) of the spectral density which measures the energy dissipated as the chromophore relaxes following excitation. Previous studies have assumed that all bilins have identical spectral densities and assigned a reorganization energy of either 260 cm^{-1},[119] 314 cm^{-1},[11] or 480 cm^{-1}.[113] Our spectral densities, shown in gray in the subpanels of Figure 2.2, reveal larger reorganization energies ($\langle\lambda\rangle$ = 909 cm^{-1}) and significant variations between different bilins. The spread in our reorganization energies (λ = 627 - 1414 cm^{-1}) is consistent with the presence of three chemically distinct bilins with different conjugation lengths and either one or two covalent protein linkages. The variability of the reorganization energies between chemically identical bilins bound in distinct protein environments (e.g. MBV_A and MBV_B) demonstrates the importance of the protein scaffold in determining the local solvation dynamics. On the other hand, all eight bilin spectral densities show a peak near 1650 cm^{-1} which is consistent with the assignment of a long-lived 1580 cm^{-1} mode as intramolecular C=C or C=N vibrations in broad-band transient absorption measurements.[11]

Incorporating the *ab initio* QM/MM spectral densities into absorption and fluorescence simulations (solid black lines) results in excellent agreement with experimental spectra

(open grey circles), as shown in Figure 2.2. We note that the negative features observed in simulated spectra are unphysical but do not impact the quality of the lineshapes (Figure 2.9). To account for both the large reorganization energies and the multiple timescales of vibrational relaxation encoded in the structure of our spectral densities, we employ numerically exact hierarchical equations of motion (HEOM),[12,13] implemented in QMaster.[14] HEOM has been shown to yield realistic simulations of exciton dynamics in LHCs,[26,127,128] but its computational complexity limits our spectral densities to including a total of 24 Drude-Lorentz peaks for full-system simulations, each representing a distributions of bath modes. We construct four classes of abridged spectral densities for each bilin starting with Class 1 (eight or nine peaks per bilin) and successively coarse-graining to incorporate fewer peaks until we reach Class 4 (two peaks per bilin). Peak parameters for all spectral densities are given in Table 2.1-2.5. Abridged spectral densities used for spectroscopic calculations are shown with our consistent bilin color scheme in the subpanels of Figure 2.2. We justify our abridged spectral densities by comparing simulated monomer absorption and fluorescence spectra, as described in supplementary information section 2.7.2. Supplementary information section 2.7.3 discusses the system Hamiltonian, *ab initio* transition dipole moments, details of the fluorescence simulations, and inhomogeneous broadening.

We validate our spectral densities by comparing to two features of the experimental spectra: the Stokes shift, defined as the frequency difference between the highest energy fluorescence peak and the lowest energy absorption peak, and the overall width of the absorption spectrum. Together, these observables are quite sensitive to the distribution of reorganization energies between the different bilins of PC645. Employing the lowest energy bilin spectral density for all pigments, such as would be extracted from a fluorescence line-narrowing experiment, results in an absorption spectrum with a full-width at half maximum (FWHM) that is 25% too small (Figure 2.10). The absorption spectrum contracts in this case because we underestimate the reorganization energies of

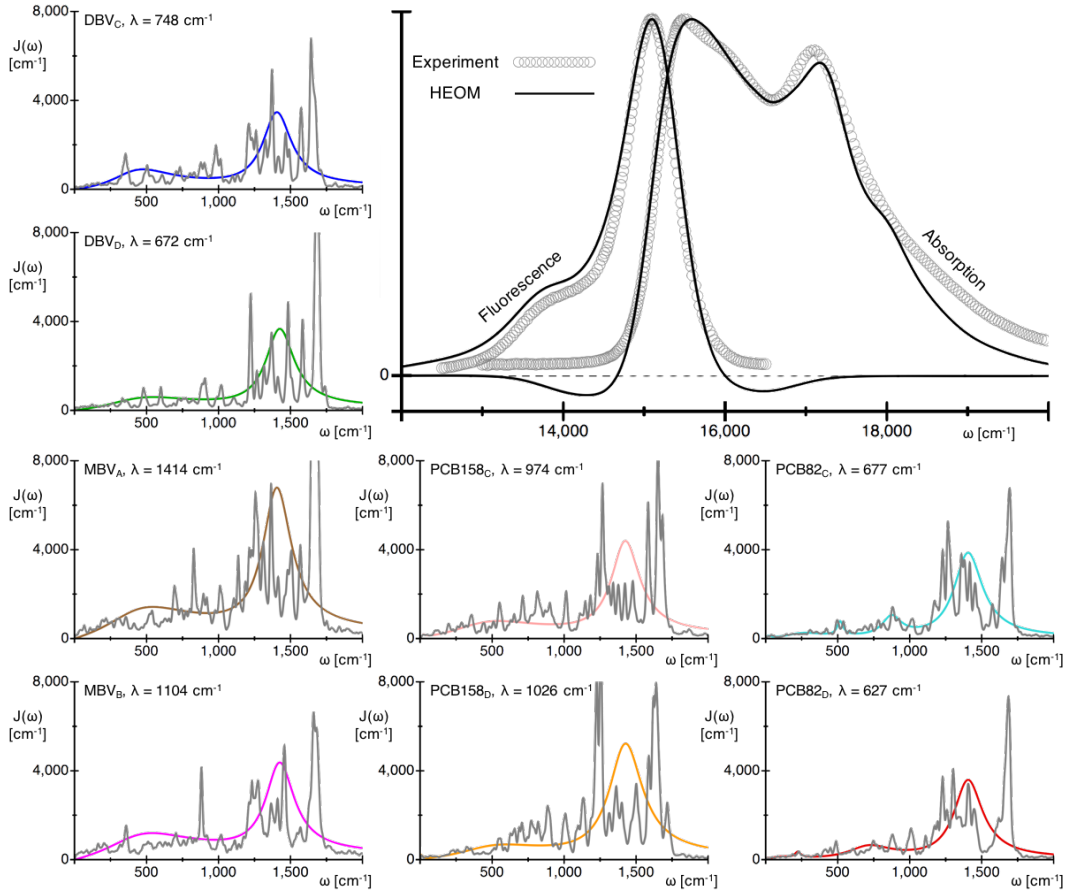

Figure 2.2: Comparison between absorption and fluorescence simulated with atomistic spectral densities and experimental spectra. Unabridged (gray) and abridged (colored) bilin spectral densities are shown in the subpanels, where the latter are used for spectroscopic simulations. Each spectral density panel is labeled with the bilin name and the calculated reorganization energy λ. The main panel compares the calculated absorption and fluorescence spectra (solid black lines) with experimental spectra (open circles).

the PCB158s and MBVs. If we instead use the average of the eight bilin spectral densities for all pigments, we obtain an absorption spectrum with a Stokes shift that is 55% too large (Figure 2.11). The Stokes shift expands because we substantially overestimate the reorganization energy of the PCB82s that dominate the fluorescence and low-energy absorption features. Thus, 18% error between the experimental and simulated Stokes shift and very good agreement with the overall absorption linewidth represents a strong validation of the solvation dynamics encoded in our atomistic spectral densities.

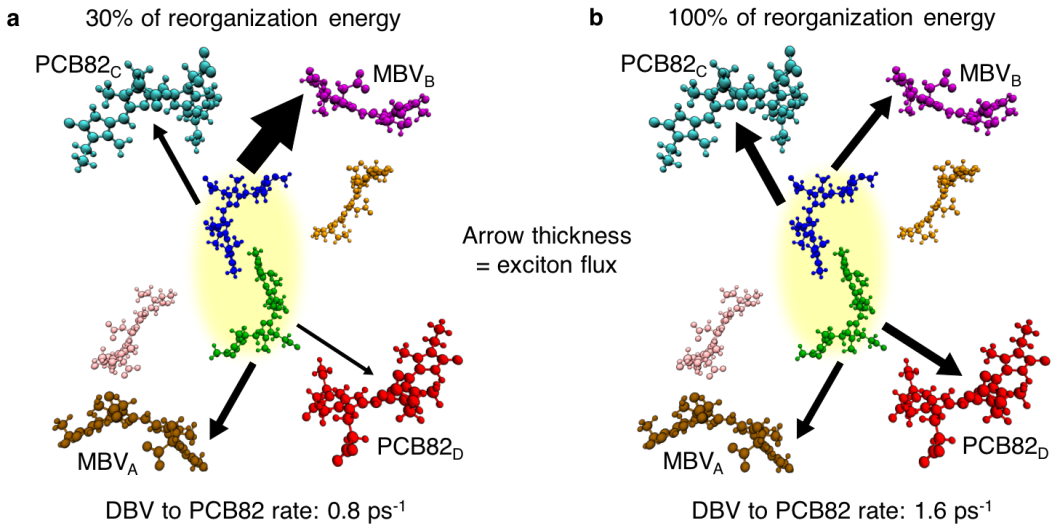

Figure 2.3: EET pathways and down-conversion rates simulated with HEOM. Arrow thickness is proportional to the exciton flux leaving the DBV core integrated over one picosecond after an initial photoexcitation with (**a**) 30% or (**b**) 100% of calculated reorganization energy. The corresponding rates from the DBV core to both PCB82s are reported below each panel.

To the best of our knowledge, in the absence of free parameters, Figure 2.2 represents the closest reported agreement between experimental lineshapes and *ab initio* simulations of absorption and fluorescence spectra for pigments in a heterogeneous environment.

2.3.2 Protein Solvation Drives Down-Conversion

The spectral density connects the atomistic dynamics of the bilin vibrational environment to both spectroscopic lineshapes and EET pertinent to light-harvesting. Having validated our atomistic QM/MM spectral densities against absorption and fluorescence spectra, we now confirm that they also describe the experimental observables associated with direct down-conversion in PC645. Experimental transient absorption measurements, combined with global kinetic analysis, indicate that initial excitation of the DBV core is followed by direct transport to the low-energy PCB82 pigments with a rate of 1.7 ps^{-1}.[11,112] Neither the rates nor selectivity of direct down-conversion have been successfully reproduced using previously estimated unstructured spectral densities.[119]

Here, we show that numerically exact HEOM simulations combined with our spectral densities predict pathways and rates of down-conversion that accurately reproduce experimental results.

The large reorganization energies of our QM/MM spectral densities are essential for correctly predicting the selectivity of transport from the DBV core to the low-energy PCB82s. Simulated EET pathways following photoexcitation of the DBV core are shown in Figure 2.3a and 2.3b. Arrow thickness in Figure 2.3 is proportional to exciton flux, the net amount of excitation that is transferred from the DBVs to an acceptor pigment in a 1.0 ps interval following photoexcitation. We perform exciton flux calculation using Class 2 spectral densities for the MBVs and Class 4 spectral densities for the remaining pigments (supplementary information section 2.7.2). In Figure 2.3a we rescale the spectral densities to match the average magnitude of reorganization energy used in previous simulations ($\langle\lambda\rangle = 260$ cm^{-1}, labeled 30%). In the presence of a smaller average reorganization energy, the more weakly solvated DBV core primarily transports excitation to the energetically adjacent MBV$_B$, qualitatively reproducing previous results.[119] EET simulations using the full reorganization energy (Figure 2.3b, labeled 100%), however, show enhanced direct transfer to the low-energy PCB82s, in reasonable agreement with global kinetic analysis of transient absorption measurements.

In addition to influencing selectivity, the large reorganization energies also increase the rate of direct down-conversion. HEOM is a non-Markovian theory, and as a result, the rates of transport vary as a function of time in response to changes in the vibrational energy distribution. We extract a best-fit rate of down-conversion from HEOM simulations using Class 1 spectral densities with a four-site model containing only the core DBVs and the low-energy PCB82s (supplementary information section 2.7.4). Class 1 spectral densities (e.g. Figure 2.6a) explicitly incorporate the high-frequency mode ($\sim$1650 cm^{-1}) previously assigned to an intramolecular bilin vibration. The rescaled spectral densities (Figure 2.3a, 30%) result in a transport rate of 0.8 ps^{-1}, substantially

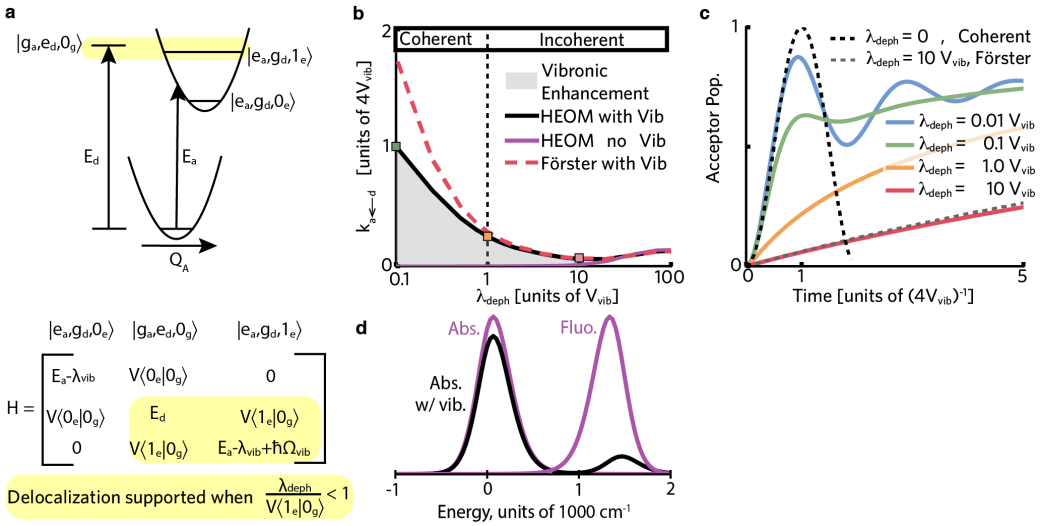

Figure 2.4: Regimes of coherent and incoherent vibronic transport. **a**, Energy levels of a detuned model dimer with a vibration on the acceptor pigment that is resonant with the site energy gap. The yellow shading represents the possible delocalization between the donor and the vibrationally excited acceptor states. **b**, Rate of transport from donor to acceptor as a function of the reorganization energy of the low-frequency background (λ_{deph}), where E_D - E_A = 250 cm^{-1}, V = 2.75 cm^{-1}, λ_{vib} = 24.7 cm^{-1}, Ω_{vib} = 274.7 cm^{-1}, and γ_{vib} = 0.125 cm^{-1}. Calculated rates of transport are shown for HEOM with a high-frequency vibration (HEOM with vib, solid black line), HEOM without vibration (HEOM no vib, solid purple line), and Förster with vibration (Förster with vib, dashed red line). The solid gray area represents the vibronic enhancement arising from the presence of the high-frequency vibration. The green, orange, and red squares represent the population dynamics shown in panel c. **c**, The acceptor population dynamics following the donor excitation are plotted for $\lambda_{deph} = 0.01, 0.1, 1,$ and 10 in blue, green, orange, and red, respectively. The first oscillation of purely coherent dynamics is plotted as a dashed black line. The population dynamics calculated using Förster theory for $\lambda_{deph} = 10$ is plotted as a dashed gray line. **d**, Mechanism of incoherent vibronic enhancement of transport, in which a nearly-resonant vibration can generate a vibronic sideband in the absorption (black) that can enhance overlap with the fluorescence. Absorption and fluorescence lineshapes in the absence of a high-frequency vibration are shown in purple.

slower than the experimentally observed 1.7 ps^{-1}. However, using the full reorganization energy of our spectral densities (Figure 2.3b, 100%), we find the simulated rate of transport to be 1.6 ps^{-1}, within 8% of the experimental value.

2.3.3 Down-Conversion Occurs via an Incoherent Vibronic Mechanism

We have demonstrated that HEOM simulations using our atomistic spectral densities reproduce both the linear spectra and the rate of direct down-conversion in PC645. However, the question remains: what are the mechanistic principles connecting bilin vibrational environments to regulation of EET pathways? In particular, the relative importance of short-lived, low-frequency, intermolecular motions versus long-lived, high-frequency, intramolecular vibrations remains controversial.[101,110] In this section, we assess how the mechanism of EET in PC645 arises from the interplay of inter-pigment couplings with structured spectral densities. First, we introduce the simplest representative model system that captures the essential features of vibronic transport in the presence of a long-lived high-frequency vibration and define a ratio that distinguishes between the coherent and incoherent transport regimes. Second, we demonstrate that PC645 experiences incoherent vibronic transport and that the long-lived near-resonant vibration assigned to support vibronic coherence is not essential for efficient transport. Finally, we show that generalized Förster theory[129–132] explains the mechanism of transport in PC645, consistent with recent work on other PPC aggregates,[14,133–136] and that local protein solvation enables direct down-conversion by controlling Förster spectral overlaps.

The transition from coherent to incoherent vibronic transport is governed by the ratio of the vibronic coupling (V_{vib}) to the rapidly relaxing component of the pigment reorganization energy (λ_{deph}). Figure 2.4a depicts an energetically detuned dimer with a long-lived resonant high-frequency vibration on the low-energy acceptor pigment (further details in supplementary section 2.7.5). In brief, we define the basis as a direct-product of three indices: the electronic state of the acceptor ($|g_a\rangle$, $|e_a\rangle$), the electronic state of the donor ($|g_d\rangle$, $|e_d\rangle$), and the vibrational state of the acceptor on either the ground- or excited-state harmonic oscillator ($|0_g\rangle$, $|0_e\rangle$, $|1_e\rangle$). Assuming the energy gap between the

donor ($|g_a, e_d, 0_g\rangle$) and the acceptor ($|e_a, g_d, 0_e\rangle$) is large compared to λ_{deph}, rapid excitation transport cannot occur (purple line, Figure 2.4b) unless a vibrationally excited acceptor state ($|e_a, g_d, 1_e\rangle$) is generated by a bridging high-frequency mode (black line, Figure 2.4b). Vibronic coupling (V_{vib}, eq. (2.1)) between the nearly degenerate states relevant for vibronic enhancement (gray area, Figure 2.4b) is described by the product of the electronic coupling (V) with the Frank-Condon factor.[137]

$$V_{vib} = V \cdot \langle 1_e | 0_g \rangle \sim V \cdot \sqrt{\frac{\lambda_{vib}}{\Omega_{vib}}} \tag{2.1}$$

The vibronic coupling (V_{vib}) facilitates delocalization between the donor and acceptor. In contrast, the component of the pigment reorganization energy that relaxes faster than the timescale of transport (λ_{deph}) drives excitations to localize on individual pigments.[138–140] Therefore, when $V_{vib} \gg \lambda_{deph}$, transport is coherent (i.e. aided by delocalization) and initial dynamics rise and oscillate (blue/green lines, Figure 2.4c) on a timescale determined by V_{vib} (black dashed line, Figure 2.4c). However, when $\lambda_{deph} \approx V_{vib}$ (orange line, Figure 2.4c) dynamic localization inhibits the initial coherent rise. Finally, when $\lambda_{deph} \gg V_{vib}$ (red line, Figure 2.4c) complete localizaton results in incoherent hopping that can be described by Förster theory,

$$K_{a \leftarrow d} = \frac{|V|^2}{\pi \hbar^2} \mathrm{Re}[\int_0^\infty A_a(t) F_d^*(t) dt] \tag{2.2}$$

where $A_a(t)$ is the absorption lineshape of the acceptor and $F_d(t)$ is the fluorescence lineshape of the donor. In the incoherent regime ($\lambda_{deph} \gg V_{vib}$) HEOM and Förster theory predict identical transport rates (red dashed line, Figure 2.4b) and dynamics (grey dashed line, Figure 2.4c), assuming vibrational relaxation is not too slow. Thus, the presence of a resonant, intramolecular vibration can enhance incoherent transport by providing a vibronic sideband that increases the absorption/fluorescence overlap[109,137] (Figure 2.4c). We note that the general conclusions drawn from this model hold whether

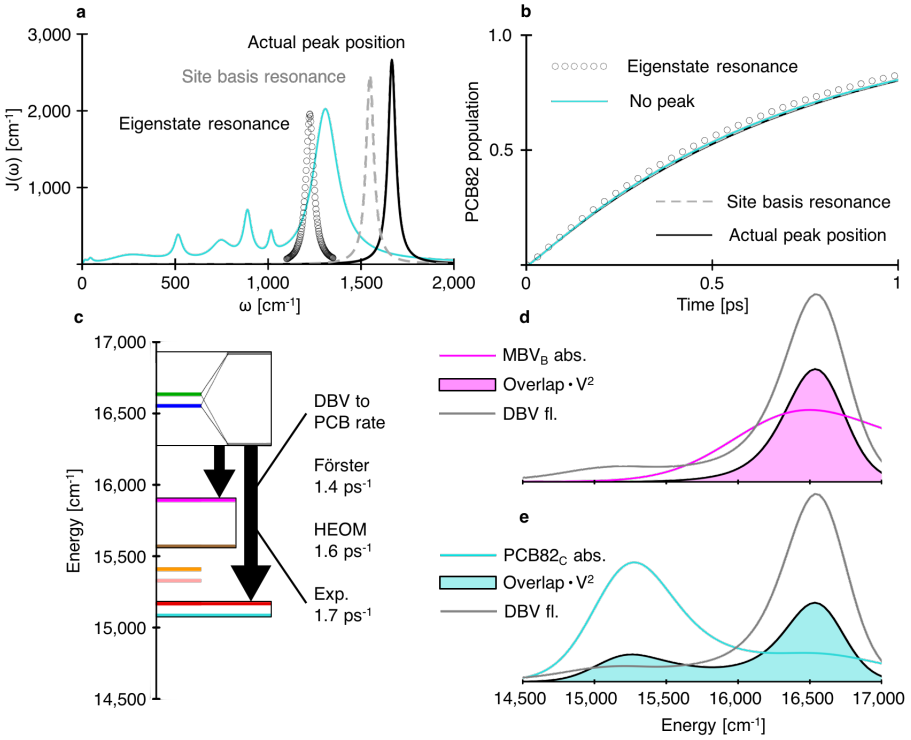

Figure 2.5: Direct down-conversion in PC645 is driven by incoherent vibronic transport. a, Four different PCB82$_C$ spectral densities that we use to examine the impact of the high-frequency vibration on direct down-conversion. While cyan represents the case where the high-frequency vibration has been removed entirely, it is also implicitly added to the following three cases in which the high-frequency vibration is shown by itself for clarity: the vibration in its original position in our QM/MM spectral densities (black), the vibration shifted to be in resonance with the DBV$_D$ - PCB82$_C$ site energy difference (1550 cm^{-1}, dashed gray), the vibration shifted to be in resonance with the low-energy DBV exciton - PCB82$_C$ energy difference (1220 cm^{-1}, black circles). Note that all four sites present in our population dynamics simulations use their individual spectral densities, but the changes to the high-frequency peak are equivalently applied to the other three sites. **b**, Population dynamics of a four-site system containing the DBVs and PCB82s. Lines representing the sum PCB82 population are labeled by their representation in panel a. **c**, An energetic depiction of down-conversion where site energies are fully reorganized and arrows represent the combined flux from the DBV core to the MBVs or PCB82s. The flux arrow from DBVs to PCB82s is labeled with the effective transport rate obtained from theory and experiment. Note that excitons are drawn schematically to represent DBV delocalization. **d**, Kubo monomer absorption for MBV$_B$ (magenta), Kubo DBV core fluorescence (gray), and absorption / fluorescence overlap weighted by the coupling to the lowest energy DBV exciton (outlined magenta). **e**, Kubo monomer absorption for PCB82$_C$ (cyan), Kubo DBV core fluorescence (gray), and absorption / fluorescence overlap weighted by the coupling to the lowest energy DBV exciton (outlined cyan).

or not the vibration is placed on the acceptor, the donor, or both (supplementary information section 2.7.5).

We find that direct down-conversion in PC645 occurs in the incoherent regime of vibronic transport. Limited delocalization between the DBVs due to their strong electronic coupling and the many timescales of vibrational relaxation complicates the assignment of both λ_{deph} ($\gg 250$ cm^{-1}) and the electronic coupling between the DBVs and PCB82s ($\sim$50 cm^{-1}), as described in supplementary information section 2.7.9. On the other hand, the high-frequency vibration on each of the DBVs and PCB82s has a Frank-Condon factor of $\sim$0.25, supporting a vibronic coupling of at most 12 cm^{-1}. Taken together, we find that the ratio of λ_{deph} to the vibronic coupling in PC645 has a lower bound of 20, indicating the dominance of incoherent transport. Thus, since the energy gap between the DBV fluorescence and PCB82 absorption maxima is larger than their peak widths (supplementary information section 2.7.9), we find that direct down-conversion in PC645 occurs in the incoherent vibronic regime. Given the order of magnitude difference between the lowest estimate of λ_{deph} and the vibronic coupling, our assignment of incoherent vibronic transport is robust to even substantial variation in Hamiltonian parameters (supplementary information section 2.7.12).

The presence of long-lived oscillations in nonlinear spectroscopic measurements led to the suggestion of functionally relevant vibronic coherence in PC645.[11] However, recent work has demonstrated that oscillatory vibronic signatures in 2D electronic spectra do not necessarily imply a role of vibronic coherence in excitation energy transfer.[141] We directly probe the role of vibronic coherence in PC645 by manipulating the high-frequency vibration previously assigned to support vibronic signatures and demonstrate that it is not required for efficient transport. Coherent vibronic transport is known to exhibit a sharp resonance condition as a function of the vibrational frequency.[10,11] The resonance condition arises because vibronic delocalization between the donor and the vibrationally excited acceptor only occurs when the energy gap is smaller than, or the same order of magnitude as, the vibronic coupling (i.e. $V_{vib} \sim 12$ cm^{-1}). In the case of PC645, partial delocalization in the DBVs means that there are two possible resonance conditions to

consider depending on whether the DBV core eigen- or pigment-states act as the donor. To explore the possible resonance conditions, we examine population dynamics calculated in a four-site model containing only the DBVs and PCB82s. We use Class 1 spectral densities with four possible positions of the high-frequency mode (Figure 2.5a): the original positions ($\sim$1650 cm^{-1}), the DBV$_D$-PCB82$_C$ site energy difference (1550 cm^{-1}), the low-energy DBV exciton-PCB82$_C$ energy difference (1220 cm^{-1}), and the complete removal of the high-frequency peak. We observe minimal differences in the resulting population dynamics (Figure 2.5b). An additional exhaustive scan of the peak position between 1100 cm^{-1} and 1800 cm^{-1} shows no greater variations in population dynamics. We have therefore demonstrated the absence of a sharp resonance condition, further supporting our assignment of incoherent vibronic transport.

Consistent with the incoherent transport regime, Förster theory captures the dominant contributions to the rate of down-conversion in PC645. In order to describe incoherent transport in the presence of strong coupling between DBVs, we use a generalization of Förster theory[129] that treats excitations within the DBV core as delocalized but assumes transport out of the core can be described as an incoherent hop. Due to rapid exciton relaxation within the DBV core, the rate of transport out of the core is determined by the overlap between the lowest-energy DBV exciton fluorescence and the absorption spectra of the remaining pigments. We simulate absorption spectra for the non-DBV pigments using Kubo lineshapes, which are exact for local excitations. We simulate the low-energy DBV exciton fluorescence using an extension of Kubo theory,[129,133,134] which neglects the localization of excitons resulting from vibrational fluctuations (Figure 2.15). Generalized Förster theory predicts a rate of 1.4 ps^{-1}, within 15% of the HEOM result (Figure 2.5c).

Using generalized Förster theory, we can explain the relative mechanistic role of low-frequency, intermolecular vibrations and high-frequency, intramolecular vibrations in controlling direct down-conversion in PC645. To understand the impact of bilin vibrational environments on transport rates and pathways, we examine the

absorption/fluorescence overlap between the DBV core (grey lines) and either PCB82$_C$ (cyan, Figure 2.5d) or MBV$_B$ (magenta, Figure 2.5e). The Stokes shift of the DBV core ($\sim$280 cm^{-1}) enhances the energetic overlap with the lower-energy pigments and dramatically increases the overall rates of transport. Despite almost perfect alignment of the DBV fluorescence with the MBV absorption spectra, excitation is preferentially transported to PCB82s due to the presence of broad vibronic sidebands. In contrast to the narrow resonance condition associated with coherent vibronic transport (width on the order of $|V\langle 1_e|0_g\rangle|$), the existence of wide absorption and fluorescence features allows for incoherent vibronic enhancement with a broad resonance condition (width on the order of the homogeneous linewidth). Finally, we note that given the importance of the Stokes shift in determining the rate and pathways of excitation transport, the demonstration of modified local solvation dynamics for chemically identical bilins within PC645 represents a potential design principle for nanoscale control of EET.

2.4 Conclusion

The inability to connect pigment-protein solvation dynamics and regimes of EET has previously concealed the underlying design principles at play in photosynthetic LHCs. We have demonstrated how specific features of the pigment vibrational environments in PC645 exert nanoscale control of EET pathways and enable direct down-conversion. We accessed the atomistic origin of local solvation for each bilin using *ab initio* QM/MM nuclear dynamics. Our simulations identified disparities between bilin vibrational environments, which had not been sucessfully extracted from experimental measurements, yielding excellent agreement with absorption and fluorescence spectra. In contrast to previous interpretations, we have identified that down-conversion proceeds via an incoherent vibronic transport mechanism where:

- excitations are localized on individual bilins (except for the DBV core) and transport occurs via incoherent hops,

- direct down-conversion is enhanced by large reorganization energies and the presence of a wide collection of high-frequency vibrations that induce broad vibronic sidebands.

Thus, our findings predict that coherent vibronic transport is not present in bilin-containing cryptophyte algal antenna complexes.

The incoherent vibronic mechanism assigned here to PC645 is far more robust to imperfections than its coherent counterpart and could act as a blueprint for the design of artificial excitonic materials. Recent advances in biomimetic light-harvesting technologies have demonstrated novel architectures, e.g. metal-organic frameworks (MOFs)[142] and DNA origami,[143] that can precisely place pigments within a hierarchically organized assembly. To fully realize nanoscale control of EET, we must iteratively simulate and design the local vibrational environments of pigment-scaffold architectures. However, the complexity of our current procedure is infeasible for high-throughput application, pointing towards the need for new and more efficient computational strategies and approximations.

2.5 Methods

We perform eight QM/MM nuclear dynamics simulations where the forces on one bilin are constructed from ground-state DFT calculations for each trajectory. We begin each QM/MM trajectory with 10 picoseconds of equilibration followed by 40 picoseconds of production run. We construct energy gap trajectories for each bilin using time-dependent density functional theory (TDDFT) calculations on geometries sampled every two femtoseconds, for a total of 20,000 geometries per bilin. We use the energy gap trajectories to construct two-time correlation functions and then Fourier transform to obtain the spectral density for each bilin. Overall, the eight 50 picosecond QM/MM trajectories took over nine months to run, and cost more than two million CPU hours. The details of the initial geometry preparation, separation of the quantum from classical regions, excited-state energy calculations, and the construction of the spectral densities is

described in supplementary information section 2.7.10.

Exciton dynamics simulations were performed with the QMaster software package[14] that provides a high-performance implementation of HEOM, which runs flexibly on both GPU and CPU architectures.[14,108,144] HEOM fluorescence calculations used a development version of QMaster. All HEOM results presented were run at a hierarchy depth of six except for rate calculations, which were run at a hierarchy depth of five (supplementary information section 2.7.4).

2.6 Acknowledgements

We gratefully acknowledge detailed discussions with and extensive commentary on the manuscript by Kapil Amarnath, as well as helpful conversations with Jacob Dean. We thank Thomas Markovich for help obtaining correlation functions and spectral densities. We acknowledge the Center for Excitonics, an Energy Frontier Research Center funded by the U.S. Department of Energy, Office of Science and Office of Basic Energy Sciences, under Award Number DE-SC0001088. S.M.B. acknowledges support from the United States Department of Energy through the Computational Sciences Graduate Fellowship (CSGF). D.I.G.B. and A.A.G. acknowledge the John Templeton Foundation (Grant Number 60469). D.I.G.B., A.A.G., and G.D.S. acknowledge CIFAR, the Canadian Institute for Advanced Research, for support through the Bio-Inspired Solar Energy program. This research used resources of the National Energy Research Scientific Computing Center, a DOE Office of Science User Facility supported by the Office of Science of the U.S. Department of Energy under Contract No. DE-AC02-05CH11231. We thank Nvidia for support via the Harvard CUDA Center of Excellence. This research used computational time on the Odyssey cluster, supported by the FAS Division of Science, Research Computing Group at Harvard University.

2.7 Supplementary Information

2.7.1 System Hamiltonian

We describe energy transfer using a Frenkel exciton Hamiltonian and assume that only one of the pigments is excited at a time. The Hamiltonian of the single exciton manifold reads

$$H_{\mathrm{ex}} = \sum_{m=1}^{N} \epsilon_m^0 |m\rangle\langle m| + \sum_{m>n} J_{mn}(|m\rangle\langle n| + |n\rangle\langle m|). \tag{2.3}$$

Here $|m\rangle$ denotes the state in which pigment m is excited while the other pigments remain in the electronic ground state. J_{mn} denotes the electronic coupling between the excited states on pigments m and n.

The pigments are coupled to the protein environment modeled by a set of independent harmonic oscillators

$$\mathcal{H}_{\mathrm{phon}} = \sum_{m,i} \hbar\omega_i b_{i,m}^\dagger b_{i,m}, \tag{2.4}$$

and we assume a linear coupling of the exciton system to the vibrations

$$\mathcal{H}_{\mathrm{ex-phon}} = \sum_m |m\rangle\langle m| \sum_i \hbar\omega_{i,m} d_{i,m}(b_{i,m} + b_{i,m}^\dagger). \tag{2.5}$$

The reorganization energy, $\lambda_m = \sum_i \hbar\omega_{i,m} d_{i,m}^2/2$, is added to the exciton energies in eqn (2.3), $\varepsilon_m = \varepsilon_m^0 + \lambda_m$. The phonon mode dependent coupling strength is captured by the spectral density

$$J_m(\omega) = \pi \sum_\xi \hbar^2 \omega_{\xi,m}^2 d_{\xi,m}^2 \delta(\omega - \omega_{\xi,m}) \tag{2.6}$$

which can also be defined as a sum of Drude-Lorentz peaks of form

$$J(\omega) = \sum_{i=1,s=\pm}^{N_{\mathrm{peaks}}} \frac{\lambda_i \gamma_i \omega}{2} \frac{1}{\gamma_i^2 + (\omega + s\,\Omega_i)^2}. \tag{2.7}$$

where λ_i is the peak reorganization energy, γ_i defines the peak width, Ω_i defines the center frequency, and β is the inverse temperature. The PC645 system Hamiltonian was

constructed by Mirkovich et. al[113] assuming an identical spectral density for all sites with a reorganization energy of 478.24 cm^{-1}. In order to combine the Mirkovich Hamiltonian with our spectral densities, we need to modify the diagonal elements, which denote the excited state energy of each chromophore plus the reorganization energy of that chromophore as defined above. To account for the reorganization energies of our unique spectral densities, we subtract off 478.24 cm^{-1} from each site energy and add the corresponding reorganization energy of that bilin's spectral density, preserving the underlying ϵ_m^0 values obtained previously.

2.7.2 Spectral Densities

While HEOM is numerically exact, large reorganization energy values require substantial hierarchy depth to ensure convergence. The particularly large reorganization energies of the MBVs require a depth of Nmax=6 for all full-system calculations presented in this manuscript, which restricts us to including a total of 24 bath modes over all eight sites and necessitates coarse graining of our spectral densities. We construct four classes of abridged spectral densities for each bilin that include successively fewer peaks. Construction is guided by four metrics:

- L1 and L2 norms of error between the abridged and unabridged spectral densities
- the relative distribution of reorganization energy along the frequency axis, e.g. how much of the reorganization energy is contained between 0 and 200 cm^{-1} versus between 200 and 400 cm^{-1}, etc
- monomer absorption and fluorescence lineshapes
- three-site population dynamics, including the core DBV bilins along with each other site in turn

We note that no experimental data of any kind was referenced during spectral density construction. Leveraging all five of these metrics simultaneously allows us to

systematically and optimally reduce complexity while preserving essential observables given the constraints.

We define the first and most accurate set of spectral densities as Class 1, and these include either eight or nine peaks depending on the bilin. Class 1 spectral densities have enough peaks to accurately capture the majority of the sharp features observed in the unabridged spectral densities, but contain too many bath modes to be applied to full-system calculations given the numerical complexity of the hierarchical equations of motion exciton dynamics method. Class 2 spectral densities include either five or six peaks depending on the bilin and therefore can only accurately represent some of the sharp features observed in the unabridged spectral densities. Despite the limitations, simulations with Class 2 spectral densities are able to accurately reproduce absorption, fluorescence, and population dynamics obtained from simulations with the more accurate Class 1 spectral densities. Class 3 and Class 4 spectral densities contain three and two peaks, respectively, and cannot accurately capture any of the sharp features observed in the unabridged spectral densities. Spectral densities of all four classes for $PCB82_C$ are shown in Figure 2.6, while spectral density parameters for all classes and all bilins are given below in Table 2.1-2.5.

We construct Class 1 spectral densities by trying to minimize L1 and L2 error with respect to the unabridged spectral densities while also preserving the relative distribution of reorganization energy. Class 1 spectral densities are too complex for use in full-system calculations, but we can use them to run monomer HEOM calculations up to a hierarchy depth of Nmax=12 for precise convergence. As seen in Figure 2.7, for $PCB82_C$, monomer simulations with the Class 2 spectral density (blue) are able to reproduce absorption and fluorescence lineshapes and Stokes shift obtained from simulations with the Class 1 spectral density (red). While the Class 3 and Class 4 spectral densities cannot reproduce the lineshape or Stokes shift, the addition of a peak near zero frequency in Class 3 compared with Class 4 dramatically improves both observables, as shown in Figure 2.7.

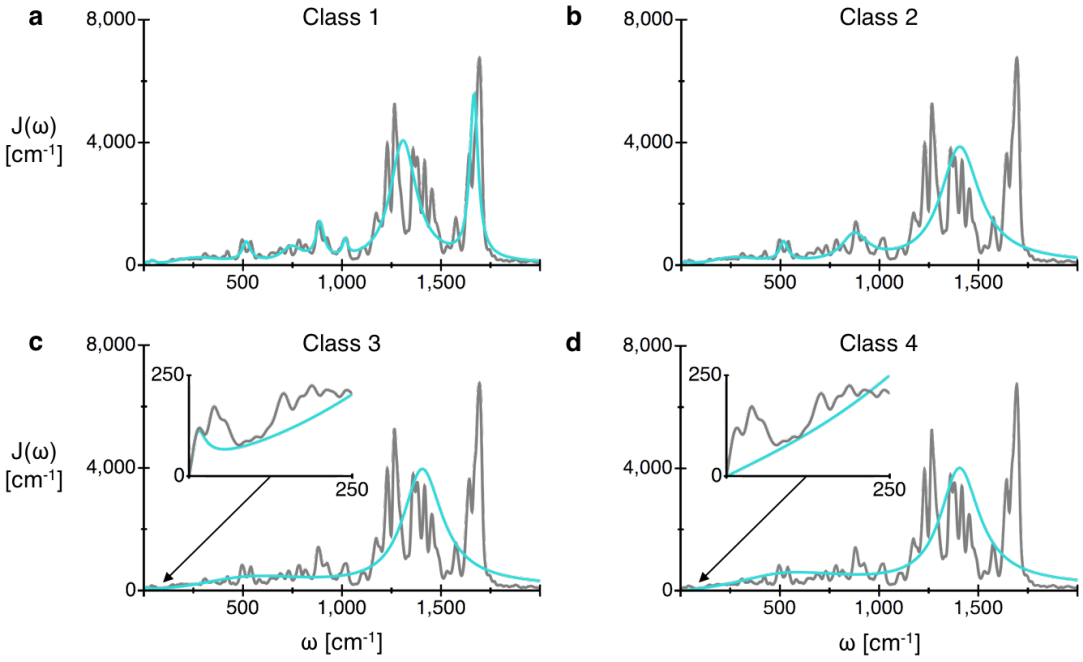

Figure 2.6: Four spectral density classes for $PCB82_C$. **a**, Class 1, nine peaks. **b**, Class 2, five peaks. **c**, Class 3, three peaks. **d**, Class 4, two peaks.

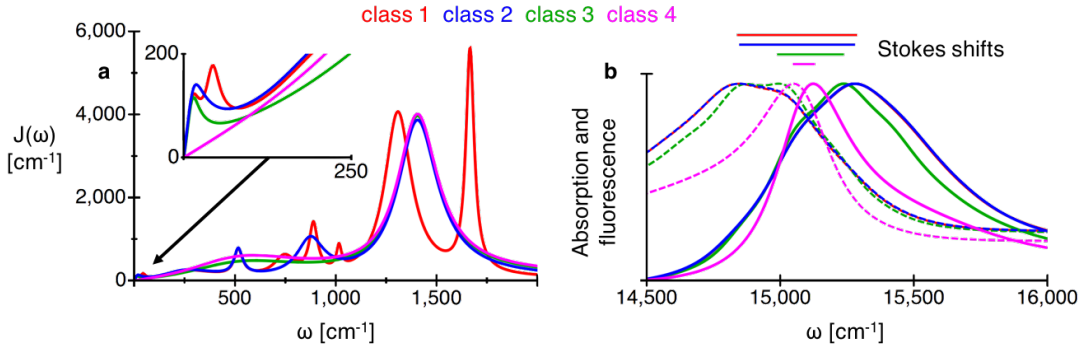

Figure 2.7: Monomer absorption and fluorescence. **a**, All four classes of spectral densities for $PCB82_C$ with Class 1 (nine peaks) shown in red, Class 2 (five peaks) shown in blue, Class 3 (three peaks) shown in green, and Class 4 (two peaks) shown in magenta. **b**, Monomer absorption (solid) and fluorescence (dashed) calculated with HEOM using the four classes of spectral densities. Stokes shifts are depicted graphically above.

This demonstrates the importance of accurately capturing the pure dephasing rate, which is defined as the spectral density slope at zero frequency, since it directly impacts the optical dephasing time which influences Stokes shift. We were able to obtain Class 2

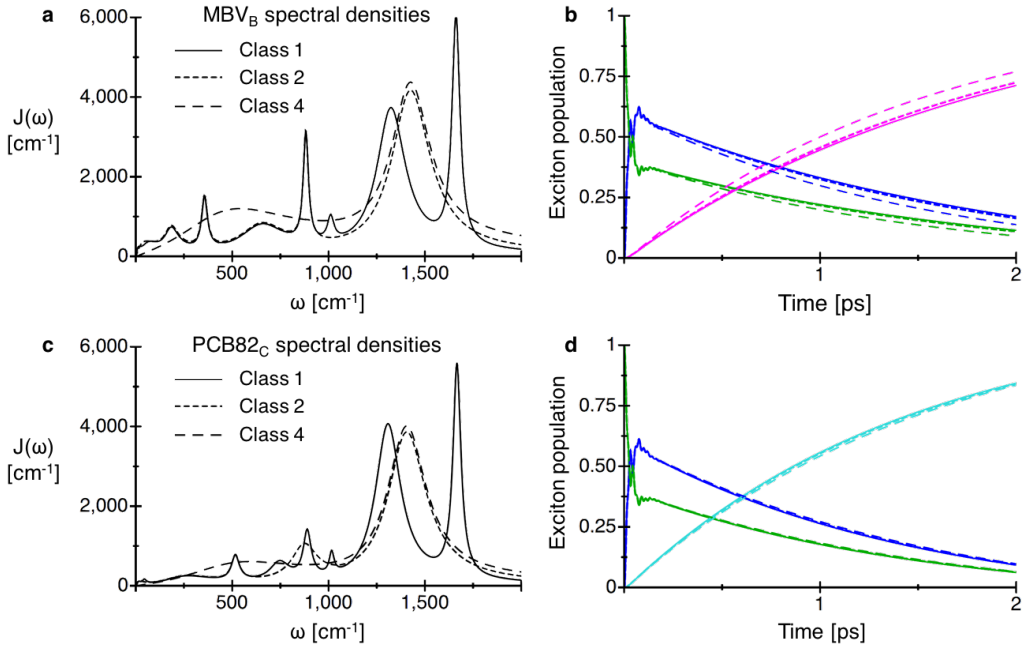

Figure 2.8: Three-site population dynamics. **a**, Three classes of MBV_B spectral densities with Class 1 shown in solid, Class 2 shown in short dashed, and Class 4 shown in long dashed. We note that Class 3 have dynamics identical to Class 4 spectral densities. **b**, Three-site population dynamics from the DBV core (blue and green) to MBV_B (magenta) using the three different classes of spectral density for the MBV_B, while Class 4 spectral densities were used for the DBV core. **c**, Three classes of $PCB82_C$ spectral densities with Class 1 shown in solid, Class 2 shown in short dashed, and Class 4 shown in long dashed. **d**, Three-site population dynamics from the DBV core (blue and green) to $PCB82_C$ (cyan) using the three different classes of spectral density for the $PCB82_C$ while Class 4 spectral densities were used for the DBV core.

spectral densities that accurately reproduced both lineshape and Stokes shift obtained from Class 1 spectral densities for all eight bilins. As seen in Figure 2.8, while we found population dynamics to be less sensitive to spectral density structure compared with spectroscopy, MBV bilin population dynamics in particular remained susceptible to changes in the spectral density structure. Therefore, full system population dynamics and population flux simulations presented in the main text use Class 2 spectral densities for MBVs and Class 4 spectral densities for all other bilins.

$\mathbf{DBV_C}$			$\mathbf{DBV_D}$		
$\lambda(cm^{-1})$	$\gamma(cm^{-1})$	$\Omega(cm^{-1})$	$\lambda(cm^{-1})$	$\gamma(cm^{-1})$	$\Omega(cm^{-1})$
95.8	7.50	5.95	114.0	10.50	4.0
148.2	90.00	110.0	120.0	70.00	80.0
63.0	16.00	352.0	52.0	50.00	310.0
50.0	37.00	540.0	24.2	13.00	480.0
40.0	40.00	740.0	15.4	12.00	599.0
71.6	55.00	945.0	70.0	55.00	898.0
183.6	80.00	1330.0	186.6	80.00	1370.0
96.0	30.00	1620.0	90.4	25.00	1660.0
$\mathbf{MBV_A}$			$\mathbf{MBV_B}$		
$\lambda(cm^{-1})$	$\gamma(cm^{-1})$	$\Omega(cm^{-1})$	$\lambda(cm^{-1})$	$\gamma(cm^{-1})$	$\Omega(cm^{-1})$
107.4	6.50	5.0	162.0	10.20	7.0
268.0	40.00	60.0	200.0	50.00	53.0
264.0	100.00	255.0	131.0	43.00	180.0
48.0	30.00	530.0	66.0	18.00	355.0
200.0	80.00	800.0	150.6	140.00	643.0
20.0	14.00	1010.0	50.0	16.00	881.0
376.0	90.00	1300.0	12.0	20.00	1010.0
160.0	25.00	1640.0	245.8	90.00	1320.0
			86.0	25.00	1660.0

Table 2.1: Class 1 spectral density parameters for DBVs and MBVs.

$\mathbf{PCB158_C}$			$\mathbf{PCB158_D}$		
$\lambda(cm^{-1})$	$\gamma(cm^{-1})$	$\Omega(cm^{-1})$	$\lambda(cm^{-1})$	$\gamma(cm^{-1})$	$\Omega(cm^{-1})$
128.0	15.00	14.0	154.0	7.50	6.0
80.0	30.00	105.0	60.8	34.00	69.0
46.0	18.00	197.0	110.6	72.00	275.0
118.0	55.00	330.0	24.0	20.00	545.0
56.0	25.00	550.0	150.0	84.00	725.0
185.2	88.00	780.0	24.0	15.00	888.0
14.0	9.00	1014.0	12.0	10.00	1005.0
242.2	80.00	1300.0	332.6	80.00	1260.0
104.6	23.00	1635.0	158.0	60.00	1600.0
$\mathbf{PCB82_C}$			$\mathbf{PCB82_D}$		
$\lambda(cm^{-1})$	$\gamma(cm^{-1})$	$\Omega(cm^{-1})$	$\lambda(cm^{-1})$	$\gamma(cm^{-1})$	$\Omega(cm^{-1})$
79.6	10.50	9.5	63.4	8.00	5.0
30.4	12.00	42.0	92.0	80.00	70.0
131.2	150.00	223.0	28.0	24.50	220.0
30.0	25.00	515.0	70.0	80.00	488.0
40.0	62.00	743.0	58.0	65.00	810.0
33.0	25.00	888.0	16.0	16.00	1009.0
8.0	15.00	1015.0	220.0	80.00	1305.0
244.8	80.00	1305.0	80.0	22.00	1675.0
80.0	25.00	1665.0			

Table 2.2: Class 1 spectral density parameters for PCBs.

$\mathbf{DBV_C}$			$\mathbf{DBV_D}$		
$\lambda(cm^{-1})$	$\gamma(cm^{-1})$	$\Omega(cm^{-1})$	$\lambda(cm^{-1})$	$\gamma(cm^{-1})$	$\Omega(cm^{-1})$
244.0	90.00	0.0	234.0	80.00	0.0
63.0	16.00	352.0	52.0	40.00	310.0
50.0	37.00	540.0	20.2	13.00	480.0
40.0	40.00	740.0	15.4	12.00	599.0
71.6	55.00	945.0	70.0	55.00	898.0
279.6	120.00	1400.0	281.0	120.00	1420.0
$\mathbf{MBV_A}$			$\mathbf{MBV_B}$		
$\lambda(cm^{-1})$	$\gamma(cm^{-1})$	$\Omega(cm^{-1})$	$\lambda(cm^{-1})$	$\gamma(cm^{-1})$	$\Omega(cm^{-1})$
375.4	50.00	0.0	362.0	50.00	0.0
264.0	100.00	255.0	131.0	43.00	180.0
48.0	30.00	530.0	66.0	18.00	355.0
40.0	18.00	695.0	150.6	140.00	643.0
180.0	80.00	900.0	50.0	16.00	881.0
536.0	120.00	1400.0	343.8	120.00	1420.0
$\mathbf{PCB158_C}$			$\mathbf{PCB158_D}$		
$\lambda(cm^{-1})$	$\gamma(cm^{-1})$	$\Omega(cm^{-1})$	$\lambda(cm^{-1})$	$\gamma(cm^{-1})$	$\Omega(cm^{-1})$
128.0	15.00	14.0	214.8	34.00	0.0
80.0	30.00	105.0	110.6	72.00	275.0
164.0	55.00	300.0	24.0	20.00	545.0
56.0	25.00	550.0	174.0	84.00	750.0
199.2	100.00	810.0	12.0	10.00	1005.0
346.8	120.00	1420.0	490.6	140.00	1420.0
$\mathbf{PCB82_C}$			$\mathbf{PCB82_D}$		
$\lambda(cm^{-1})$	$\gamma(cm^{-1})$	$\Omega(cm^{-1})$	$\lambda(cm^{-1})$	$\gamma(cm^{-1})$	$\Omega(cm^{-1})$
110.0	15.00	9.5	63.4	8.00	5.0
131.2	150.00	223.0	92.0	80.00	70.0
30.0	25.00	515.0	28.0	24.50	220.0
81.0	80.00	870.0	144.0	180.00	700.0
324.8	120.00	1400.0	300.0	120.00	1400.0

Table 2.3: Class 2 spectral density parameters.

$\mathbf{DBV_C}$			$\mathbf{DBV_D}$		
$\lambda(cm^{-1})$	$\gamma(cm^{-1})$	$\Omega(cm^{-1})$	$\lambda(cm^{-1})$	$\gamma(cm^{-1})$	$\Omega(cm^{-1})$
95.8	7.50	5.95	114.0	10.50	4.0
372.8	250.00	400.0	267.0	350.00	400.0
279.6	120.00	1400.0	291.6	120.00	1420.0
$\mathbf{MBV_A}$			$\mathbf{MBV_B}$		
$\lambda(cm^{-1})$	$\gamma(cm^{-1})$	$\Omega(cm^{-1})$	$\lambda(cm^{-1})$	$\gamma(cm^{-1})$	$\Omega(cm^{-1})$
107.4	6.50	5.0	162.0	10.20	7.0
800.0	350.00	400.0	609.6	350.00	400.0
536.0	120.00	1400.0	331.8	120.00	1420.0
$\mathbf{PCB158_C}$			$\mathbf{PCB158_D}$		
$\lambda(cm^{-1})$	$\gamma(cm^{-1})$	$\Omega(cm^{-1})$	$\lambda(cm^{-1})$	$\gamma(cm^{-1})$	$\Omega(cm^{-1})$
128.0	15.00	14.0	154.0	7.50	6.0
499.2	350.00	400.0	381.4	350.00	450.0
346.8	120.00	1420.0	490.6	140.00	1420.0
$\mathbf{PCB82_C}$			$\mathbf{PCB82_D}$		
$\lambda(cm^{-1})$	$\gamma(cm^{-1})$	$\Omega(cm^{-1})$	$\lambda(cm^{-1})$	$\gamma(cm^{-1})$	$\Omega(cm^{-1})$
79.6	10.50	9.5	63.4	8.00	5.0
272.6	350.00	450.0	264.0	350.00	450.0
324.8	120.00	1400.0	300.0	120.00	1400.0

Table 2.4: Class 3 spectral density parameters.

$\mathbf{DBV_C}$			$\mathbf{DBV_D}$		
$\lambda(cm^{-1})$	$\gamma(cm^{-1})$	$\Omega(cm^{-1})$	$\lambda(cm^{-1})$	$\gamma(cm^{-1})$	$\Omega(cm^{-1})$
468.6	250.00	400.0	381.0	350.00	400.0
279.6	120.00	1400.0	291.6	120.00	1420.0
$\mathbf{MBV_A}$			$\mathbf{MBV_B}$		
$\lambda(cm^{-1})$	$\gamma(cm^{-1})$	$\Omega(cm^{-1})$	$\lambda(cm^{-1})$	$\gamma(cm^{-1})$	$\Omega(cm^{-1})$
907.4	350.00	400.0	771.6	350.00	400.0
536.0	120.00	1400.0	331.8	120.00	1420.0
$\mathbf{PCB158_C}$			$\mathbf{PCB158_D}$		
$\lambda(cm^{-1})$	$\gamma(cm^{-1})$	$\Omega(cm^{-1})$	$\lambda(cm^{-1})$	$\gamma(cm^{-1})$	$\Omega(cm^{-1})$
627.2	350.00	400.0	535.4	350.00	450.0
346.8	120.00	1420.0	490.6	140.00	1420.0
$\mathbf{PCB82_C}$			$\mathbf{PCB82_D}$		
$\lambda(cm^{-1})$	$\gamma(cm^{-1})$	$\Omega(cm^{-1})$	$\lambda(cm^{-1})$	$\gamma(cm^{-1})$	$\Omega(cm^{-1})$
352.2	350.00	450.0	327.4	350.00	450.0
324.8	120.00	1400.0	300.0	120.00	1400.0

Table 2.5: Class 4 spectral density parameters.

2.7.3 Spectroscopy

Ab initio transition dipole moments for each bilin, necessary for accurate spectroscopic simulations, were obtained from TDDFT calculations and averaged over bilin trajectories. Our eight transition dipole vectors are given in Table 2.6.

Inhomogeneous broadening was accounted for in absorption and fluorescence simulations by averaging 100 calculations in which each bilin excitation energy was perturbed by a value drawn randomly from a Gaussian distribution with a width of 150 cm^{-1}. This width was selected to be approximately the average of the inhomogeneous line broadening values used by Mirkovich et. al.[113]

Fluorescence results presented in the main text are Boltzmann weighted sums of monomer fluorescence calculations run with HEOM at a hierarchy depth of Nmax=12. The additional computational complexity of fluorescence compared to absorption prevents full system simulations from achieving convergence in the hierarchy. Calculations

Bilin	$\mathbf{L_x}$	$\mathbf{L_y}$	$\mathbf{L_z}$
DBV_C	1.316	3.062	3.082
DBV_D	0.794	3.260	2.604
MBV_A	0.882	3.535	-2.359
MBV_B	0.072	-3.517	2.947
$PCB158_C$	3.414	0.195	2.944
$PCB158_D$	3.304	-1.780	-2.438
$PCB82_C$	0.935	-1.908	4.243
$PCB82_D$	1.949	0.365	-4.359

Table 2.6: Transition dipole vectors given in atomic units.

including only the four lowest energy bilins, the PCB158s and PCB82s, are feasible and reasonably accurate given that fluorescence spectra are dominated by the response of low energy sites. We observed that four-site calculations are indistinguishable from a Boltzmann weighted sum of four monomer lineshapes. Therefore, we present monomer-based results that allow larger Nmax values.

Absorption and fluorescence spectra presented in the main text can be seen to go slightly below zero amplitude, which is unphysical. We expect negative features arise due to the high-temperature approximation made by the QMaster implementation of HEOM. In order to ensure that negative features are not impacting the overall lineshape, we compared HEOM monomer absorption and fluorescence spectra to Kubo lineshapes, which are exact for monomers, shown in Figure 2.9. Monomer calculations employed Class 1 spectral densities, and the HEOM calculations were run at a hierarchy depth of Nmax=12. While HEOM lineshapes appear to be slightly too narrow, their features remain minimally perturbed by negative features.

Absorption and fluorescence spectra are highly sensitive to spectral density structures and pigment reorganization energies. Due to experimental constraints, spectral densities of the lowest energy bilins, such as would be extracted from fluorescence line narrowing, are often used for all pigments. However, if we employ $PCB82_C$ spectral densities for all

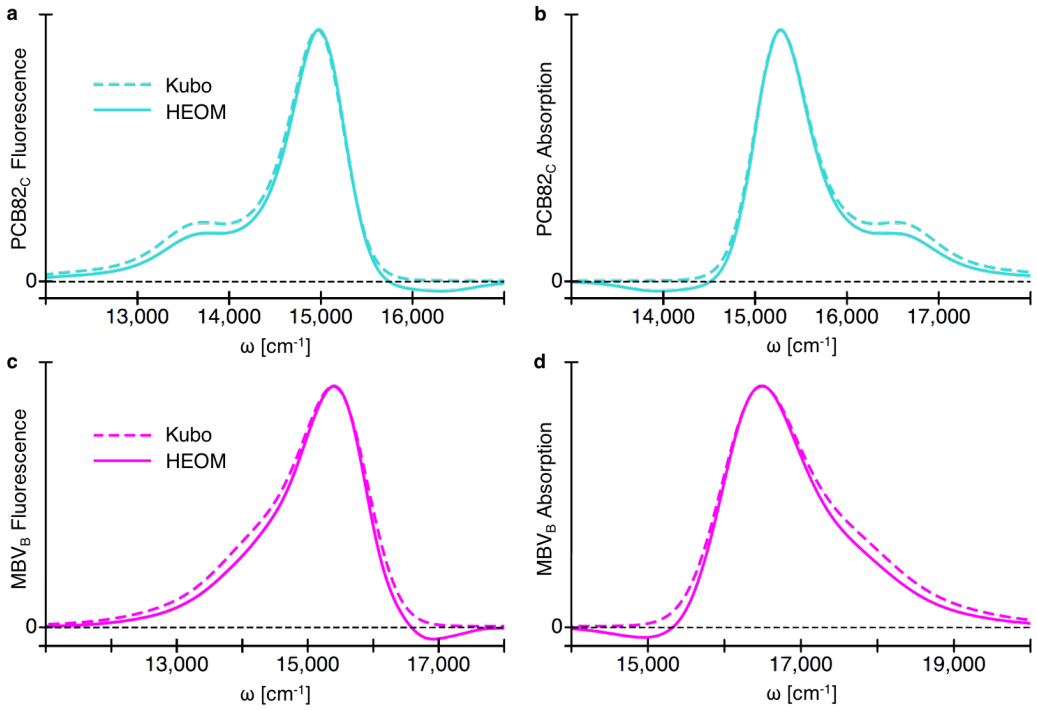

Figure 2.9: Comparing monomer lineshapes. Monomer Kubo absorption and fluorescence (dashed) are compared to monomer HEOM absorption and fluorescence (solid) for two representative bilins, MBV_B (magenta) and $PCB82_C$ (cyan).

pigments, we obtain an absorption spectrum with a full-width at half maximum 25% too small, as seen in Figure 2.10. The decreased spectral width is due to the reduced reorganization energy of the high-energy MBVs and DBVs, while the Stokes shift remains accurate given that the reorganization energies of the PCB82s remain essentially unchanged. In order to present a fair comparison with our non-identical spectra, Class 4 $PCB82_C$ spectral densities were used for MBVs and DBVs, Class 3 $PCB82_C$ spectral densities were used for PCB158s, and Class 2 $PCB82_C$ spectral densities were used for PCB82s.

In contrast, if we employ the average of the eight bilin spectral densities for all pigments, we obtain an absorption spectrum that overestimates the Stokes shift by 55%, as seen in Figure 2.11. The larger Stokes shift follows from the increase in the reorganization energy of our lowest energy pigments when using the average spectral

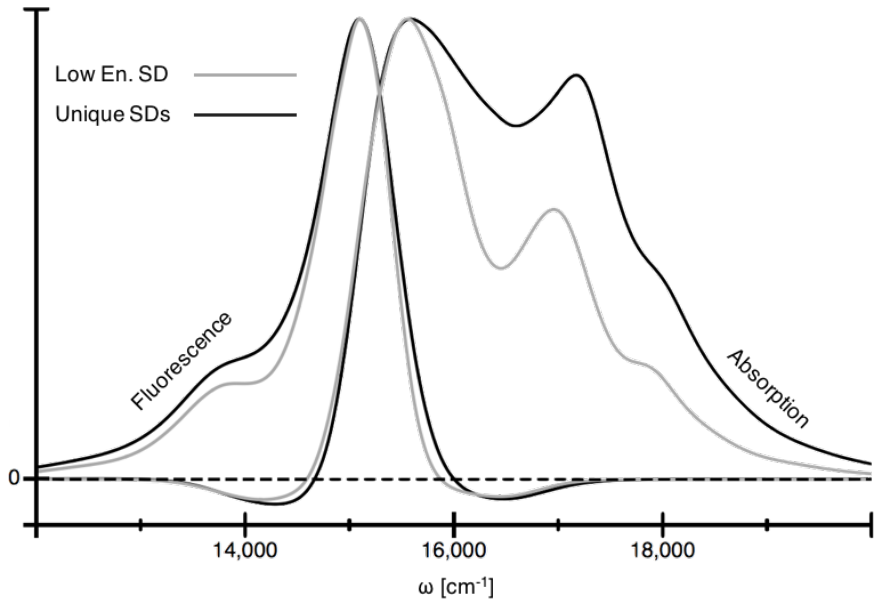

Figure 2.10: The sensitivity of linear spectra to spectral densities: low energy SDs. Absorption and fluorescence spectra using spectral densities from the lowest energy bilin $PCB82_C$ (gray) compared with those using unique spectral densities (black).

density. We note that average spectral densities were made by averaging the eight raw bilin spectral densities and then using the same construction procedure to obtain the four spectral density classes as detailed previously. Once again, in order to present a fair comparison with our non-identical spectra, Class 4 average spectral densities were used for MBVs and DBVs, Class 3 average spectral densities were used for PCB158s, and Class 2 average spectral densities were used for PCB82s.

We note that in both of the examples presented, Hamiltonian site energies were adjusted according to the reorganization energies in order to continue to preserve the underlying ϵ_m^0 values. While many different sets of spectral densities could in principle yield reasonable absorption and fluorescence spectra, the significant spectroscopic error introduced when employing two common approximations provides further evidence that our spectral densities and their associated reorganization energies have accurately captured physically relevant details of individual bilin vibrational environments in PC645. Finally, we note that for both the examples presented here and the spectra presented in

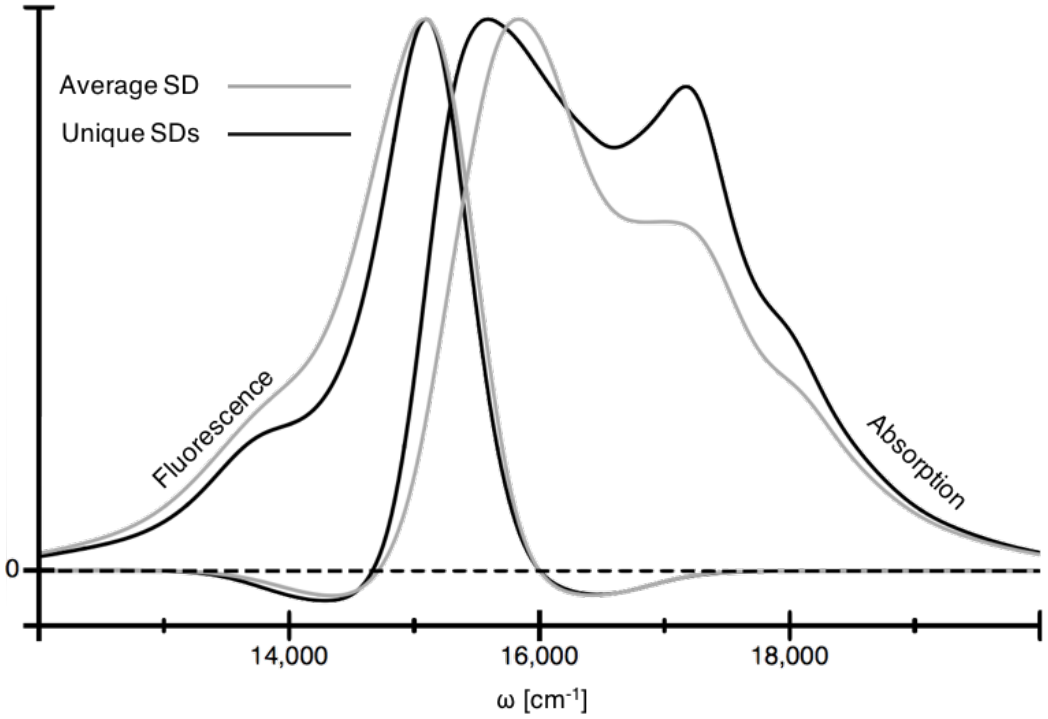

Figure 2.11: The sensitivity of linear spectra to spectral densities: average SDs. Absorption and fluorescence spectra using average spectral densities (gray) compared with those using unique spectral densities (black).

the main text, an additional 85 cm^{-1} was added to all site energies to ensure alignment with the experimental fluorescence peak. This has no impact on the Stokes shift or the absorption lineshape that we depend on to validate our spectral densities.

2.7.4 Dynamics

Figure 2.12 shows one picosecond of full system population dynamics calculated at a hierarchy depth of Nmax=6. The exciton is initially localized on the highest energy bilin, DBV_D (green), and can be seen to rapidly delocalize over the DBV core (blue and green) before down-converting to the low energy PCB82s (cyan and red). The minimal populations of the intermediate MBVs (magenta and brown) represent an improvement over previous simulations of PC645 exciton dynamics[119] given the better agreement with

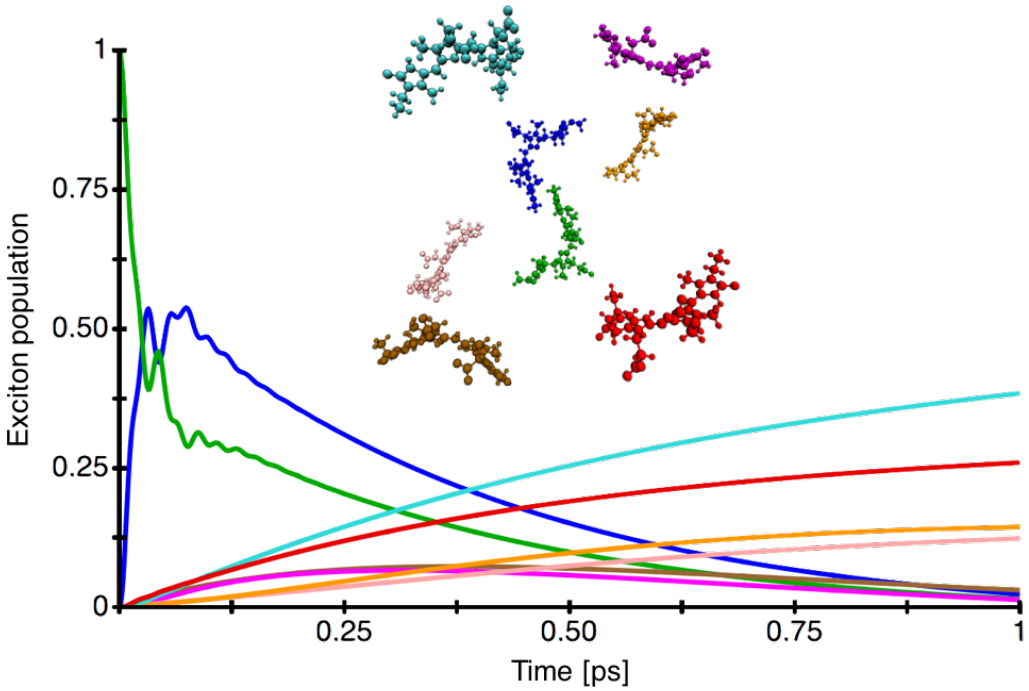

Figure 2.12: Full system population dynamics. One picosecond of population dynamics calculated with Class 2 spectral densities (six peaks) on the MBVs (brown and magenta) and Class 4 spectral densities (two peaks) on all other sites.

experimental transient absorption measurements.[112]

We perform four-site HEOM population dynamics simulations including the DBV core and the low energy PCB82s in order to isolate the DBV to PCB transfer rate. The populations of the two DBVs and the two PCB82s are summed separately in order to obtain a dimer-like system from which we extract rates as per Dijkstra et. al.[145] Summed populations obtained from HEOM calculations are compared to populations obtained from resulting rate equations in Figure 2.13 and are found to agree with minimal error.

We calculate rates in this way at a range of scaled reorganization energies and using two different classes of spectral densities to further demonstrate the importance of our large reorganization values and of resolved spectral density features for accurate rate prediction. As seen in Figure 2.14, the rate in best agreement with experiment is obtained at our full reorganization energy and with the more accurate Class 2 spectral densities.

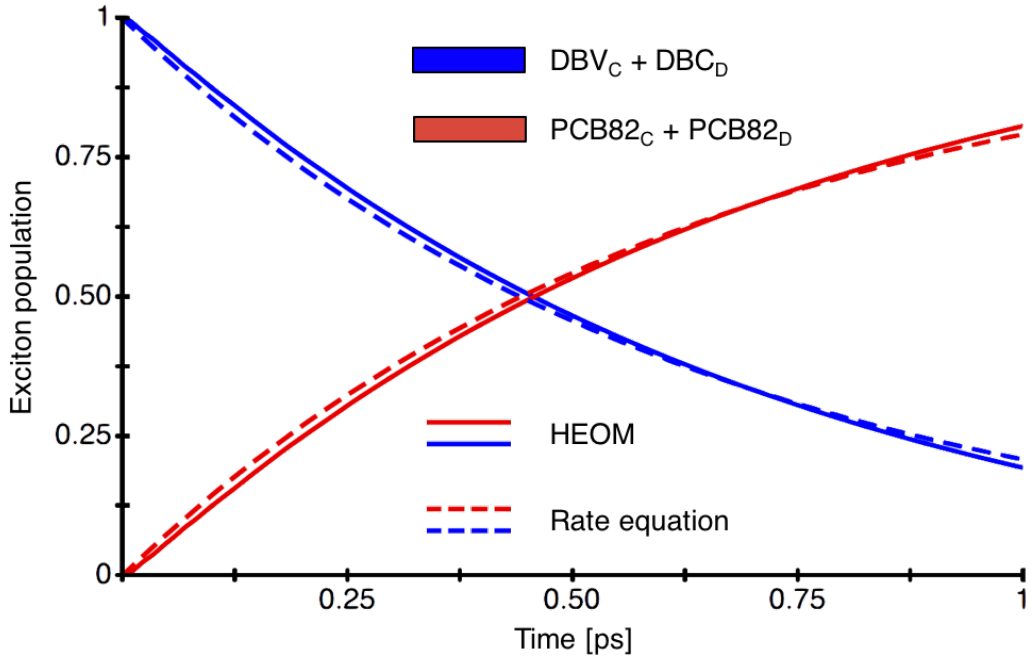

Figure 2.13: DBV to PCB82 populations: HEOM vs rate equation. Summed DBV populations (blue) and summed PCB82 populations (red) obtained from HEOM calculations (solid) are compared with the summed populations given by a rate equation (dashed) that employs the extracted rate of 1.6 ps^{-1}.

While rate calculations presented here were run at a hierarchy depth of Nmax=6, our four-site population dynamics no longer include the bilins with the largest reorganization energies, and thus we determined that they converged at a hierarchy depth of Nmax=5. The significantly reduced computational cost at this depth allowed us to use Class 1 spectral densities to simulate down-conversion rates presented in the main text while maintaining strict convergence. We note that the rate of down-conversion obtained from simulations with Class 1 spectral densities differs by less than 0.015 ps^{-1} compared with the rate obtained from simulations with Class 2 spectral densities.

Förster overlaps presented in the main text rely on the accuracy of Kubo fluorescence for the tightly bound DBV core. However, Kubo lineshapes fail to describe the time-dependent dynamic localization process captured by HEOM, as shown in Figure 2.15. The additional Stokes shift increases overlap with the PCB82 absorption by

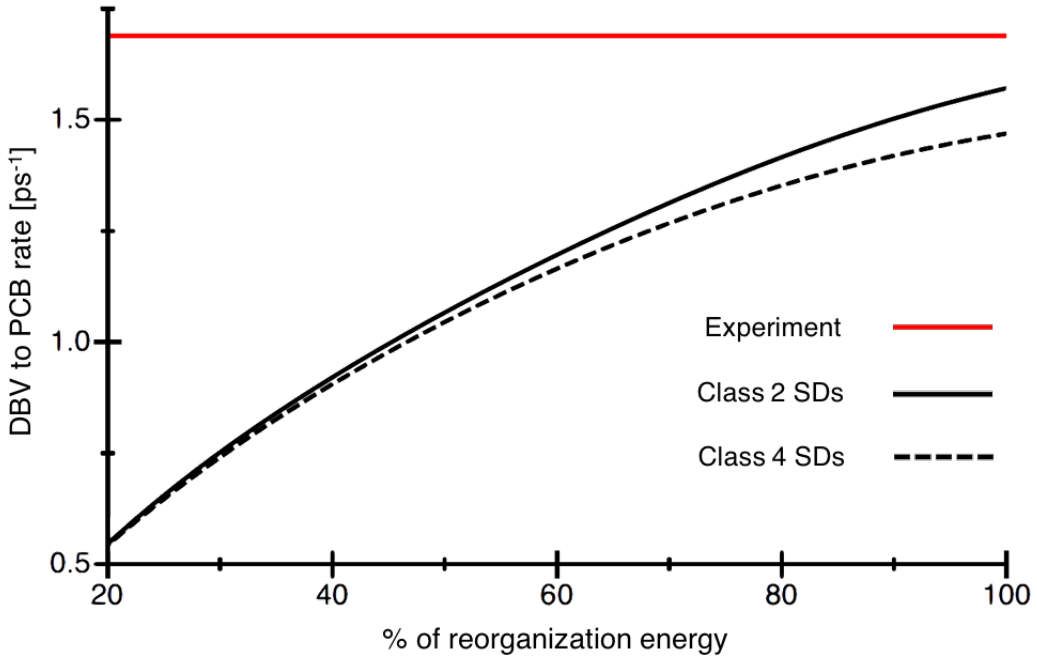

Figure 2.14: DBV to PCB transfer rate as a function of reorganization energy. EET rate as a function of reorganization energy scaling extracted from four-site HEOM calculations. The experimental rate is shown in red, HEOM simulations with Class 2 spectral densities (five peaks) are shown in solid black, and HEOM simulations with Class 4 spectral densities (two peaks) are shown in dashed black.

12%. The increased rate is mitigated by an estimated 10% decrease of $|V_{eff}^2|$ as a result of dynamic localization in the DBV core.

2.7.5 Model Vibronic Dimer

2.7.6 Coherent vs Incoherent Transport

Figure 2.4a depicts an energetically detuned dimer with a long-lived high-frequency vibration on the low-energy acceptor pigment that is resonant with the energy gap. As noted in the main text, we define the basis as a direct-product of three indices: the electronic state of the acceptor ($|g_a\rangle$, $|e_a\rangle$), the electronic state of the donor ($|g_d\rangle$, $|e_d\rangle$), and the vibrational state of the acceptor on either the ground- or excited-state harmonic oscillator of the acceptor ($|0_g\rangle$, $|0_e\rangle$, $|1_e\rangle$). In the purely coherent limit (i.e. $\lambda_{deph} \to 0$),

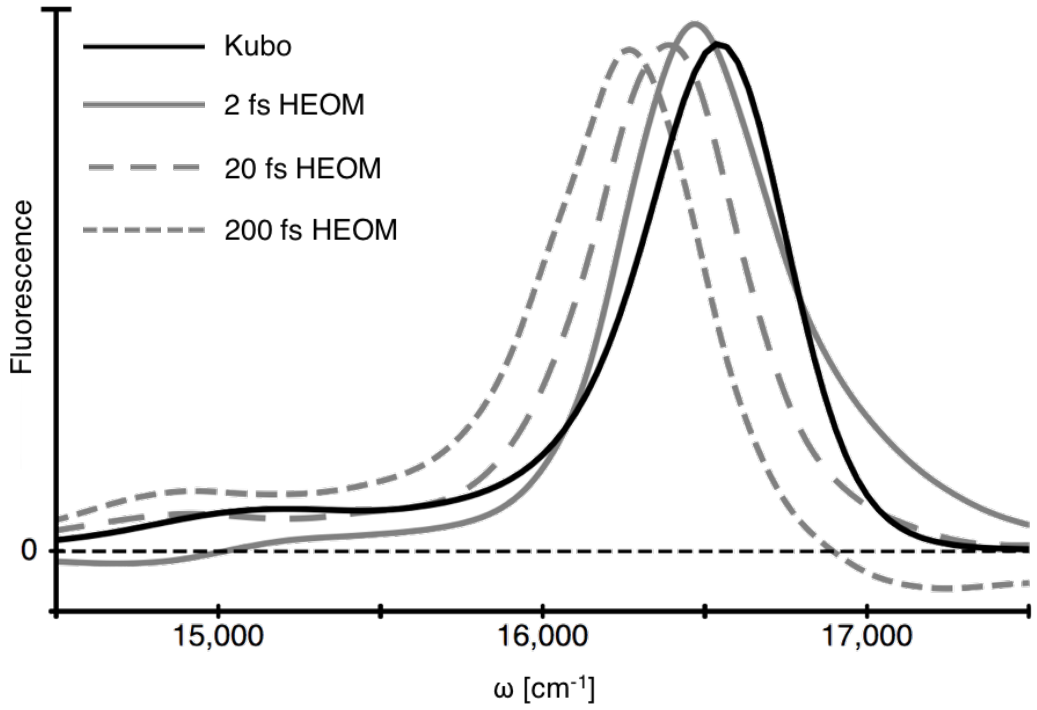

Figure 2.15: Time-dependence of HEOM DBV fluorescence compared to Kubo lineshape. Kubo fluorescence (black) fails to describe the dynamic localization captured by HEOM (gray) over 2 fs (solid), 20 fs (long dashed), and 200 fs (short dashed).

when the energy gap between the pigments is large compared to the electronic coupling (V) then we can ignore the presence of the low-energy (off-resonant) acceptor state and an excitation of the donor undergoes oscillatory transport with the vibrationally excited acceptor state (black dashed line, Figure 2.4c). The frequency of the oscillation is determined by the splitting of the eigenstates ($2 \cdot \mathrm{V}_{vib}$) of the vibronic block of the Hamiltonian (yellow area, Figure 2.4a). We define $\mathrm{T}_{coh} = \frac{\mathrm{h}}{4\mathrm{V}_{vib}}$ as the half period of the oscillatory motion, which determines the timescale of the initial rise for coherent dynamics. As λ_{deph} increases, the coherent rise is inhibited and dynamics moves into the incoherent regime. We can quantify the onset of incoherent dynamics by comparing HEOM (solid lines) and Förster (dashed lines) population dynamics when $\lambda_{deph} = 0.1\ \mathrm{V}_{vib}$ (green), $\lambda_{deph} = 1\ \mathrm{V}_{vib}$ (orange), and $\lambda_{deph} = 10\ \mathrm{V}_{vib}$ (red) (Figure 2.16). In the coherent regime, Förster over-estimates the rate of transport because it does not account for the

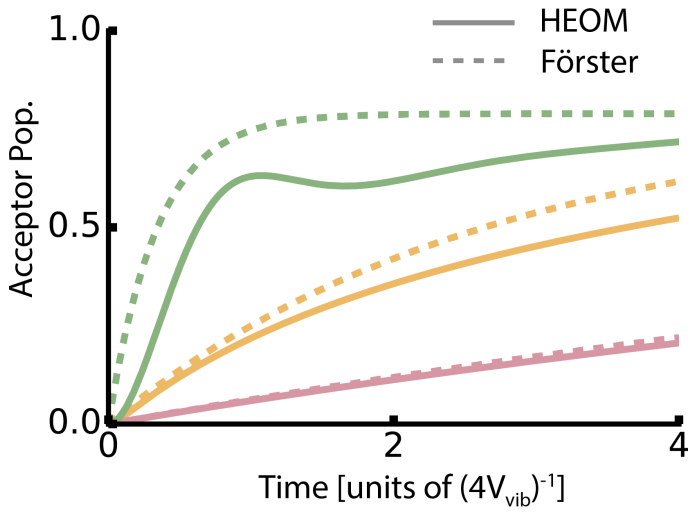

Figure 2.16: Comparing Förster and HEOM for different λ_{deph} values. We plot the acceptor population dynamics calculated using HEOM (solid lines) or Förster (dashed lines) when $\lambda_{deph} = 0.1, 1$, or 10 (green, orange, and red, respectively). The remaining simulations parameters are the same as described in the caption of Figure 2.4b.

possibility of coherent back-transfer between the nearly degenerate states (green lines, Figure 2.16). As λ_{deph} becomes equal to the vibronic coupling, the dynamics of Förster and HEOM become similar (orange lines, Figure 2.16). Finally, as λ_{deph} becomes larger than the vibronic coupling the excitation transport dynamics of Förster and HEOM become equivalent (red line, Figure 2.16).

2.7.7 Vibronic vs Electronic Transport

In the incoherent regime, where Förster theory captures the process of excitation hopping, the rate of transport is determined by the overlap of the donor fluorescence and the acceptor absorption. As a result, the reorganization energy of the vibrational environment plays two roles: first, the component of the reorganization process that occurs after optical dephasing results in a Stokes shift of the fluorescence peak of the donor compared to the absorption energy (E_d). Second, the reorganization energy controls the 'homogeneous' width of the donor fluorescence and acceptor absorption. When λ_{deph} is comparable to the energy gap between the donor (E_d) and acceptor ($E_a - \lambda_{vib}$) absorption energies, then the

0-0 transitions of the donor fluorescence and acceptor absorption can overlap, driving direct electronic transport without vibrational enhancement. However, when the donor-acceptor energy gap is large compared with λ_{deph}, transport requires the presence of a bridging high-frequency vibration that creates a vibronic side-band in the acceptor absorption, thereby increasing overlap. While the transition from coherent to incoherent is uniquely determined by the ratio of λ_{deph} to V_{vib}, the smallest λ_{deph} that supports direct electronic transport (i.e. not dependent on the high-frequency vibration) depends on the specific value of the energy gap. It is worth noting that in PC645, the energy gap between the DBV core and the PCB82s is large enough that electronic transport cannot explain direct down-conversion as seen by the DBV fluorescence and PCB82 absorption spectra presented if Figure 2.5e.

2.7.8 1 vs 2 vibrations

In the model dimer system, we have incorporated only a single vibration on the acceptor molecule. A single vibration on the donor molecule would result in identical dynamics, where the vibrationally excited state of interest is in the donor ground-state. In the case of two symmetric vibrations, one each on the donor and the acceptor, the Hilbert space must be extended by an additional index for the vibrational state of the donor pigment ($|e_a, g_d, 0_e^a, 0_g^d\rangle$, $|g_a, e_d, 0_g^a, 0_e^d\rangle$, $|e_a, g_d, 1_e^a, 0_g^d\rangle$, $|e_a, g_d, 0_e^a, 1_g^d\rangle$). The resulting Hamiltonian is given by,

$$\begin{bmatrix} \tilde{E}_a & V\langle 0_e|0_g\rangle & 0 & 0 \\ V\langle 0_e|0_g\rangle & E_d & V\langle 1_e|0_g\rangle & V\langle 0_e|1_g\rangle \\ 0 & V\langle 1_e|0_g\rangle & \tilde{E}_a + \hbar\Omega_{vib} & 0 \\ 0 & V\langle 0_e|1_g\rangle & 0 & \tilde{E}_a + \hbar\Omega_{vib} \end{bmatrix} \tag{2.8}$$

where $\tilde{\mathrm{E}}_a = E_a - \lambda_{vib}$. This four-state Hamiltonian can be compared to the 3-state equivalent given in Figure 2.4a. To see the influence of the second vibration on the transition from the coherent to incoherent regime, we will rewrite our basis set in terms of

a linear combination of the two degenerate vibrationally excited states:
$|e_a, g_d, \nu_+\rangle = \frac{1}{\sqrt{2}} \cdot (|e_a, g_d, 0_e^a, 1_g^d\rangle + |e_a, g_d, 1_e^a, 0_g^d\rangle)$,
$|e_a, g_d, \nu_-\rangle = \frac{1}{\sqrt{2}} \cdot (|e_a, g_d, 0_e^a, 1_g^d\rangle - |e_a, g_d, 1_e^a, 0_g^d\rangle)$. In this new basis, we find the Hamiltonian is given by

$$\begin{bmatrix} \tilde{E}_a & V\langle 0_e|0_g\rangle & 0 & 0 \\ V\langle 0_e|0_g\rangle & E_d & \sqrt{2}\cdot V\langle 1_e|0_g\rangle & 0 \\ 0 & \sqrt{2}\cdot V\langle 1_e|0_g\rangle & \tilde{E}_a + \hbar\Omega_{vib} & 0 \\ 0 & 0 & 0 & \tilde{E}_a + \hbar\Omega_{vib} \end{bmatrix} \tag{2.9}$$

where $\tilde{\mathrm{E}}_a = E_a - \lambda_{vib}$. The addition of a second equivalent vibration thus increases the effective vibronic coupling by a factor of $\sqrt{2}$ which slightly delays the transition from coherent to incoherent transport. Further, in the incoherent regime the presence of the second vibration results in a second pathway for excitation transport between the donor and acceptor (as seen by the presence of a vibronic peak in both the donor fluorescence and acceptor absorption) which increases the rate of transport by approximately a factor of 2 compared with the case of a single vibration.

2.7.9 Incoherent Vibronic Transport in PC645

While most of the electronic couplings in PC645 are weak enough (V $\ll$ 50 cm^{-1}) that a site-basis description is appropriate, the strong electronic coupling between the DBVs ($\sim$320 cm^{-1}) indicates that some exciton delocalization is present. While delocalization can increase coupling, we find that the exciton and site basis description of the DBV core both have at most 50 cm^{-1} of coupling to the PCB82s. In our *ab initio* QM/MM spectral densities, the DBVs and PCB82s have a long-lived ($\sim$200 fs lifetime), high-frequency ($\sim$1650 cm^{-1}) vibration with at most 96 cm^{-1} of reorganization energy which supports a 12 cm^{-1} vibronic coupling. The assignment of λ_{deph} for down-conversion in PC645 is complicated by both the presence of strong electronic coupling in the DBV core and the

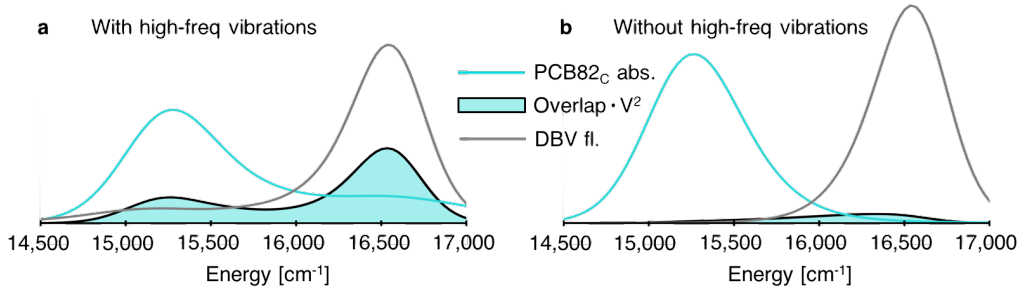

Figure 2.17: Overlap between DBV fluorescence and PCB82 absorption depends on vibronic side-bands. **a**, Kubo monomer absorption for PCB82$_C$ (cyan), Kubo DBV core fluorescence (gray), and absorption / fluorescence overlap weighted by the coupling to the lowest energy DBV exciton (outlined cyan) with high-frequency vibrations present. **b**, Kubo monomer absorption for PCB82$_C$ (cyan), Kubo DBV core fluorescence (gray), and absorption / fluorescence overlap weighted by the coupling to the lowest energy DBV exciton (outlined cyan) with high-frequency vibrations absent.

many timescales of vibrational relaxation evidenced by the structured form of the spectral densities. The $\sim$250 cm^{-1} shift in the fluorescence of the DBV core during the first 200 fs following excitation (Figure 2.15), however, is a lower bound for λ_{deph}. We thus find that the ratio of λ_{deph} to the vibronic coupling is at least 20, indicating the dominance of an incoherent transport mechanism.

To differentiate between vibronic and electronic transport, we examine the DBV fluorescence lineshape and PCB82 absorption spectra. The energy gap between the 0-0 transitions of the DBV fluorescence and the PCB82 absorption (i.e. transitions that do not change the vibrational quantum number of the donor or acceptor) is $\sim$ 1300 cm^{-1}. The FWHM of the 0-0 transitions are, however, only $\sim$ 500 cm^{-1}, resulting in minimal direct electronic transport between the DBVs and PCB82s. We verify this analysis by recalculating the fluorescence and absorption lineshapes in the absence of any high frequency vibrations (i.e. $\hbar\Omega_{vib} > 475$ cm^{-1}) while enforcing the original peak position as shown in Figure 2.17b. In keeping with the analysis above, we see minimal overlap between the 0-0 transitions in the absence of the high-frequency vibrations.

2.7.10 QM/MM Spectral Density Construction

Starting from the PC645 X-ray structure reported by Curmi et al.,[146] we constructed AMBER[147] molecular mechanics force fields for each bilin with Antechamber, part of AmberTools13.[147] We performed QM/MM nuclear dynamics using NWChem version 6.3[148] with a quantum mechanical treatment of a single bilin in each trajectory. We separated the quantum and classical regions of each calculation by inserting a fictitious hydrogen atom as a link into each bilin-protein bond.[149] Given the aqueous protein environment, we assumed that carboxylic acid groups were deprotonated, resulting in a net charge of -2 on each bilin. We added all bilin hydrogens by hand while allowing NWChem to automatically add hydrogens to the protein backbone assuming neutral pH. We obtained initial partial charges for bilin force fields from vacuum density functional theory calculations using the B3LYP exchange-correlation functional[150–152] and a 6-31G basis set. We solvated the protein using default directives in NWChem. Subsequently, we performed a geometry optimization on the quantum mechanically treated bilin in the presence of protein partial charges prior to running each trajectory. A geometry optimization consisted of ten cycles that each included 3000 MM optimization steps in which we held the QM region fixed followed by ten QM optimization steps in which we held the MM region fixed. Following the geometry optimization, we calculated new partial charges for each bilin in the presence of the protein environment and updated the underlying force field files. After the initial optimization, used to determine the bilin force field parameters, we performed ten additional optimization cycles such that final gradients were below thermal fluctuations. This yielded eight separate optimized structures, one for each bilin, from which to start our QM/MM trajectories.

We began each trajectory with 10 picoseconds of equilibration, during which the simulation temperature stabilized at 295K. We employed Berendsen's thermostat,[153] standard in NWChem, which is known to correctly approximate the canonical ensemble for simulations including thousands of atoms, such as an LHC.[154] After equilibration, we

performed 40 picosecond production runs. We used a 0.5 femtosecond time step for both equilibration and production runs. Overall, the eight 50 picosecond QM/MM trajectories took nearly nine months to run, and cost over two million CPU hours.

To construct energy gap trajectories for each bilin, we extracted geometries at two femtosecond intervals, for a total of 20,000 geometries per bilin. We ran time dependent density functional theory (TDDFT) calculations using the B3LYP functional and 6-31G basis set on the resulting 160,000 geometries on both Harvard's Odyssey cluster and the Edison supercomputer at the Department of Energy NERSC facility, using a combined four million CPU hours. We note that while TDDFT often incorrectly predicts excitation energies, cancellation of error results in good descriptions of the curvature of the potential energy surface that we depend on here.[123,124] For each geometry, we calculated the first five excited states and selected the brightest state, defined as the one with the largest oscillator strength. For a small fraction of calculations (<1%) where two states were within 0.05 oscillator strength, we used their transition dipole vectors to find a linear combination of the two states with maximized oscillator strength. Separately, roughly 5% of the TDDFT calculations failed to converge, requiring us to re-run these calculations with the larger 6-31G* basis set. To make sure that mixing results from two different basis sets did not introduce numerical issues, we additionally ran 6-31G* TDDFT for all geometries of a single bilin. We found the resulting energy gap correlation function to be nearly identical to that constructed with the mixed 6-31G and 6-31G* results.

Following Ref.,[47] we constructed two-time bath correlation functions from the energy gap trajectories. To ensure that the correlation functions decayed to zero after roughly two picoseconds, we convolved the resulting correlation functions with a Gaussian having a standard deviation of 24 femtoseconds, as per Ref.[115] We Fourier transformed the resulting correlation functions to obtain a spectral density for each bilin. Drude-Lorentz peaks were then fit to each spectral density to allow for their application to exciton dynamics with the hierarchical equations of motion (HEOM) approach.[12,13]

Initial State	Flux to MBV_A	Flux to MBV_B	Flux to $PCB82_C$	Flux to $PCB82_D$
DBV_D	0.1858	0.2069	0.2719	0.2315
$DBV + exciton$	0.1824	0.2127	0.2772	0.2294
$DBV + site$	0.1815	0.2116	0.2760	0.2286
$DBV - exciton$	0.1807	0.2104	0.2747	0.2278
$DBV - site$	0.1816	0.2115	0.2759	0.2286

Table 2.7: Flux out of the DBV core with different initial states.

2.7.11 EET Pathways are Insensitive to Initial Density Matrix

There has been extensive discussion in the literature regarding the importance of coherent versus incoherent excitation for natural photosynthesis.[155–157] In our assessment of PC645 flux, we have assumed an initial excitation of the DBV_D bilin, but laser excitation interacts with eigenstates of the dipole operator which can delocalize across multiple bilins. In order to assess the importance of our choice of a DBV_D excitation, we calculate exciton flux out of the DBV core with a range of initial conditions (Table 2.7) including the high-energy DBV core eigenstate (DBV+ exciton), the low-energy DBV core eigenstate (DBV- exciton), and the equivalent population distributions with the off-diagonal entries of the density matrix set to zero (DVB+ site and DVB- site). In order for the excitation condition to be important, the transport of interest must occur on timescales fast enough that the initial conditions remain imprinted in the density matrix. Consistent with our assignment of incoherent transport, all memory of the initial coherence of the excitation is lost prior to transport resulting in identical ($\pm$ 0.001) fluxes for the exciton and site excitations with matched initial populations (e.g. DBV+ exciton and DBV+ site). Further, the rapid relaxation of excitation within the DBV core compared to transport out of the core results in excitations reaching local equilibrium prior to transport. Thus we also find very close agreement ($\pm$ 0.01) between the flux distributions for all five initial conditions.

2.7.12 The Regime of Transport is Robust to Modest Changes in DBV - PCB Couplings

In the main text, we have assigned incoherent vibronic transport by (i) noting that there is a lower bound on the quickly relaxing component of the reorganization energy that is 20x larger than the vibronic coupling, and (ii) demonstrating the absence of a resonance condition consistent with a coherent enhancement of the transport rates. Specific assignment of coupling elements between pigments can be complicated by the heterogeneous dielectric environment of the protein. We test the sensitivity of our assignment of an incoherent vibronic transport mechanism to modest perturbations in the coupling elements between the DBV and PCB82 pigments. We simulate four-site population dynamics, and plot the sum of the PCB82s, when DBV - PCB82 couplings have been decreased (Figure 2.18a) or increased (Figure 2.18b) by a factor of 1.5 for all four conditions used in the main text Figure 2.5b. These calculations demonstrate the continued absence of a sharp resonance condition or even sensitivity to the presence of the high frequency vibration. Further, the rate of transport increases (decreases) by a factor of 2.1-2.3 when the coupling is increased (decreased) which is consistent with the prediction of 2.25 from Förster theory.

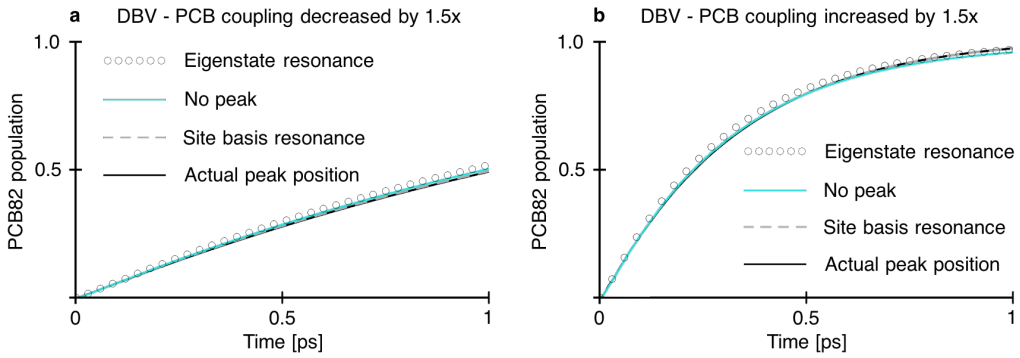

Figure 2.18: Resonance condition remains absent at increased or decreased couplings. a Population dynamics of a four-site system containing DBVs and PCB82s where DBV - PCB82 couplings have been decreased by a factor of 1.5. **b** Population dynamics of a four-site system containing DBVs and PCB82s where DBV - PCB82 couplings have been increased by a factor of 1.5.

3

Ab Initio Simulations of a Synthetic Fluorescein Dimer Reveal Electronic Coherence

3.1 Abstract

Investigating the importance of electronic coherence in biological light-harvesting has driven research in the last decade based on the promise of novel bio-inspired technologies. However, disentangling the excitation dynamics of pigment-protein complexes has necessitated the use of sophisticated spectroscopic techniques that remain difficult to analyze. The need for a simple model system prompted Hayes et al. to synthesis a series of fluorescein dimers that exhibited off-diagonal oscillations in 2D spectra which they interpreted as evidence of electronic coherence. Despite the reduced complexity, both underlying system properties and the coherent assignment were immediately contested. We seek to resolve this controversy by simulating the excitation dynamics of a synthetic fluorescein dimer with high accuracy and from first principles. We find electronic coupling to be an order of magnitude larger than previously thought, and that strong coupling is critical to obtaining excellent agreement between simulated and experimental linear spectra. We observe strong oscillations at the frequency of electronic coherence for the first 100-150 femtoseconds of population and coherence dynamics, after which long-lived

vibrationally driven coherences persist for hundreds of femtoseconds. Thus we have identified strong electronic coupling in a fluorescein dimer and confirmed that electronic coherence can be engineered in artifical systems.

3.2 Introduction

Delocalized excited states can allow for coherent, wave-like excitation energy transport (EET), potentially yielding superior transfer efficiencies than incoherent hopping mechanisms.[101,106,158] The observation of persistent off-diagonal beatings in 2D spectra of biological light-harvesting systems led to the hypothesis that long-lived electronic coherences play a functional role in photosynthetic EET.[5,159] However, the complexity of both the pigment-protein complexes and the spectroscopic techniques makes it difficult to distinguish between electronic coherence, vibronic (mixed electronic and vibrational) coherence,[9,141,160] and ground-state vibrations, convoluting mechanistic assignment and precipitating a decade of fierce debate over the importance of coherent effects in biology.[5,7,9,11,26,101,103,106,107,109,115,121,130,132,134,136,140,146,155,158,159,161,162] In 2013, Hayes et al. engineered rigid synthetic fluorescein heterodimers that exhibited long-lived 2D off-diagonal oscillations with the goal of providing a model system for investigating coherent energy transfer in multichromophoric systems.[15] Despite the system's reduced complexity, the work attracted almost immediate controversy.[163] Here, we seek to verify the coherent timescale and assignment by simulating transfer dynamics, coherences, and 2D spectra of a fluorescein heterodimer with high accuracy and entirely from first principles. We find that the dimer exhibits strong electronic coupling and that electronic coherence persists for 100-150 fs.

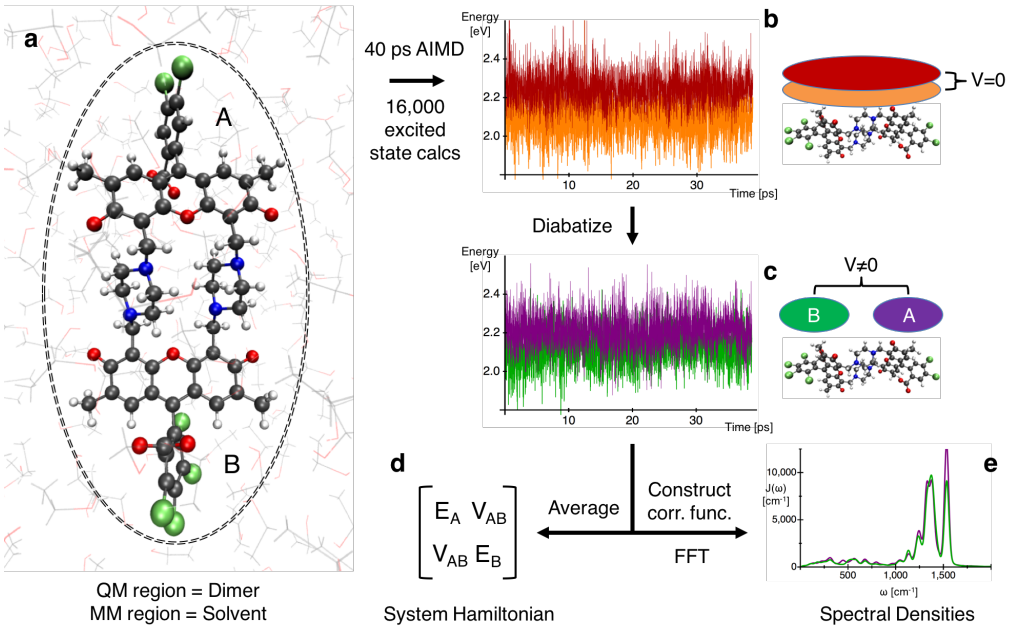

Figure 3.1: Computational methodology for Hamiltonian and spectral density construction. **a**, Molecular structure of the AB dimer. Gradients for the 40 ps nuclear dynamics trajectory are obtained from a classical forcefield for the ethanol solvent and from planewave density functional theory for the dimer itself. **b**, First two delocalized, adiabatic excitation energy gap trajectories extracted from 16,000 SOS-CIS(D) calculations. The lowest energy excited state is shown in orange, the 2nd lowest energy excited state is shown in red, and by definition these states are orthogonal and thus have no electronic coupling. **c**, Localized, diabatic energy gap trajectories obtained following a fragment excitation difference diabatization on the adiabatic trajectories. The excitation localized on the A dye is shown in purple while the excitation localized on the B dye is shown in green, and their electronic coupling is now non-zero. **d**, Averaging our diabatic energy gap trajectories as well as the trajectory of their electronic coupling yields the site energies and the coupling, respectively, which form our system Hamiltonian. **e**, We can instead construct energy gap correlation functions and Fourier transform to obtain our two site spectral densities.

3.3 Results and Discussion

3.3.1 Hamiltonian and Spectral Density Construction

Excitation dynamics simulations require three main components: the system Hamiltonian, which defines the excited state energies and their electronic coupling, spectral densities, which define the frequency-dependent coupling of a given excited state to its thermal environment,[120] and excited state transition dipoles. These components can be extracted by simulating a nuclear dynamics trajectory and performing thousands of

excited state calculations on geometry snapshots at regular intervals.[115–118,121] Given the detail we are aiming to resolve, we went beyond the field's standard nuclear dynamics procedure of classical MD and instead propagate nuclear dynamics trajectories with mixed quantum/classical planewave density functional theory *ab initio* molecular dynamics (QM/MM PWDFT AIMD), where we obtain dimer forces quantum mechanically and solvent forces from a classical forcefield (Figure 3.1a). We note that this is just the second time that AIMD has been used for spectral density construction, with our previous work on PC645 being the first.[162]

We then calculate the first two excited states of the dimer every 2.5 femtoseconds using configuration interaction singles (CIS)[164] and spin opposite-scaled configuration interaction singles with perturbative doubles (SOS-CIS(D)).[165] However, these calculations yield delocalized, adiabatic states that are orthogonal, and thus by definition have no electronic coupling (Figure 3.1b). In order to examine coherence between the two fluoresceins, we instead require localized, diabatic states with finite electronic coupling. Thus, we employ the fragment excitation difference (FED) diabatization[166] to rotate our states into a diabatic basis (Figure 3.1c), yielding energy gap trajectories for excitations on the A and B dyes as well as a trajectory of their electronic coupling. Averaging our trajectories yields the system Hamiltonian (Figure 3.1d), the values of which are summarized in the first four rows of Table 3.1. We can also construct energy gap correlation functions for our two diabatic trajectories as per Valleau et al.[47] and Fourier transform to obtain spectral densities for each site (Figure 3.1e), the reorganization energies of which are reported in the last two rows of Table 3.1. Please see the methods section for comprehensive details on all the calculations summarized here.

As we expect, SOS-CIS(D) excitation energies are significanly closer to the experimental approximation of the A and B site energies than CIS excitation energies (Table 3.1). Further, the SOS-CIS(D) energy gap between A and B is in reasonable agreement with experiment, and far closer than the CIS energy gap. However, while our SOS-CIS(D)

	CIS	SOS-CIS(D)	Exp. Approx.
$E_A[eV]$	3.555 ± 0.00054	2.210 ± 0.00084	2.37
$E_B[eV]$	3.450 ± 0.00059	2.137 ± 0.00092	2.30
$\Delta E_{AB}[cm^{-1}]$	850.7 ± 9.1	593.3 ± 14.2	500
$V_{AB}[cm^{-1}]$	448.1 ± 0.2	346.3 ± 1.37	< 30
$\lambda_A[cm^{-1}]$	820.4	1062.8	——
$\lambda_B[cm^{-1}]$	697.1	966.9	——

Table 3.1: Comparing CIS, SOS-CIS(D), and experimental absolute energies, energy gaps, couplings, and reorganization energies. Standard error is shown where applicable.

coupling value of 346.3 cm^{-1} is substantially smaller than our CIS coupling, it is over an order of magnitude larger than the coupling assumed by experimentalists.[167] We will discuss the problems with the weak coupling assumption in great detail after we examine our spectral densities and simulated linear spectra. Finally, we note that all simulations shown throughout the manuscript use the SOS-CIS(D) Hamiltonian given its consistency with experiment and that it is based on a higher level of theory.

3.3.2 Spectral Densities and Linear Spectra

We aim to simulate exciton dynamics and spectroscopy with QMaster,[14] a high-performance implementation of the numerically exact hierarchical equations of motion (HEOM) method.[12,13] However, HEOM scales factorially with the number of bath modes present in the simulation, necessitating substantial coarse graining of our spectral densities. We parameterize four classes of pairs of spectral densities that include in total 34 (Class 1), 19 (Class 2), and 8 peaks (Class 3) respectively. Peak parameters and details of the coarse graining procedure are given in supplementary information section 3.7.2. While Class 1 spectral densities contain far too many peaks to use in HEOM, exact Kubo monomer lineshapes allow us to compare all three classes of spectral densities. We find almost no difference between the resulting monomer lineshapes (Figure 3.4), giving us confidence in our coarse graining.

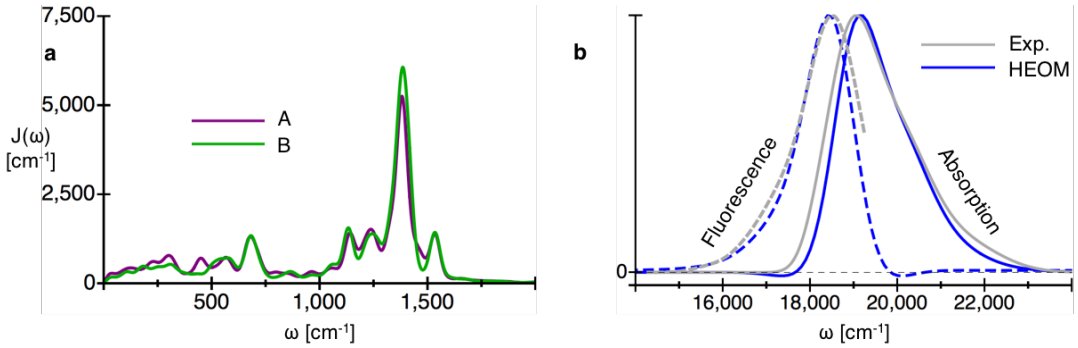

Figure 3.2: Spectral densities and linear spectra. a, CIS spectral densities for the A dye (purple) and for the B dye (green). **b**, A comparison of simulated (blue) and experimental (gray) linear spectral, where absorption is shown with solid lines and fluorescence is shown with dashed lines. Simulated spectra include 400 cm^{-1} of inhomogeneous broadening, a 2300 cm^{-1} constant shift, and a 35 degree rotation of one transition dipole vector, but are otherwise entirely *ab initio*.

Spectroscopic signals and coherence dynamics depend intimately on the system Hamiltonian and site spectral densites; therefore, we seek to validate our Hamiltonian and spectral densities by comparing simulated linear spectra to experimental linear spectra. Preliminary HEOM simulations of linear absorption and fluorescence using Class 2 spectral densities yield excellent agreement with experimental Stokes shift and peak positions while also revealing the need for better transition dipole moments and the importance of inhomogeneous broadening (Figure 4.18). Since SOS-CIS(D) is only an energy correction,[165] our average transition dipoles are directly from CIS, which is known to struggle in particular with this property.[168] Therefore, our need to slightly rotate the A transition dipole vector by 35 degrees in order to correct the relative absorption peak heights is unsurprising. Once we apply 400 cm^{-1} of inhomogeneous broadening, as described in the methods section, we obtain the spectra shown in Figure 3.2b (CIS) and Figure 3.6 (SOS-CIS(D)). We note that the transition dipole rotation, the choice of inhomogeneous broadening, and the standard addition of a constant shift to match experimental spectral positions are the only aspects of our analysis that do not come entirely from first principles.

While linear spectra simulated with both CIS and SOS-CIS(D) spectral densities are in

good agreement with experiment, CIS spectral densities do a better job capturing the Stokes shift and thus we employ them exclusively going forward. The erroneously large reorganization energies of the SOS-CIS(D) spectral densities may originate from the mismatch with the underlying CIS diabatization. A thorough comparison of CIS and SOS-CIS(D) spectral densities and linear spectra is presented in supplementary information section 3.7.5.

3.3.3 The Case for Strong Coupling

Having validated our Hamiltonian, we now examine the order of magnitude mismatch between the electronic coupling extracted from our calculations and that assumed by experimentalists. While exciton energies can be quantified with linear absorption, site energies and electronic couplings explicitly depend on the underlying diabatization, and thus are most often obtained theoretically.[169] However, accurate simulations of couplings require a trajectory of geometries and thus entail substantial real and computational time.

In their original paper, Hayes et al. assert that their dimers have weak electronic coupling based on the fact that monomer linear spectra approximately sum to dimer linear spectra (Figure 3.7) and that exciton peaks remain unresolved even at cryogenic temperatures.[15] Crucially, this assumption allows them to assign the frequency of electronic coherence without calculating site couplings explicitly. Given their evidence, the lack of contradictory simulations, and the resources required to simulate coupling, this was a reasonable course of action at the time. When Halpin et al. question the weak coupling assumption in their comment,[163] Hayes et al. further support their argument by citing the simulations of Akimov and Prezhdo[170] and presenting a four-gaussian fit to low-temperature AB absorption.[167] However, the simulations of Prezhdo are unreliable given that they employ semiempirical extended Huckel theory and have incorrectly protonated alcohol and carboxylic acid groups despite the experiment's basic solvent.[15] Furthermore, the molecular orbitals shown in Prezhdo's Figure 3.3 and cited by Hayes

were calculated in vacuum,[170] a suspect approximation given that excited states can change substantially in the presence of an electrostatic environment.[171–173] We also remain unconvinced by the four-gaussian fit to 77K absorption given that accurate extraction of site energies requires simultaneously cross-referencing many different experimental observables.[106,114,133]

Therefore, the strong couplings extracted from our calculations, performed at great cost and at the limit of computational feasibility, represent an important new piece of evidence in this debate. The agreement between our simulated AB dimer linear spectra and experimental spectra is superior to the agreement between experimental summed monomer spectra and dimer spectra (Figure 3.2 and Figure 3.7) and further solidifies the assignment of strong coupling. Additionally, if we reduce our coupling by a factor of ten to roughly agree with the speculative coupling of 30 cm^{-1}, simulated Stokes shift and lineshape cannot be made to agree or even approach experimental values, as described in supplementary information section 3.7.4 and shown in Figure 3.8. As we proceed to examine the presence of coherence in the AB dimer, we note that our assignment of strong coupling means that the frequency corresponding to electronic coherence is actually the eigenenergy difference of 915 cm^{-1} and not the site energy difference of 500 cm^{-1} examined by Hayes et al.

3.3.4 Population and Coherence Dynamics

While experimentalists are limited to measuring transport and coherence with indirect techniques such as transient absorption and 2D echo spectroscopy, we can directly simulate population and coherence dynamics by propagating a density matrix with a diagonal or off-diagonal initial state, respectively.

Population dynamics calculated with HEOM and Class 2 spectral densities exhibit an early-time coherent rise at the Eigenenergy difference of 915 cm^{-1} that identifies electronic coherence (Figure 3.3a, dashed blue). While oscillations of this frequency

strongly presist only 100 fs, almost 90% of the excitation transfer is completed during this time. Population oscillations dynamically change over time and can be examined more thoroughly to probe the nature of the coherences relevant to transport; however, a better measure can be obtained by propagating the coherence directly.

Exciton coherences reveal short-time electronic coherence which transitions to vibrationally driven coherence after 150 fs. Coherent dynamics (Figure 3.3b) can be disentangled by performing a windowed fast Fourier transform as per Kriesbeck et al.[174] (Figure 3.3c), snapshots of which reveal the nature of the coherence as a function of time. At early times (50 fs), the frequency of electronic coherence can be seen to dominate the power spectrum (Figure 3.3d). However, it remains the dominant feature for only 100 fs. By 150 fs, the magnitude of the electronic frequency has decayed substantially, and by 200 fs it only minorly contributes to the power spectrum, which exhibits particularly strong features at vibrational frequencies 680 cm^{-1} and 1350 cm^{-1} (Figure 3.3e). Our observation of electronic coherence lasting between 100 and 150 fs is in excellent agreement with experimentally observed dephasing times. Finally, by 350 fs, long-lived vibrations at 450 cm^{-1}, 550 cm^{-1}, 680 cm^{-1}, 1200 cm^{-1}, and 1550 cm^{-1} dominate the power spectrum (Figure 3.3g).

We note that long-lived coherent frequencies precisely match the sharpest peaks present in our Class 2 spectral densities. While other observables change very slightly (population dynamics) or remain essentially unchanged (linear spectra) by moving from Class 2 to Class 3 spectral densities, long-time coherence dynamics change substantially, as shown in Figure 3.11, 3.12, 3.13, and 3.14. The observation of a coherence between two electronic excited states oscillating at vibrational frequencies could lead one to assign such oscillations to vibronic coherence. However, vibronic effects imply mixing between electronic and vibrational states and thus must exhibit shifts away from pure vibrational frequencies.[8] Given that we observe no such shifts, we cannot assign the oscillations to vibronic coherence. To probe the underlying mechanism, we construct a model vibronic

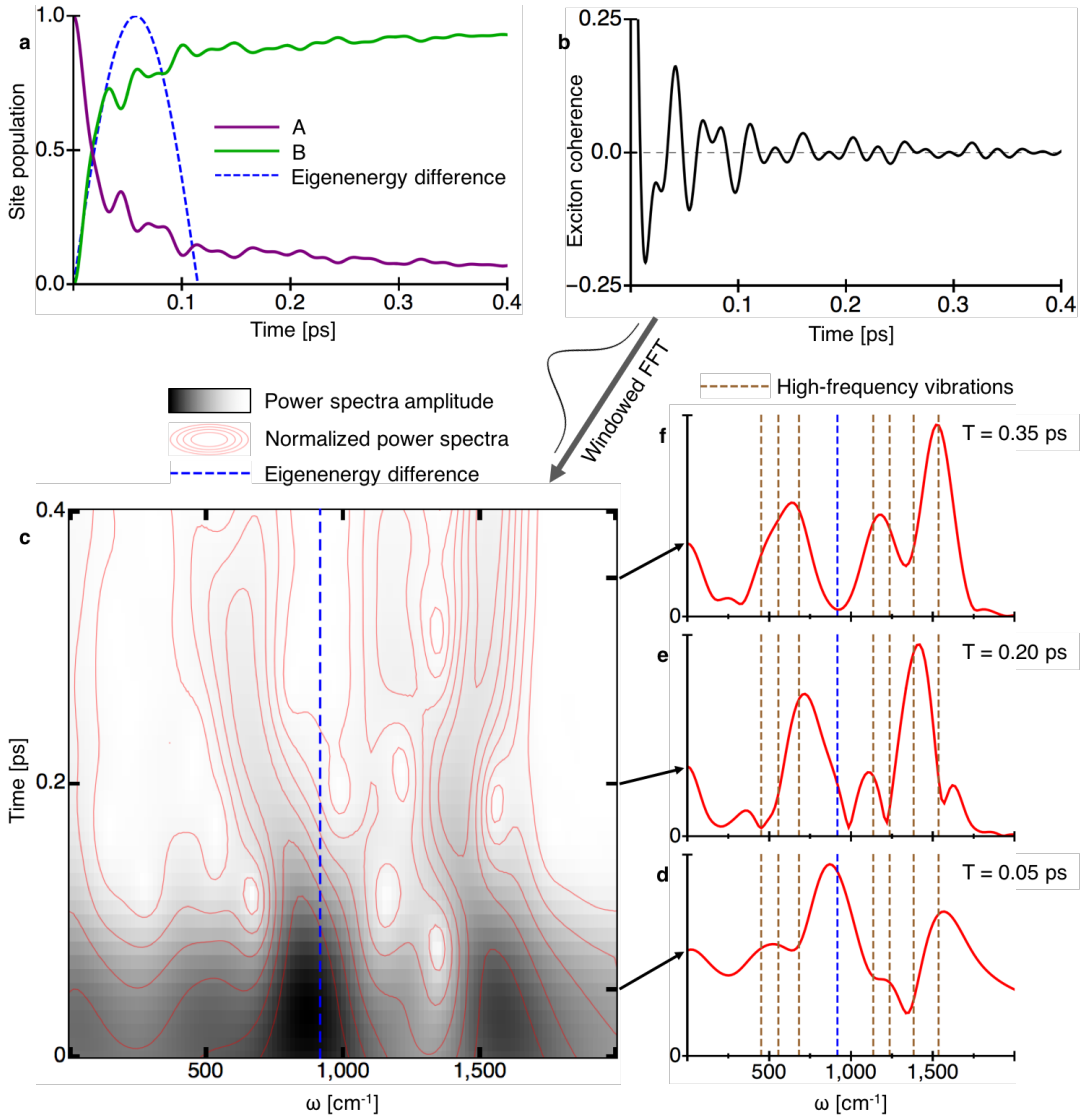

Figure 3.3: Population and coherence dynamics. **a**, Transport dynamics simulated with HEOM and Class 2 spectral densities with the excitation initially locaized on the high-energy A dye (purple) and rapidly migrating to the B dye (green) with an initial rise corresponding precisely to the frequency of electronic coherence (dashed blue). **b**, Direct propagation of exciton coherences. **c**, Windowed Fourier transform of the coherence dynamics, where a grey scale denotes absolute power spectra amplitude, red contour lines denote normalized power spectra amplitude to better reveal long-time vibrational effects, and the frequency of electronic coherence is shown in dashed blue. Note that the dark feature in the bottom middle of the panel denotes electronic coherence. **d**, Windowed FFT time slice at 0.05 ps, where strong high-frequency vibrations from both A and B spectral densities are shown in dashed brown. **e**, Windowed FFT time slice at 0.2 ps. **f**, Windowed FFT time slice at 0.35 ps.

Hamiltonian with Van Vleck perturbation theory, as described in supplementary information section 3.7.7. We find that while long-lived coherent oscillations arrise due to vibronic mixing, they are of almost entirely vibrational character, and thus we describe them as vibrationally driven coherence.

3.3.5 2D Spectroscopy

In an effort to compare directly with experiment, we simulate a picosecond trajectory of 2D spectra with five fs resolution. However, 2D HEOM simulations are significantly more computationally intensive than any of the previously reported calculations and also require an additional level of the hierarchy to converge (Nmax=7). Thus, we are limited to Class 3 spectral densities, and the trajectory still takes two weeks on a 256 GPU cluster. Unfortunately, simplification to Class 3 spectral densities prevents accurate incorporation of vibrational frequencies and lifetimes, substantially diminishing the quality of our results and preventing a quantitative comparison with experiment.

Despite the limitations of our 2D simulations, we do observe a 915 cm^{-1} feature in the short-time power spectra of the off-diagonal oscillations of both the stimulated emission (SE) and excited state absorption (ESA) pathways, consistent with our assignment of electronic coherence (Figure 3.18, 3.19). However, the 915 cm^{-1} features in SE and ESA in large part cancel out when all pathways are summed together (Figure 3.17). Cancelation is exacerbated by overly broad features that arise from the broad peaks in our Class 3 spectral densities. Thus, we expect that more accurate spectral densities including realistic, narrow peaks would allow at least a small peak at 915 cm^{-1} to remain in the total off-diagonal oscillation power spectrum. Unfortunately, 2D calculations with more complex spectral densities are computationally infeasible.

Re-examining experimental off-diagonal oscillation power spectra reveals that a 915 cm^{-1} peak present for the AB dimer is absent for the mixture of A and B monomers (Figure 3.21). Comparing dimer and monomer mixture power spectra is the key piece of

evidence that Hayes et al. use to finalize their assignment of electronic coherence.[15] However, the dimer spectra peak at 500 cm^{-1} that they assign to electronic coherence could instead be the 470 cm^{-1} peak observed in the monomer mixture shifted 30 cm^{-1} due to vibrational perturbations from molecular linkage. Furthermore, our dimer spectral densities contain multiple long-lived vibrations near 500 cm^{-1} that could explain that particular peak while no such vibrations exist near 915 cm^{-1}. Therefore, we find the presence of the 915 cm^{-1} feature in the dimer power spectra and the absence of such a peak in the monomer mixture power spectra is consistent with our assignment of the electronic coherent frequency and thus the presence of strong electronic coupling.

3.4 Conclusion

We sought to clarify the nature and timescale of the controvertial coherence in a synthetic fluorescein dimer. We characterized the system Hamiltonian and spectral densities with high accuracy and from first principles using QM/MM PWDFT AIMD and thousands of SOS-CIS(D) excited state calculations. We found electronic coupling to be an order of magnitude larger than previously thought, changing the frequency corresponding to electronic coherence from 500 cm^{-1} to 915 cm^{-1}, and that strong coupling was critical to our observed excellent agreement between simulated and experimental Stokes shift and lineshape. We calulated population and coherence dynamics and found that signatures of electronic coherence persist for 100-150 fs, after which complex vibrationally driven coherences dominate. We simulated a trajectory of 2D spectra and found signatures of electronic coherence in the SE and ESA pathways that mostly cancelled out in the summed signal. Finally, we examined the experimental 2D power spectrum and found that a small peak at 915 cm^{-1} is present for the dimer and absent for the mixute of monomers, confirming strong electronic coupling in the fluorescein dimer and that electronic coherence can be engineered in artifical systems.

Our work demonstrates the importance of leveraging both theory and experiment when

investigating coherence while simultaneously highlighting critical areas of improvement for each. Although simulations allowed us to probe observables that are not directly experimentally accessible, such as population and coherence dynamics, accurate characterization of the underlying Hamiltonian and spectral densities took over a year of combined real and computational time. More efficient strategies for system characterization, such as the one pioneered by Coker,[122] must continue to be developed and improved along with more efficient exciton dynamics methods that retain much of the accuracy of HEOM. In concert, these advances would make larger and more important systems, such as the photosynthetic reaction center,[9,10,106] computationally tractable and would also allow smaller systems to be treated en masse in screening applications. Regarding experiment, we propose that 2D echo spectroscopy alone is not an optimal strategy for investigating coherence given multiple observations[2,174,175] like ours that SE and ESA cancelation can mask the feature of interest. 2D fluorescence spectroscopy,[175,176] which explicitly prevents this cancelation, or full quantum process tomography[177,178] could be used to supplement 2D echo and yield a more reliable description of the underlying excitation dynamics.

3.5 Methods

We prepared the AB dimer structure in Avogadro[179] with all OH groups deprotonated and thus a net -4 charge, given the use of basic solvent,[15] and preformed initial optimization in vacuum with the universal forcefield (UFF).[180] We then solvated the structure in a box of 240 ethanol molecules with Antechamber, a part of AmberTools13,[147] and performed a brief additional optimization of both the dimer and solvent with the UFF. We then treated the solvated structure with the QM/MM interface of the pseudopotential plane-wave density functional theory module of NWChem[148] on the Cori supercomputer at NERSC. We chose the unit cell size of 48 by 70 by 48 bohr to prevent dimer self-interaction despite the use of periodic boundary conditions, and the

PBE96 exchange-correlation functional[181] given it's excellent tradeoff between accuracy and computational cost. We treated ethanol solvent molecules with the OPLSAA forcefield[182,183] as well as local pseudopotentials with partial charges as per ref.[184] We collected additional parameters necessary for Lennart Jones ionic interactions from appropriate sources when not available in original OPLSAA.[185–188]

We then fixed dimer coordinates and optimized solvent molecules with 100 steps of steepest descent in the presence of an approximate AB dimer electron density converged with a minimal wavevector cutoff of 2 Hartree. We then propagated the entire system for 30,000 steps with the Car-Parinello algorithm[189] using a time step of 5 atomic units, a fake mass of 600 atomic units, and a Nose Hoover chain thermostat[190] at 295 Kelvin in order to equilibrate the solvent temperature. We then raised the wavevector cutoff to 35 Hatree and released dimer coordinates, propagating the entire system to equilibation for 10 ps, at which point the system temperature had stabilized at 295 K. We then performed a production run of 38 ps of QM/MM AIMD, still employing our previous time step of 5 atomic units, parallelized over 960 cores. We split the production AIMD trajectory into tasks of 3000 time steps, each of which printed restart files upon completion, in order to gracefully address inevitable crashes or maintenance. Note that a system of this size and complexity was a unique challenge for NWChem, and we worked directly with the developer of the NWPW module, Eric Bylaska, for months in order to correctly prepare the calculation. Additionally, Dr. Bylaska had to implement a new fast error function in order to allow our trajectory to complete in a timely manner. After six months preparing the calculation, AIMD took over four months of real time and cost just over two million CPU hours.

With our trajectory of geometries in hand, we then prepared SOS-CIS(D) excited state calculations[165] followed by an FED diabatization[166] in Q-Chem.[191] We employed a 6-31G basis and an rimp2-VDZ auxilliary basis,[192,193] as required by the SOS-CIS(D) method in Q-Chem. We specified donor and acceptor atomic indices for the diabatization,

incorporated solvent molecules as point charges, and solved for the first two adiabatic excited states, which were then rotated to yield localized diabatic states and an electronic coupling value. We did over 100 spot-checks solving for three excited states over the course of the trajectory and found the 3rd excited state to always be substantially higher in energy and substantially lower in oscillator strength than the first two, giving us confidence in our two-state treatment. We took particular care to identify which site each diabatic state sits on given that their ordering changed frequently over the course of the trajectory. While an individual SOS-CIS(D) + FED calculation was straightforward to perform, scalling up to 16,000 calculations presented new challenges due to the 50 GB of scratch that each single point calculation wrote to scratch combined with their 12 hour runtime. NERSC consultants helped us to identify the optimal batch configuration of 64 single core jobs and to compile a custom Q-Chem executable that prevented their substantial IO from interfering with eachother. In total, SOS-CIS(D) + FED excited state calculations took two months and cost 400,000 CPU hours.

We performed exciton dynamics simulations with the QMaster software package[14] that provides a high-performance implementation of HEOM and runs flexibly on both GPU and CPU architectures.[14,108,144] HEOM fluorescence calculations used a development version of QMaster. All HEOM results presented were run at a hierarchy depth of six except for 2D simulations, which were run at a hierarchy depth of seven, and fluorescence simulations, which were run at a hierarchy depth of eight. All HEOM results employed a time step of 0.5 fs to ensure accurate propagation. Inhomogeneous broadening was applied to linear spectra through Gaussian weighting of both the dimer energy gap and the energy midpoint.

3.6 Acknowledgements

We gratefully acknowledge Dugan Hayes for sharing experimental data. We thank Thomas Markovich for help obtaining correlation functions and spectral densities. We

acknowledge the Center for Excitonics, an Energy Frontier Research Center funded by the U.S. Department of Energy, Office of Science and Office of Basic Energy Sciences, under Award Number DE-SC0001088. S.M.B. acknowledges support from the United States Department of Energy through the Computational Sciences Graduate Fellowship (CSGF). D.I.G.B. and A.A.G. acknowledge the John Templeton Foundation (Grant Number 60469). D.I.G.B. and A.A.G. acknowledge CIFAR, the Canadian Institute for Advanced Research, for support through the Bio-Inspired Solar Energy program. This research used resources of the National Energy Research Scientific Computing Center, a DOE Office of Science User Facility supported by the Office of Science of the U.S. Department of Energy under Contract No. DEAC02-05CH11231. We thank Nvidia for support via the Harvard CUDA Center of Excellence. This research used computational time on the Odyssey cluster, supported by the FAS Division of Science, Research Computing Group at Harvard University.

3.7 Supplementary Information

3.7.1 System Hamiltonian

We describe energy transfer using a Frenkel exciton Hamiltonian and assume that only one of the pigments is excited at a time. The Hamiltonian of the single exciton manifold reads

$$H_{\text{ex}} = \sum_{m=1}^{N} \epsilon_m^0 |m\rangle\langle m| + \sum_{m>n} J_{mn}(|m\rangle\langle n| + |n\rangle\langle m|). \tag{3.1}$$

Here $|m\rangle$ denotes the state in which pigment m is excited while the other pigments remain in the electronic ground state. J_{mn} denotes the electronic coupling between the excited states on pigments m and n.

The pigments are coupled to the protein environment modeled by a set of independent harmonic oscillators

$$\mathcal{H}_{\text{phon}} = \sum_{m,i} \hbar\omega_i b_{i,m}^\dagger b_{i,m}, \tag{3.2}$$

and we assume a linear coupling of the exciton system to the vibrations

$$\mathcal{H}_{\text{ex-phon}} = \sum_m |m\rangle\langle m| \sum_i \hbar\omega_{i,m} d_{i,m}(b_{i,m} + b_{i,m}^\dagger). \tag{3.3}$$

The reorganization energy, $\lambda_m = \sum_i \hbar\omega_{i,m} d_{i,m}^2/2$, is added to the exciton energies in eqn (3.1), $\varepsilon_m = \varepsilon_m^0 + \lambda_m$. The phonon mode dependent coupling strength is captured by the spectral density

$$J_m(\omega) = \pi \sum_\xi \hbar^2 \omega_{\xi,m}^2 d_{\xi,m}^2 \delta(\omega - \omega_{\xi,m}) \tag{3.4}$$

which can also be defined as a sum of Drude-Lorentz peaks of form

$$J(\omega) = \sum_{i=1,s=\pm}^{N_{\text{peaks}}} \frac{\lambda_i \gamma_i \omega}{2} \frac{1}{\gamma_i^2 + (\omega + s\,\Omega_i)^2}. \tag{3.5}$$

where λ_i is the peak reorganization energy, γ_i defines the peak width, Ω_i defines the center frequency, and β is the inverse temperature.

3.7.2 Coarse Graining Spectral Densities

While HEOM is numerically exact, large reorganization energy values require substantial hierarchy depth to ensure convergence. We construct four classes of abridged spectral densities that include successively fewer peaks. Construction is guided by three metrics:

- L1 and L2 norms of error between the abridged and unabridged spectral densities
- the relative distribution of reorganization energy along the frequency axis, e.g. how much of the reorganization energy is contained between 0 and 200 cm^{-1} versus between 200 and 400 cm^{-1}, etc
- monomer absorption and fluorescence lineshapes

We note that no experimental data of any kind was referenced during spectral density

construction. Leveraging all four of these metrics simultaneously allows us to systematically and optimally reduce complexity while preserving essential observables given the constraints.

We define the first and most accurate set of spectral densities as Class 1, and these include 16 peaks for site A and 18 peaks for site B. Class 1 spectral densities have enough peaks to accurately capture all sharp features observed in the unabridged spectral densities, but contain too many bath modes to be applied to full-system calculations given the numerical complexity of the hierarchical equations of motion exciton dynamics method. Class 2 spectral densities include 11 peaks on site A and 8 peaks on site B and capture the vast majority of the sharp features observed in the unabridge spectral densities while also being usable for coherence dynamics simulations. Class 2.5 spectral densities contain seven peaks on each site, and while we do not reference them in the main text, we use them later in the SI when we examine coherence dynamics as a function of SD class. Class 3 spectral densities include four peaks on each site and are employed for our trajectory of 2D spectra. Spectral density parameters for all four classes are given in Table 3.2 and 3.2, and CIS spectral densities of Class 2, 2.5, and 3 are shown in Figure 3.11. While Class 1 spectral densities contain far too many peaks to use in HEOM, exact Kubo monomer lineshapes allow us to compare Class 1-3 spectral densities. As seen in Figure 3.4, we find almost no difference between the resulting monomer lineshapes, giving us confidence in our coarse graining.

3.7.3 Linear Spectra, Inhomogeneous Broadening and Transition Dipole Vectors

Absorption and fluorescence spectra simulated with HEOM and both CIS and SOS-CIS(D) Class 3 spectral densities are shown in Figure 4.18. Despite the substantially higher reorganization energy of SOS-CIS(D) SDs, both are observed to excellently reproduce the experimental Stokes shift. However, neither accurately captures the spectral

SiteA, Class1			**SiteB, Class1**		
$\lambda(cm^{-1})$	$\gamma(cm^{-1})$	$\Omega(cm^{-1})$	$\lambda(cm^{-1})$	$\gamma(cm^{-1})$	$\Omega(cm^{-1})$
204.0	25.0	15.0	160.0	35.0	0.0
143.0	55.0	107.5	50.0	28.0	102.0
66.0	41.0	224.0	64.0	35.0	179.0
63.0	34.0	299.0	32.0	36.0	249.0
27.0	25.0	447.0	42.0	37.0	308.0
17.0	50.0	510.0	4.0	40.0	370.0
23.4	28.0	564.0	8.0	50.0	425.0
54.0	30.0	681.0	20.0	32.0	514.0
4.0	30.0	800.0	15.0	32.0	547.0
4.0	30.0	850.0	18.0	30.0	580.0
4.6	25.0	961.0	50.0	28.0	682.0
4.4	30.0	1045.0	7.0	30.0	862.0
30.0	29.0	1138.0	2.0	28.0	965.0
34.0	36.0	1233.0	4.4	20.0	1055.0
128.0	34.0	1382.0	34.0	29.0	1130.0
14.0	18.0	1534.0	28.0	36.0	1240.0
			148.0	34.0	1382.0
			10.7	15.0	1535.0

SiteA, Class2			**SiteB, Class2**		
$\lambda(cm^{-1})$	$\gamma(cm^{-1})$	$\Omega(cm^{-1})$	$\lambda(cm^{-1})$	$\gamma(cm^{-1})$	$\Omega(cm^{-1})$
206.4	25.0	15.0	150.0	40.0	0.0
145.0	55.0	107.5	223.4	110.0	200.0
66.0	41.0	222.0	53.0	44.0	547.0
65.0	34.0	299.0	50.0	28.0	682.0
34.0	27.0	450.0	34.0	29.0	1130.0
33.0	32.0	560.0	28.0	36.0	1240.0
60.0	32.0	681.0	148.0	34.0	1382.0
32.0	29.0	1138.0	10.7	15.0	1535.0
35.0	36.0	1233.0			
130.0	34.0	1382.0			
14.0	18.0	1534.0			

Table 3.2: Class 1 and Class 2 CIS spectral density parameters.

SiteA, Class2.5 CIS			**SiteB, Class2.5 CIS**		
$\lambda(cm^{-1})$	$\gamma(cm^{-1})$	$\Omega(cm^{-1})$	$\lambda(cm^{-1})$	$\gamma(cm^{-1})$	$\Omega(cm^{-1})$
340.0	60.0	0.0	150.0	40.0	0.0
170.0	80.0	260.0	223.4	110.0	200.0
100.4	100.0	590.0	103.0	80.0	620.0
31.5	29.0	1138.0	34.0	29.0	1130.0
34.5	36.0	1233.0	28.0	36.0	1240.0
130.0	34.0	1382.0	148.0	34.0	1382.0
14.0	18.0	1534.0	10.7	15.0	1535.0
SiteA, Class3 CIS			**SiteB, Class3 CIS**		
$\lambda(cm^{-1})$	$\gamma(cm^{-1})$	$\Omega(cm^{-1})$	$\lambda(cm^{-1})$	$\gamma(cm^{-1})$	$\Omega(cm^{-1})$
340.0	60.0	0.0	150.0	40.0	0.0
170.0	80.0	260.0	210.0	110.0	200.0
100.4	100.0	590.0	97.1	80.0	620.0
210.0	60.0	1370.0	240.0	60.0	1373.0
SiteA, Class3 SOS − CIS(D)			**SiteB, Class3 SOS − CIS(D)**		
$\lambda(cm^{-1})$	$\gamma(cm^{-1})$	$\Omega(cm^{-1})$	$\lambda(cm^{-1})$	$\gamma(cm^{-1})$	$\Omega(cm^{-1})$
310.0	140.0	80.0	368.0	150.0	100.0
86.0	40.0	300.0	38.0	30.0	300.0
116.0	100.0	590.0	70.0	70.0	570.0
550.8	80.0	1350.0	490.9	70.0	1360.0

Table 3.3: Class 2.5 and Class 3 spectral density parameters.

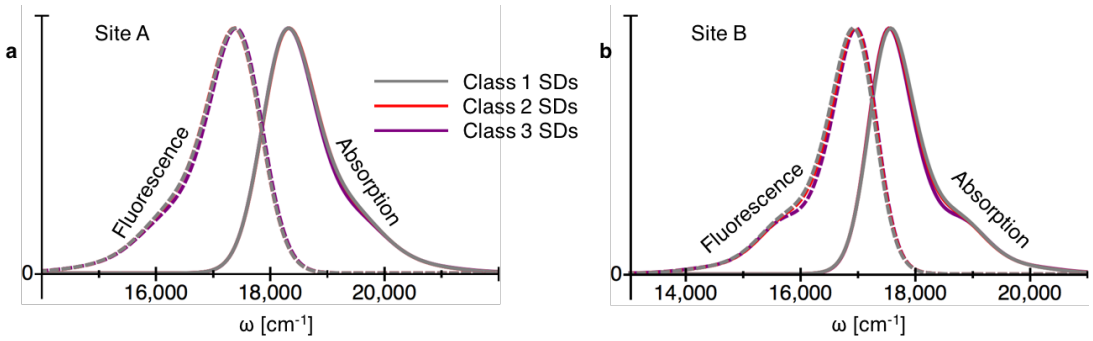

Figure 3.4: Monomer Kubo spectra as a function of spectral density class. Site A (left, **a**) and site B (right, **b**) absorption (solid) and fluorescence (dashed) monomer Kubo lineshapes using Class 1 (gray), Class 2 (red), and Class 3 (purple) spectral densities. Only very small changes are observed despite substantial differences in the spectral density parameterizations.

	$\mathbf{L_x}$	$\mathbf{L_y}$	$\mathbf{L_z}$
Site A	3.7344	-0.081708	-0.859594
Site A tweaked	2.40227	1.55316	-2.5511
Site B	2.57364	0.10163	-0.788947

Table 3.4: Transition dipole vectors given in atomic units.

width nor the correct relative peak heights. The former is due to our lack of inhomogeneous broadening that arrises from the many structures present in the ensemble, while the latter is due to the fact that we employ low quality CIS transition dipole moments. We apply ihomogeneous broadening to linear spectra through Gaussian weighting of both the dimer energy gap and the energy midpoint, and we correct the relative peak heights by a small 35 degree rotation of our site A transition dipole vector. After these two modifications, both CIS (Figure 3.2) and SOS-CIS(D) (Figure 3.6b) linear spectra are found to be in good agreement with experimental spectra. Transition dipole vectors including both raw and rotated site A vectors are given in Table 3.4.

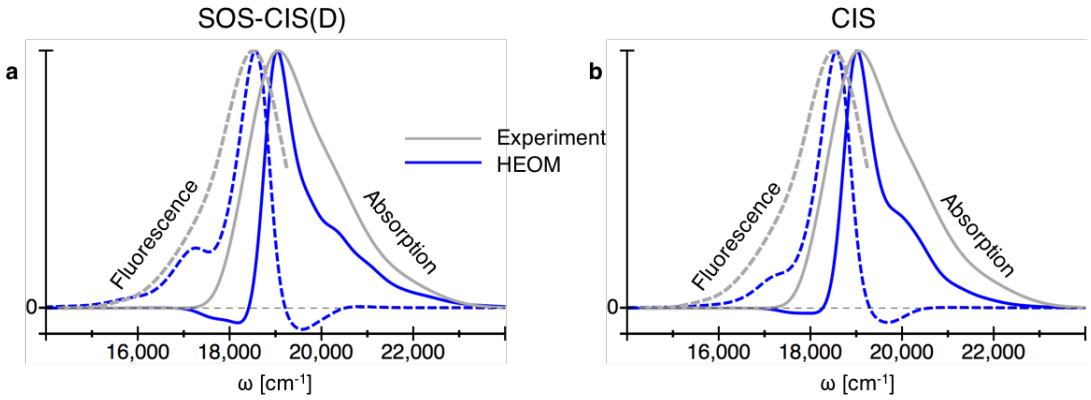

Figure 3.5: Absorption and fluorescence in the absence of inhomogeneous broadening or modifications to the transition dipole moments. SOS-CIS(D) (**a**) and CIS (**b**) absorption (solid) and fluorescence (dashed) for the AB dimer calculated with HEOM and Class 3 spectral densities (blue) versus experimental dimer spectra (gray).

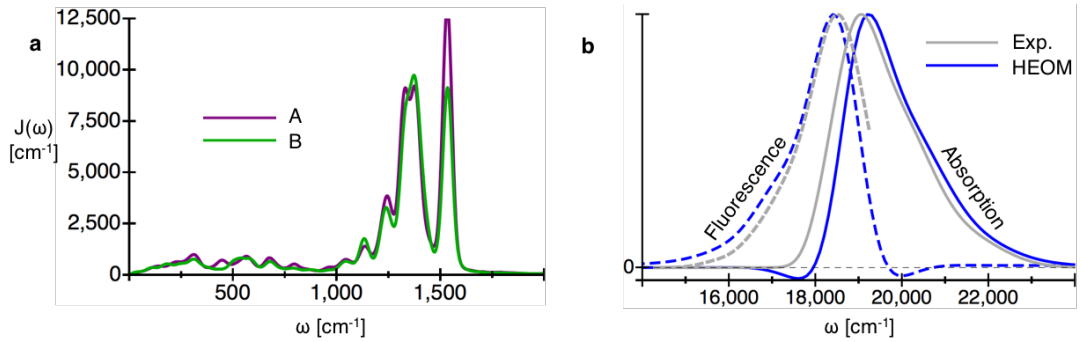

Figure 3.6: SOS-CIS(D) spectral densities and linear spectra. a, SOS-CIS(D) spectral densities for the A dye (purple) and for the B dye (green). **b**, A comparison of simulated (blue) and experimental (gray) linear spectral, where absorption is shown with solid lines and fluorescence is shown with dashed lines. Simulated spectra include 400 cm^{-1} of inhomogeneous broadening, a 2300 cm^{-1} constant shift, and a 35 degree rotation of one transition dipole vector, but are otherwise entirely *ab initio*.

3.7.4 The Weak Coupling Assumption

Experimentalists justify their assumption of weak coupling in large part through their observation that summed monomer spectra match dimer spectra (Figure 3.7). However, agreement for the AB dimer is of only middling quality, and both our CIS and SOS-CIS(D) simulated spectra are in significantly better agreement with experimental dimer spectra than the sum of experimental monomer spectra are. Furthermore, if we

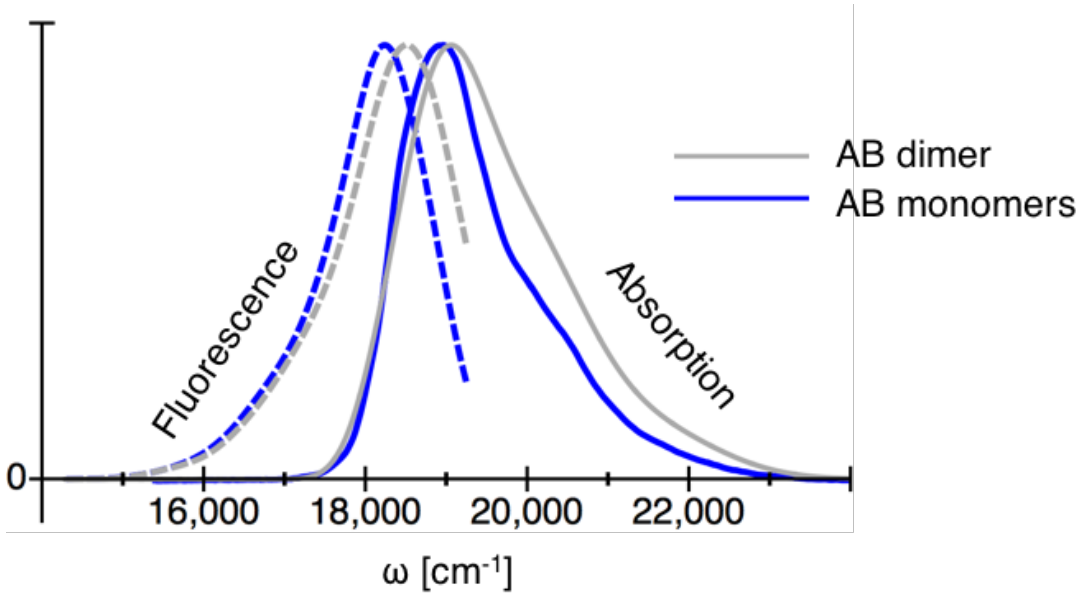

Figure 3.7: Experimental dimer versus summed monomer spectra. Dimer spectra are shown in gray while the summed monomer spectra are shown in blue.

reduce our coupling by a factor of ten in order to agree with the weak coupling assumption, simulated spectra massively overestimate Stokes shift and cannot be made to agree with experimental spectra under any set of transition dipole vectors (Figure 3.8).

3.7.5 CIS Versus SOS-CIS(D)

SOS-CIS(D) spectral densities have significantly more reorganization energy than CIS spectral densities, and the vast majority of that additional amplitude is contained in modes above 1000 cm^{-1}, as seen in Figure 3.9. While linear spectra simulated with both CIS and SOS-CIS(D) spectral densities are in good agreement with experiment, CIS spectral densities do a better job capturing the Stokes shift (Figure 3.2), and SOS-CIS(D) spectral densities do a better job capturing the lineshape (Figure 3.6). The lineshape comparison is better demonstrated by separately shifting absorption and fluorescence, as shown in Figure 3.10. We can see that the additional SOS-CIS(D) high-frequency spectral density amplitude fills in the spectral tails in better agreement with experiment while the

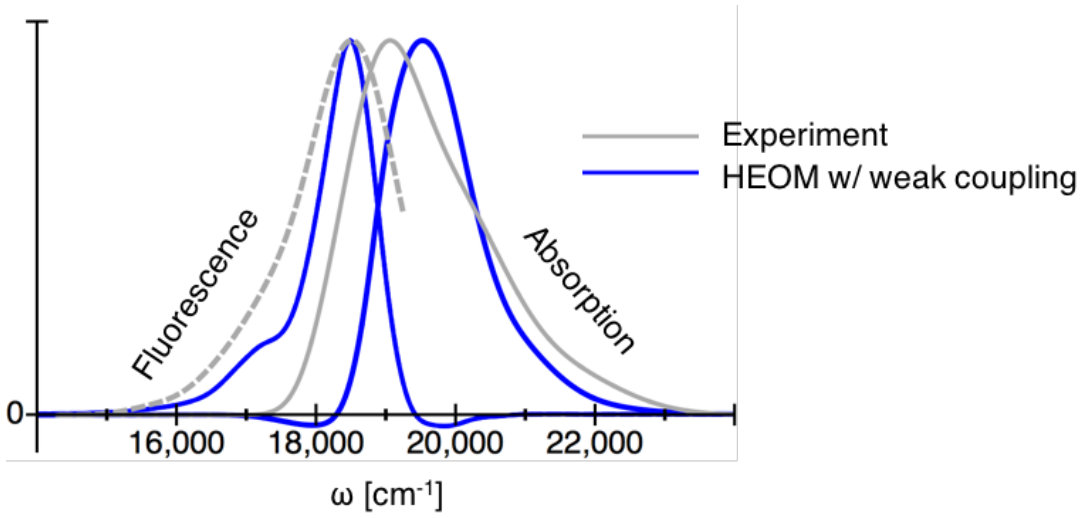

Figure 3.8: Linear spectra simulated with small coupling cannot capture experimental Stokes shift. Experimental dimer spectra are shown in gray while HEOM simulations of dimer spectra with coupling reduced by an order of magnitude are shown in blue.

larger overall reorganization energy causes the Stokes shift to be too large. Recalling once again that SOS-CIS(D) is only an energy correction, it is important to point out that the underlying diabatization is based on CIS electron densities, regardless of if we apply it to CIS or SOS-CIS(D) energies. Thus, it may be that while the energy correction improves the relative high-frequency peak heights or the relative distribution of reorganization energy between high- and low-frequency modes, the increased overall reorganization energy may be due to incorrectly exaggerated fluctuations coming from the mismatch of applying a CIS diabatization rotation to SOS-CIS(D) corrected energies. Given that CIS and SOS-CIS(D) spectral densities yield linear spectra of roughly equal qualities, and that smaller reorganization energies are easier to converge with HEOM, we avoid this mismatch and employ only CIS spectral densities going forward.

3.7.6 Coherence Dynamics as a Function of SD Class

While some observables change very slightly (population dynamics) or remain essentially unchanged (linear spectra) by moving from Class 2 to Class 3 spectral

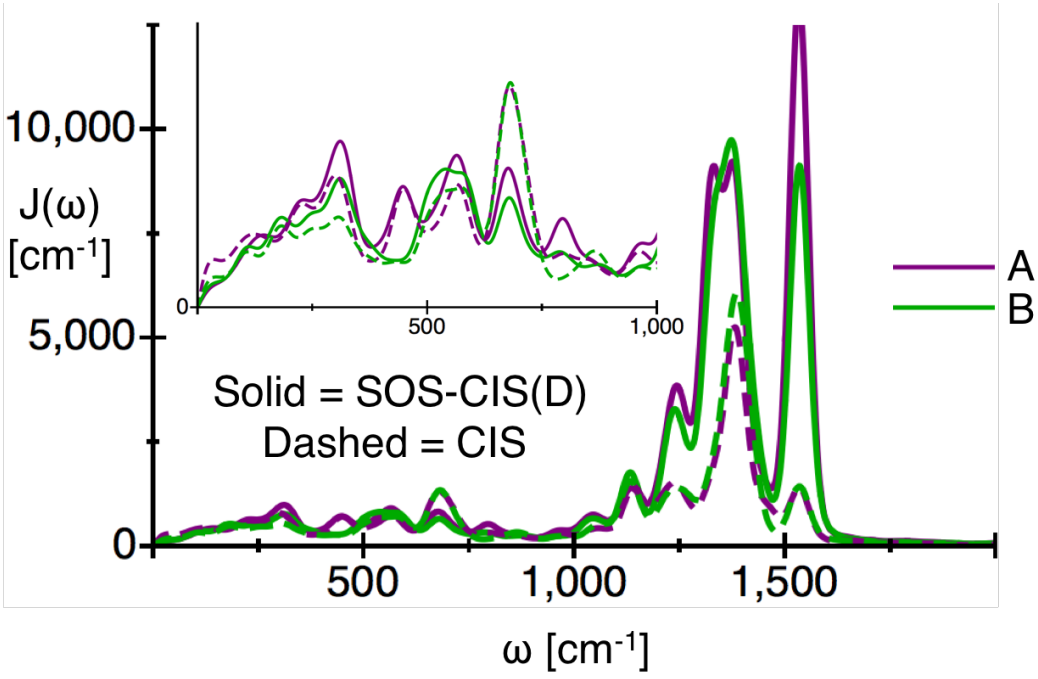

Figure 3.9: Comparing CIS and SOS-CIS(D) spectral densities. A dye SDs are shown in purple and B dye SDs are shown in green while simultaneously SOS-CIS(D) SDs are depicted with solid lines and CIS SDs are depicted with dashed lines.

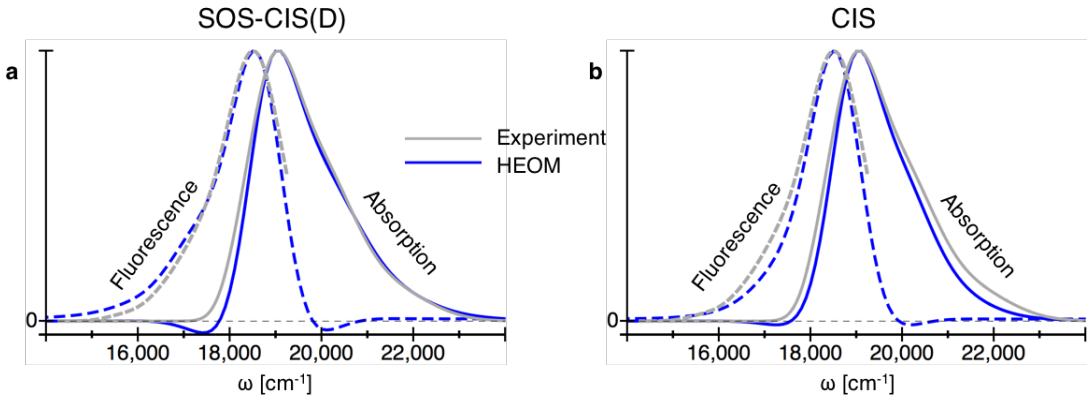

Figure 3.10: Comparing CIS and SOS-CIS(D) lineshapes. Simulated (blue) absorption (solid) and fluorescence (dashed) are shifted to precisely match experimental (gray) peak positions in order to compare the quality of the lineshapes obtained from SOS-CIS(D) spectral densities (**a**) and CIS spectral densities (**b**).

densities, long-time coherence dynamics intimately depend on specific sharp peaks in the spectral density and thus change substantially. In order to better clarify these effects and

to provide an intermediate data point between the very accurate Class 2 SDs and the very approximate Class 3 SDs, we parameteried Class 2.5 SDs with seven peaks on each site. In figure 3.11, we show Class 2, 2.5, and 3 SDs for both site A (Figure 3.11a) and site B (Figure 3.11b) as well as the resulting exciton coherences (Figure 3.11c). We then show the windowed FFT analysis for Class 2 (Figure 3.12), Class 2.5 (Figure 3.13) and Class 3 (Figure 3.14). While Class 2 SDs include sharp, long-lived vibrational peaks at both lower frequencies (400 - 700 cm^{-1}) and at higher frequencies (1100 - 1600 cm^{-1}), Class 2.5 SDs only include the high-frequency sharp peaks, and Class 3 SDs include only broad peaks. As a result, by 350 fs, coherence dynamics calculated with Class 2.5 SDs only show features at high frequencies (Figure 3.13), corresponding to their sharp peaks, and coherence dynamics calulated with Class 3 SDs show few features at all (Figure 3.14).

The particular sensitivity to small, sharp peaks calls into question the validity of the standard spectral density construction procedure in the field, which we employ, that includes convoluting the energy gap correlation function with a Gaussian to ensure that it decays to zero on timescales observed by experimental fluorescence line-narrowing experiments. Convolution with a Gaussian also broadens and merges spectral density peaks, aiding necessary coarse graining for methods like HEOM. Unfortunately, even if we modified our procedure to preserve small, sharp peaks in the spectral densities, we would not be able to incorporate them into our simulations because we are already at the limit of what is computationally feasable given that convergence requires a hierarchy depth of six. However, it is very likely that the true coherence dynamics of the system have even stronger long-lived oscillations due to the many additional small, sharp SD features that we unfortunately cannot include in our simulations.

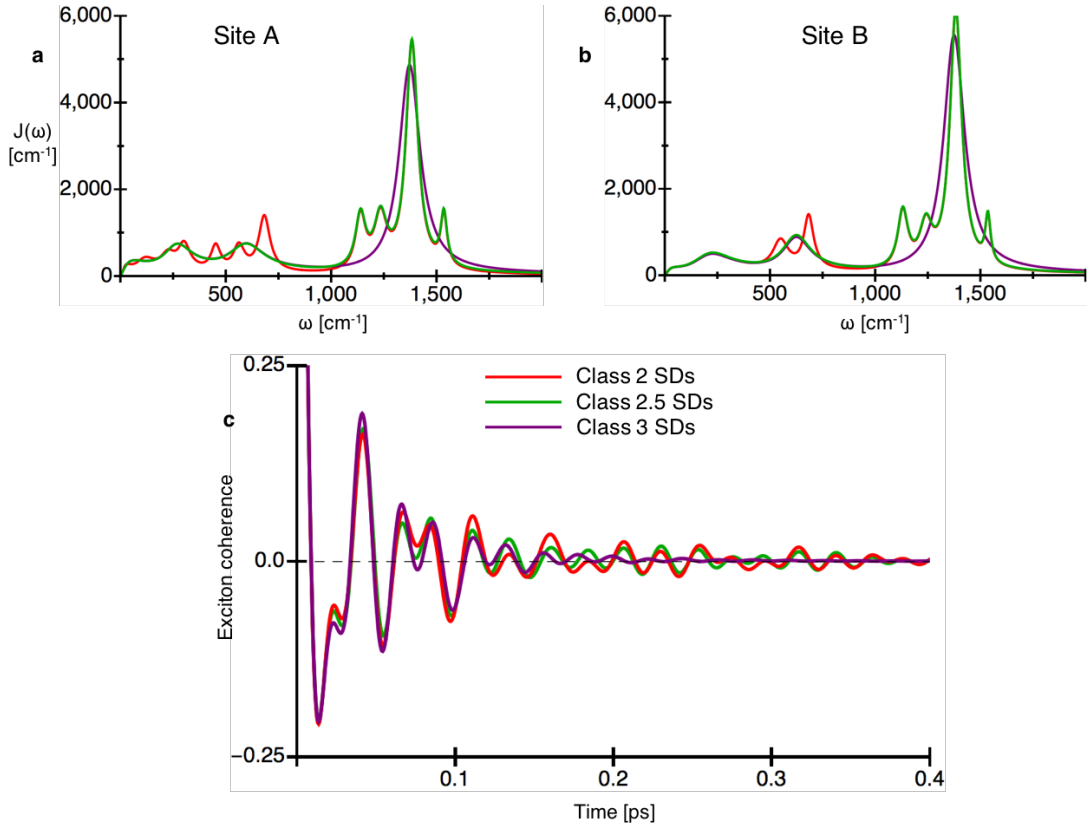

Figure 3.11: Coherence dynamics as a function of spectral density class. Class 2 (red), Class 2.5 (green), and Class 3 SDs for site A (**a**) and site B (**b**) as well as corresponding coherences (**c**).

3.7.7 Probing the Mechanism of Long-Lived Vibrationally Driven Coherences with Van Vleck Perturbation Theory

Vibronic mixing, e.g. the coherent interplay between the electronic degrees of freedom and very specific underdamped molecular vibrations, has been observed in several natural and artificial light-harvesting systems.[9,10] As we show in the main text, for the fluorescein dimer, such an entangled motion between the exciton system and vibrational modes manifest in a complex coherent dynamics that show rich features and various beat frequencies. Here, we investigate the nature of the vibronic mixing in deeper detail.

We demonstrate that the dynamics exhibits two types of coherence. One involves delocalization in the excitonic manifold and dominantly reflects the nature of electronic

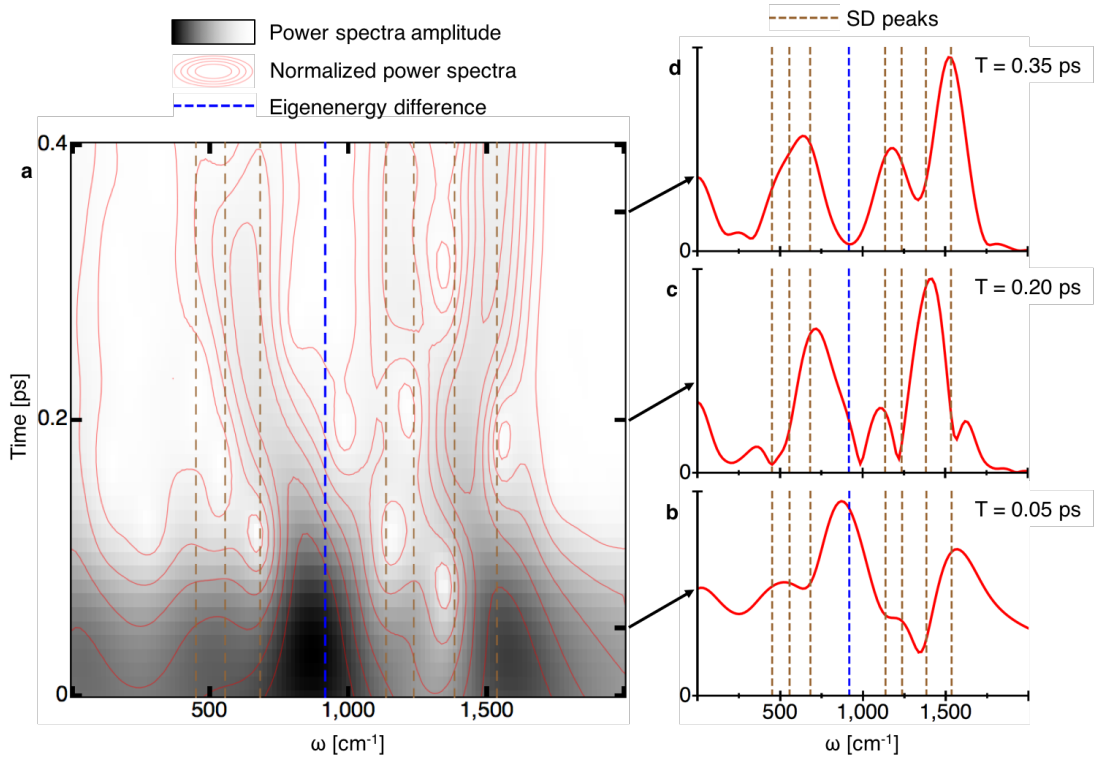

Figure 3.12: Disentangling coherence dynamics with Class 2 spectral densities. a, Windowed Fourier transform of coherence dynamics calculated with Class 2 SDs, where a grey scale denotes absolute power spectra amplitude, red contour lines denote normalized power spectra amplitude to better reveal long-time vibrational effects, the frequency of electronic coherence is shown in dashed blue, and select SD peaks are shown in dashed brown. Note that the dark feature in the bottom middle of the panel denotes electronic coherence. **b**, Windowed FFT time slice at 0.05 ps. **c**, Windowed FFT time slice at 0.2 ps. **d**, Windowed FFT time slice at 0.35 ps.

coherence, while the other is of dominant vibrational nature, resulting from a coherent mixing of vibrational quanta. The latter carries the frequency of the underdamped vibrational modes (see main text Figure 3.3) and can be associated with the long-lasting oscillatory component in the EET. The coherence life-time is defined by the life-time of the vibrational mode itself. Note that the vibronic interaction is critical for this vibrationally driven coherence to be seen in the single-exciton manifold. This distinguishes this type of coherence from ground-state vibrations, for which both pigments remain in the electronic ground state, which has been found to affect cross-peak beatings in the 2D electronic spectra.[7]

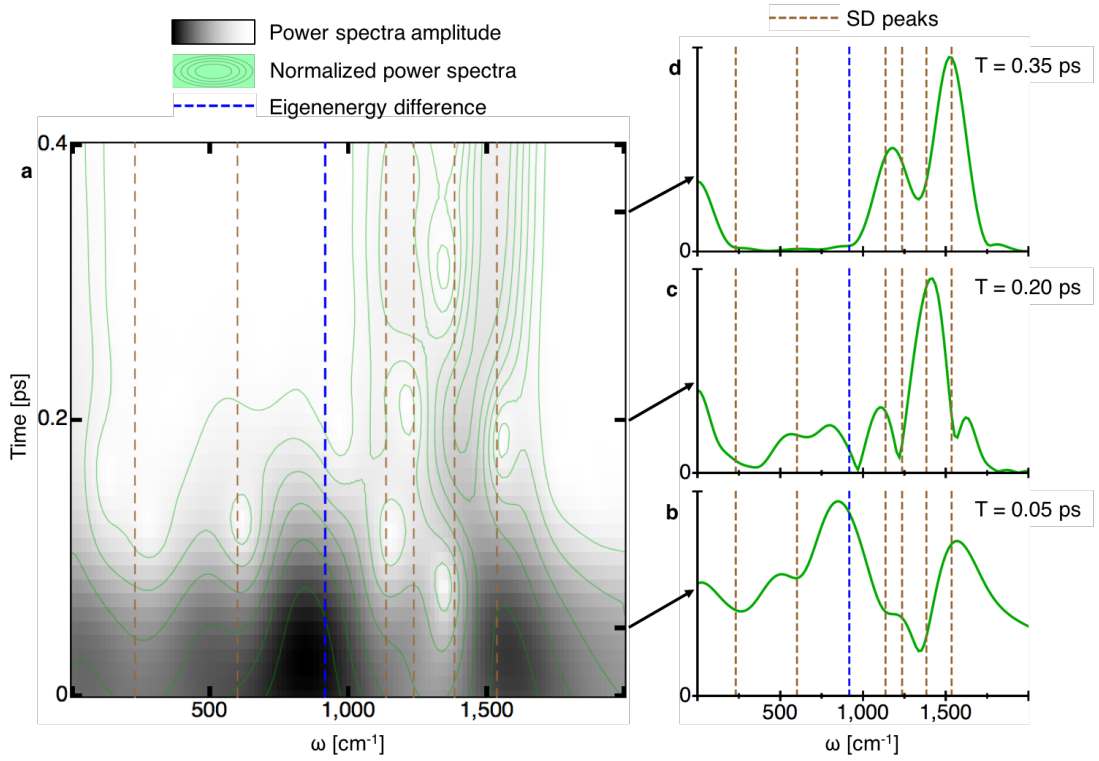

Figure 3.13: Disentangling coherence dynamics with Class 2.5 spectral densities. a, Windowed Fourier transform of coherence dynamics calculated with Class 2.5 SDs, where a grey scale denotes absolute power spectra amplitude, green contour lines denote normalized power spectra amplitude to better reveal long-time vibrational effects, the frequency of electronic coherence is shown in dashed blue, and select SD peaks are shown in dashed brown. Note that the dark feature in the bottom middle of the panel denotes electronic coherence. **b**, Windowed FFT time slice at 0.05 ps. **c**, Windowed FFT time slice at 0.2 ps. **d**, Windowed FFT time slice at 0.35 ps.

Vibronic effects have been studied previously in literature in the context of the James-Cummings model with various applications in quantum optics and cavity quantum electrodynamics. Under certain limiting regimes, insights into vibronic states and resulting frequencies have been obtained analytically. We carry out a similar analysis for a excitonic dimer system for which each pigment strongly couples to an underdamped vibrational mode. Analogous to Ref.,[194] we derive explicit analytical expressions based on a van-Vleck perturbation theory which allows us to unambiguously characterize the nature of coherence in the fluorescein dimer.

In the following, we consider a dimer system with two pigments and a spectral density

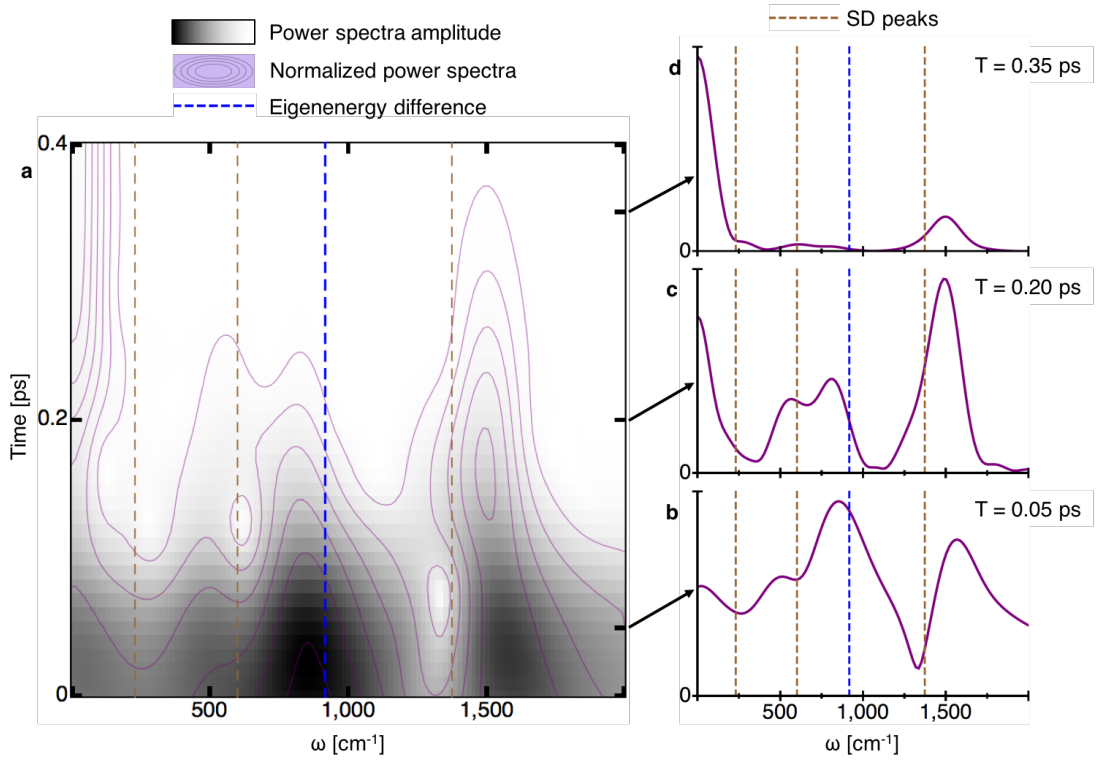

Figure 3.14: Disentangling coherence dynamics with Class 3 spectral densities. a, Windowed Fourier transform of coherence dynamics calculated with Class 2 SDs, where a grey scale denotes absolute power spectra amplitude, purple contour lines denote normalized power spectra amplitude to better reveal long-time vibrational effects, the frequency of electronic coherence is shown in dashed blue, and select SD peaks are shown in dashed brown. Note that the dark feature in the bottom middle of the panel denotes electronic coherence. **b**, Windowed FFT time slice at 0.05 ps. **c**, Windowed FFT time slice at 0.2 ps. **d**, Windowed FFT time slice at 0.35 ps.

which contains a single underdamped vibrational mode at each pigment. This model can be equivalently described by a two level system coupled to two harmoic oscillators

$$\begin{aligned}\mathcal{H} =&\varepsilon \left|1\right\rangle \left\langle 1\right| - J(\left|1\right\rangle \left\langle 2\right| + \left|2\right\rangle \left\langle 1\right|) + \hbar\Omega\sqrt{S}\left|1\right\rangle \left\langle 1\right|(b_1^\dagger + b_1) \\ &+ \hbar\Omega\sqrt{S}\left|2\right\rangle \left\langle 2\right|(b_2^\dagger + b_2) + \hbar\Omega b_1^\dagger b_1 + \hbar\Omega b_2^\dagger b_2, \end{aligned} \tag{3.6}$$

where the oscillators are weakly coupled to a Ohmic bath.[195,196] We assume identical Huang-Rhys factors $S = \lambda/\Omega$ and frequencies Ω for the distinct vibrations at each pigment.

Within Van-Vleck perturbation theory we expand the vibronic Hamiltonian eq. (3.6) up to second order in the exciton-vibrational coupling $g = \Omega\sqrt{S}$

$$\mathcal{H} = \mathcal{H}_0 + \mathcal{V}_1 + \mathcal{V}_2. \tag{3.7}$$

with

$$\begin{aligned}\mathcal{V}_1 =& g(\cos^2\theta\,|e_0\rangle\langle e_0| + \sin^2\theta\,|e_1\rangle\langle e_1| - \cos\theta\sin\theta(|e_1\rangle\langle e_0| + |e_0\rangle\langle e_1|))(b_1^\dagger + b_1)\\ \mathcal{V}_2 =& g(\sin^2\theta\,|e_0\rangle\langle e_0| + \cos^2\theta\,|e_1\rangle\langle e_1| + \cos\theta\sin\theta(|e_1\rangle\langle e_0| + |e_0\rangle\langle e_1|))(b_2^\dagger + b_2).\end{aligned} \tag{3.8}$$

Here, we expanded the interaction terms into the eigenstates of the unperturbed Hamiltonian $\mathcal{H}_0$

$$|e_0, n_1, n_2\rangle = (\cos\theta\,|1\rangle + \sin\theta\,|2\rangle) \otimes |n_1\rangle \otimes |n_2\rangle \tag{3.9}$$

$$|e_1, n_1, n_2\rangle = (-\sin\theta\,|1\rangle + \cos\theta\,|2\rangle) \otimes |n_1\rangle \otimes |n_2\rangle\,. \tag{3.10}$$

The spectrum of the unperturbed Hamiltonian $\mathcal{H}_0$ as function of Ω is shown in Fig. 3.15(a).

Van-Vleck perturbation assumes that the unperturbed spectrum can be grouped around resonance condition $\hbar\Omega = \Delta$ into energetically separated manifolds. In our case the eigenstates of $\mathcal{H}_0$ form following manifolds

$$\begin{aligned}&\{|j=0,\alpha\rangle\} = \{|e_0,0,0\rangle\}\\ &\{|j=1,\alpha\rangle\} = \{|e_0,1,0\rangle,\ |e_0,0,1\rangle,\ |e_1,0,0\rangle\}\\ &\{|j=2,\alpha\rangle\} = \{|e_0,2,0\rangle,\ |e_0,0,2\rangle,\ |e_0,1,1\rangle,\ |e_1,1,0\rangle,\ |e_1,0,1\rangle\}\\ &\qquad ...\end{aligned} \tag{3.11}$$

Van-Vleck perturbation theory there exists a transformation $\mathcal{S}$ which brings the system

Hamiltonian $\mathcal{H}$ into a block-diagonal form. Expanding $\mathcal{S} = \mathcal{S}^{(1)} + \mathcal{S}^{(2)} + \mathcal{O}(g^3)$ and $\mathcal{H}_{\text{eff}} = \mathcal{H}_{\text{eff}}^{(0)} + \mathcal{H}_{\text{eff}}^{(1)} + \mathcal{H}_{\text{eff}}^{(2)} + \mathcal{O}(g^3)$ up to second order perturbation in g we obtain following expressions for the matrix elements of the effective Hamiltonian

$$\begin{aligned} \langle i,\alpha|\,\mathcal{H}_{\text{eff}}\,|j,\alpha\rangle &= E_{j,\alpha}\delta_{ij} + \langle i,\alpha|\,\mathcal{V}\,|j,\alpha\rangle \\ &+ \frac{1}{2}\sum_{k,\beta\neq\alpha} \langle i,\alpha|\,\mathcal{V}\,|k,\beta\rangle\,\langle k,\beta|\,\mathcal{V}\,|j,\alpha\rangle\,\Big[\frac{1}{E_{i,\alpha}-E_{k,\beta}} + \frac{1}{E_{j,\alpha}-E_{k,\beta}}\Big] \end{aligned} \tag{3.12}$$

For high frequency vibrational modes $\hbar\Omega \gg k_b T$ only the two lowest energetic manifolds are expected to contribute to the dynamics and we obtain

$$\mathcal{H}_{\text{eff}} = \left[\begin{array}{c|ccc} -\Delta - (\cos^4\theta + \sin^4\theta)\Omega S & & & \\ \quad -2\cos^2\theta\ \sin^2\theta\ \Omega^2 S\frac{1}{2\Delta+\Omega} & & & \\ \hline & \Delta - (\cos^4\theta + \sin^4\theta)\Omega S & -\cos\theta\ \sin\theta\ \Omega\sqrt{S} & \cos\theta\ \sin\theta\ \Omega\sqrt{S} \\ & -\cos\theta\ \sin\theta\ \Omega\sqrt{S} & -\Delta + \Omega - (\cos^4\theta + \sin^4\theta)\Omega S & \cos^2\theta\ \sin^2\theta\ \Omega^2 S\frac{1}{2\Delta+\Omega} \\ & & -3\sin^2\theta\ \cos^2\theta\ \Omega^2 S\frac{1}{2\Delta+\Omega} & \\ & \cos\theta\ \sin\theta\ \Omega\sqrt{S} & \cos^2\theta\ \sin^2\theta\ \Omega^2 S\frac{1}{2\Delta+\Omega} & -\Delta + \Omega - (\cos^4\theta + \sin^4\theta)\Omega S \\ & & & -3\sin^2\theta\ \cos^2\theta\ \Omega^2 S\frac{1}{2\Delta+\Omega} \end{array}\right]. \tag{3.13}$$

The lowest energy state is given by the low-energy exciton state for which both vibrations are in the ground state

$$|E_0\rangle = |e_0,0,0\rangle\,. \tag{3.14}$$

The vibronic coupling in the 3×3 block matrix leads to a mixing of the states $|e_1,0,0\rangle$, $|e_0,1,0\rangle$ and $|e_0,0,1\rangle$. Diagonalizing this block reveals that the vibronic state

$$|E_2\rangle = \frac{1}{\sqrt{2}}(|e_0,1,0\rangle + |e_0,0,1\rangle \tag{3.15}$$

mixes only the vibrational quanta at the two pigments, while the exciton system remains

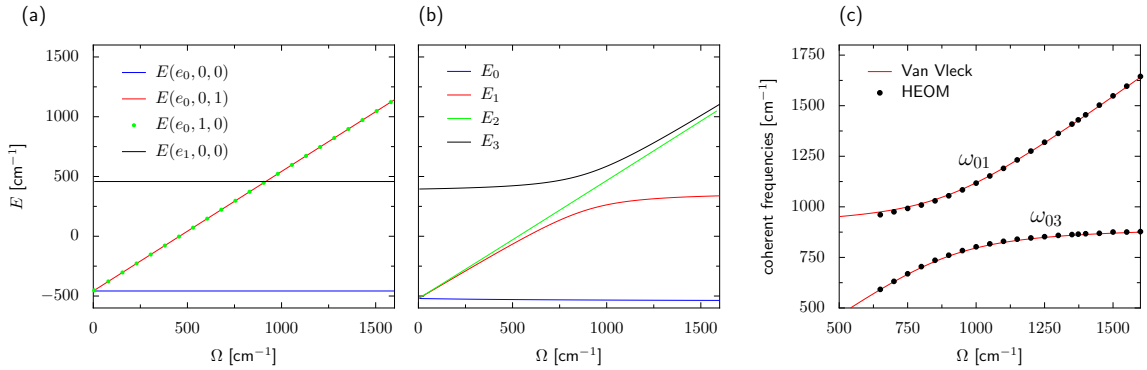

Figure 3.15: Spectrum of the (a) unperturbed Hamiltonian $\mathcal{H}_0$ and (b) the full Hamiltonian $\mathcal{H}$ as function of the vibrational frequency Ω. The used parameters $\varepsilon = -599$ cm^{-1}, $J = -346.3$ cm^{-1} and $\lambda = 88$ cm^{-1} reflect the situation of the Fluorescein dimer. (c) Comparison of the extracted frequencies from the dynamics of the exciton coherence computed with HEOM compared to the analytical results derived from the Van Vleck perturbation theory.

in its low energy state. The remaining two vibronic states can be written in following form

$$|E_1\rangle = a_1 |e_1,0,0\rangle + b_1(|e_0,1,0\rangle - |e_0,0,1\rangle) \tag{3.16}$$

$$|E_3\rangle = a_3 |e_1,0,0\rangle + b_3(|e_0,1,0\rangle - |e_0,0,1\rangle). \tag{3.17}$$

The vibronic coupling leads to an avoided crossing as is depicted in Fig. 3.15(b).

In the main text we probe the life-time of coherence in the EET by studying the evolution of exciton coherences. To this end we prepare the system in the artificial initial state $\rho(t_0) = |e_0,0,0\rangle\langle e_1,0,0|$. Expanding $\rho(t_0)$ in the vibronic basis yields

$$\rho(t_0) = \alpha|E_0\rangle\langle E_1| - \beta|E_0\rangle\langle E_3| \tag{3.18}$$

with $\alpha = b_3/b_1/N$ and $\beta = 1/N$, where $N = a_1 b_3/b_1 - a_3$. Therefore the coherent dynamics

$$\rho(t) = \alpha|E_0\rangle\langle E_1|exp(i(E_1 - E_0)t) - \beta|E_0\rangle\langle E_3|exp(i(E_3 - E_0)t) \tag{3.19}$$

exhibit the frequencies $\hbar\omega_{01} = E_1 - E_0$ and $\hbar\omega_{03} = E_3 - E_1$.

In Figure 3.15c we compare the expected frequencies based on the Van-Vleck perturbation theory with accurate HEOM simulations. Note, that in the latter we included a Drude-Lorentz spectral density with $\lambda = 10$ cm^{-1} as dissipative background. We reduced the dissipative background by more than one order of magnitude when compared to the fluorescein dimer in order to better resolve the frequencies in the FFT analysis of the coherences. We find a very good agreement between the expected frequencies from the analytical results and the ones extracted from the HEOM calculations, hence validating the assumptions made in the Van-Vleck perturbation theory.

Finally, we investigate the nature of the coherence assigned to the frequencies ω_{01} and ω_{03} in the dynamics of the fluorescein dimer. As is shown in the main text, the coherent dynamics are governed by various vibrational frequencies for which the vibrational mode around 1500 cm^{-1} ($S = 0.01$) is the most distinct. Analyzing the corresponding vibronic states we find that

$$|E_0\rangle\langle E_1| \approx a_1|e_0\rangle\langle e_1| \otimes |0,0\rangle\langle 0,0| \tag{3.20}$$

corresponds to a dominant electronic coherence, while

$$|E_0\rangle\langle E_3| \approx b_3|e_0\rangle\langle e_0| \otimes (|0,0\rangle\langle 1,0| - |0,0\rangle\langle 0,1|) \tag{3.21}$$

shares a dominant vibrational coherent character, which explains our assignment of the oscillatory frequencies in the main text. For the fluorescein dimer the exciton system couples to multiple underdamped vibrational modes resulting in a more complex dynamics showing multiple vibrational frequencies.

3.7.8 2D Pathway Oscillations

While experiments can only probe the overall 2D signal that is a sum of all pathways, our simulations allow us to examine off-diagonal oscillations of each pathway individually (Figure 3.16). We perform a windowed FFT analysis on the the summed signal (Figure

3.17), the SERP pathway (Figure 3.18), the ESARP pathway (Figure 3.19) and the GBRP pathway (Figure 3.20), where signal background has been removed using a sum of two exponentials consistent with experimental methods. Due to the computational complexity of 2D simulations, we are restricted to Class 3 SDs, which include only broad peaks with erroneously short vibrational lifetimes. Given that our windowed FFT analysis reveals that peaks in long-time power spectra in all pathways correspond to SD peak frequencies, it is thus unsurprising that our observed oscillations decay significantly earlier than those observed experimentally. If we were able to include more accurate SDs, such as Class 2 SDs, we expect we would see significantly longer-lived and larger magnitude oscillations in better agreement with experiment, as was exactly the case for the coherence dynamics.

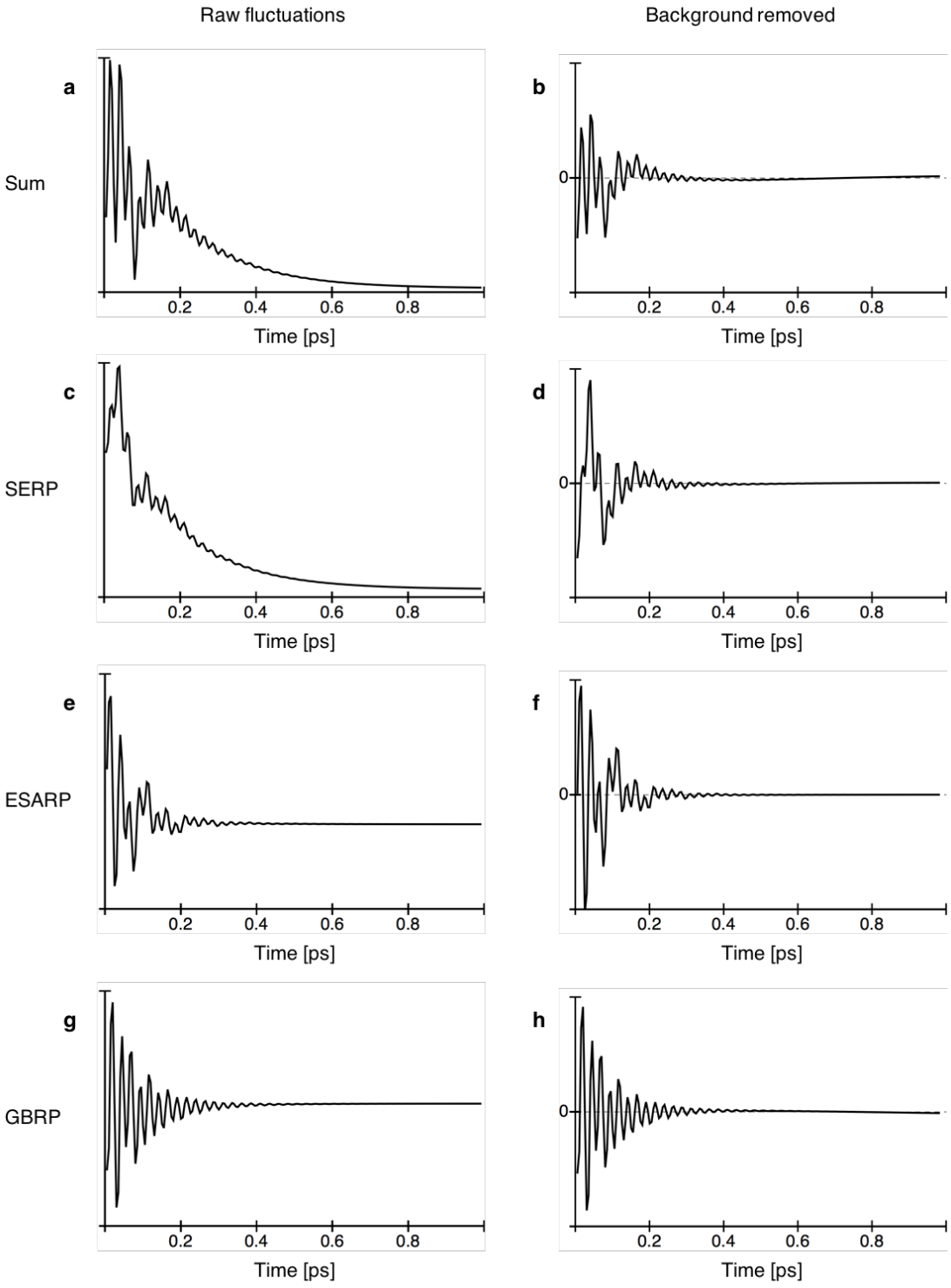

Figure 3.16: Off-diagonal 2D oscillations of each pathway. Oscillations of all pathways summed together shown with (**a**) and without (**b**) background. SERP pathway oscillations with (**c**) and without (**d**) background. ESARP pathway oscillatioins with (**e**) and without (**f**) background. GBRP pathway oscillations with (**g**) and without (**h**) background.

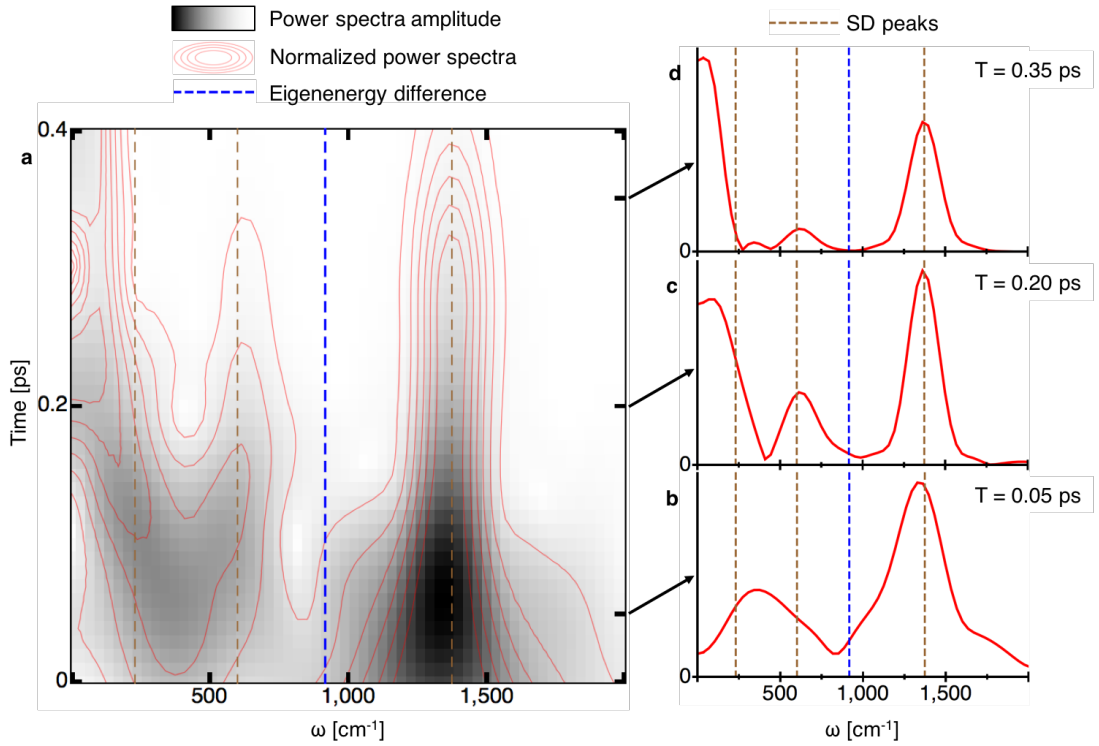

Figure 3.17: Windowed FFT of summed oscillations. a, Windowed Fourier transform of off-diagonal oscillations of all summed pathways calculated with Class 3 SDs, where a grey scale denotes absolute power spectra amplitude, red contour lines denote normalized power spectra amplitude to better reveal long-time vibrational effects, the frequency of electronic coherence is shown in dashed blue, and SD peak positions are shown in dashed brown. **b**, Windowed FFT time slice at 0.05 ps. **c**, Windowed FFT time slice at 0.2 ps. **d**, Windowed FFT time slice at 0.35 ps.

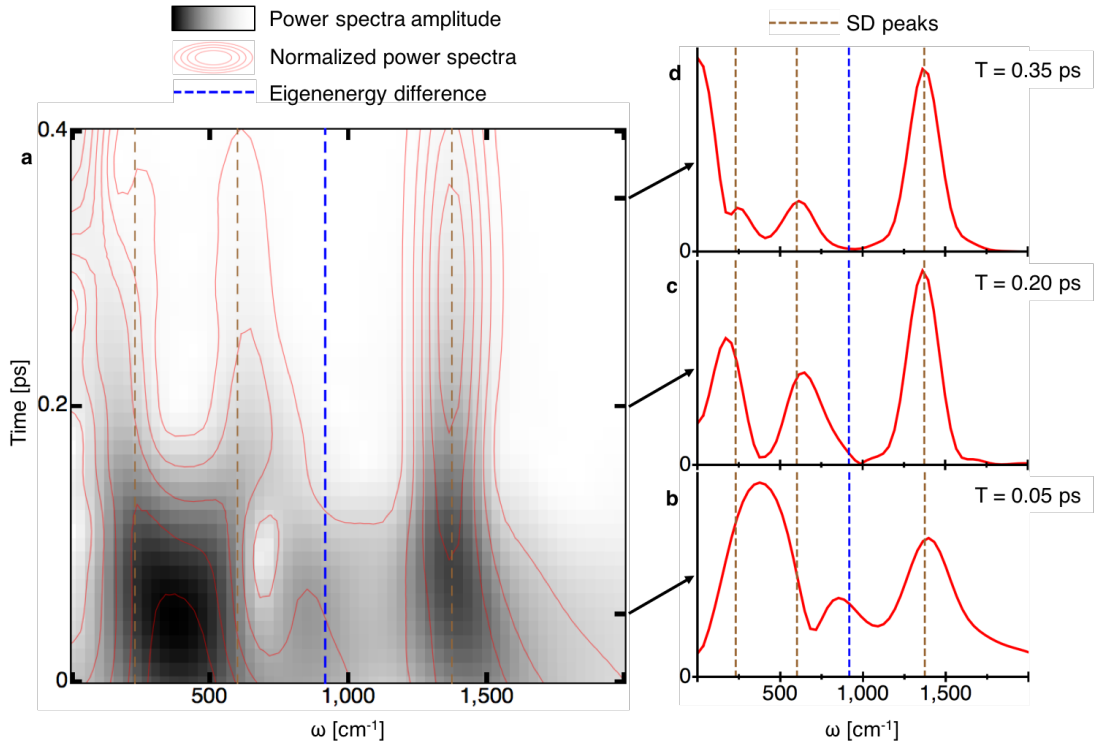

Figure 3.18: Windowed FFT of SERP oscillations. a, Windowed Fourier transform of off-diagonal oscillations of the SERP pathway calculated with Class 3 SDs, where a grey scale denotes absolute power spectra amplitude, red contour lines denote normalized power spectra amplitude to better reveal long-time vibrational effects, the frequency of electronic coherence is shown in dashed blue, and SD peak positions are shown in dashed brown. **b**, Windowed FFT time slice at 0.05 ps. **c**, Windowed FFT time slice at 0.2 ps. **d**, Windowed FFT time slice at 0.35 ps.

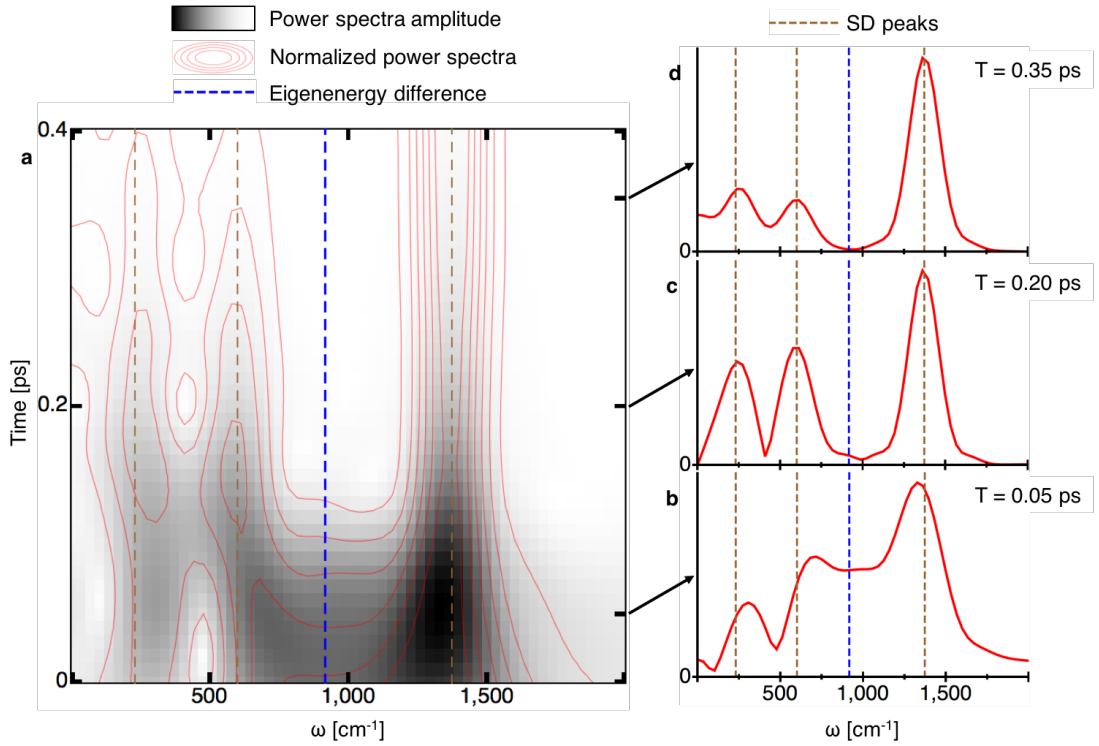

Figure 3.19: Windowed FFT of ESARP oscillations. a, Windowed Fourier transform of off-diagonal oscillations of the ESARP pathway calculated with Class 3 SDs, where a grey scale denotes absolute power spectra amplitude, red contour lines denote normalized power spectra amplitude to better reveal long-time vibrational effects, the frequency of electronic coherence is shown in dashed blue, and SD peak positions are shown in dashed brown. **b**, Windowed FFT time slice at 0.05 ps. **c**, Windowed FFT time slice at 0.2 ps. **d**, Windowed FFT time slice at 0.35 ps.

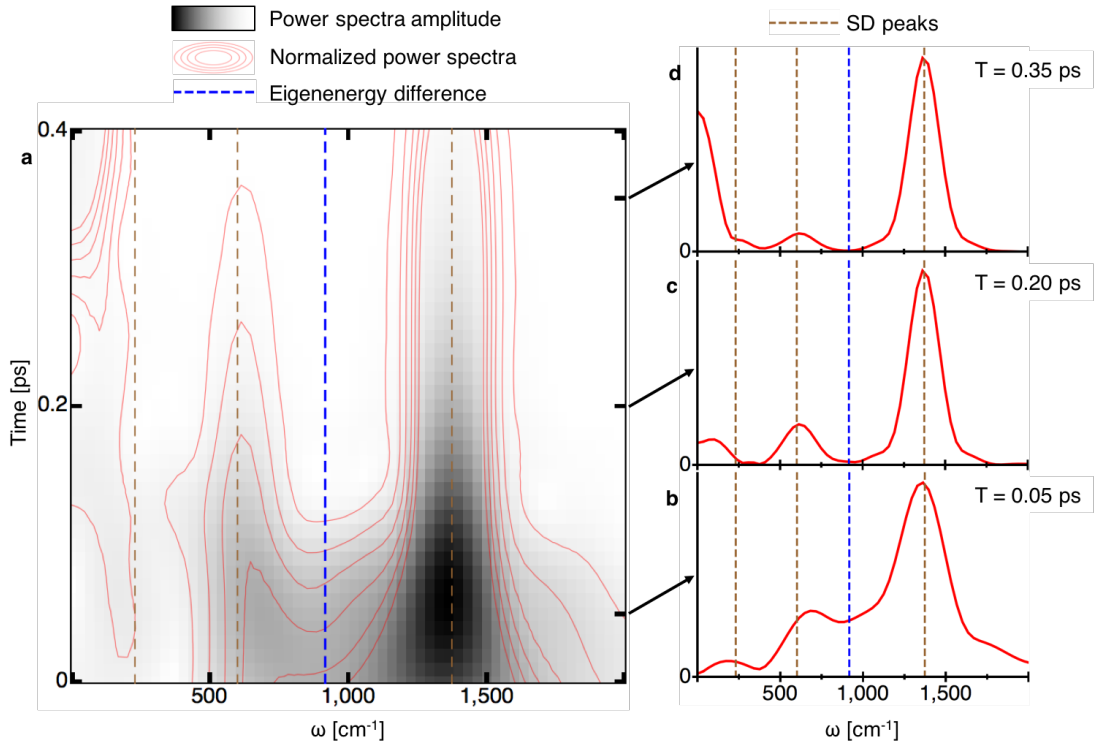

Figure 3.20: Windowed FFT of GBRP oscillations. a, Windowed Fourier transform of off-diagonal oscillations of the GBRP pathway calculated with Class 3 SDs, where a grey scale denotes absolute power spectra amplitude, red contour lines denote normalized power spectra amplitude to better reveal long-time vibrational effects, the frequency of electronic coherence is shown in dashed blue, and SD peak positions are shown in dashed brown. **b**, Windowed FFT time slice at 0.05 ps. **c**, Windowed FFT time slice at 0.2 ps. **d**, Windowed FFT time slice at 0.35 ps.

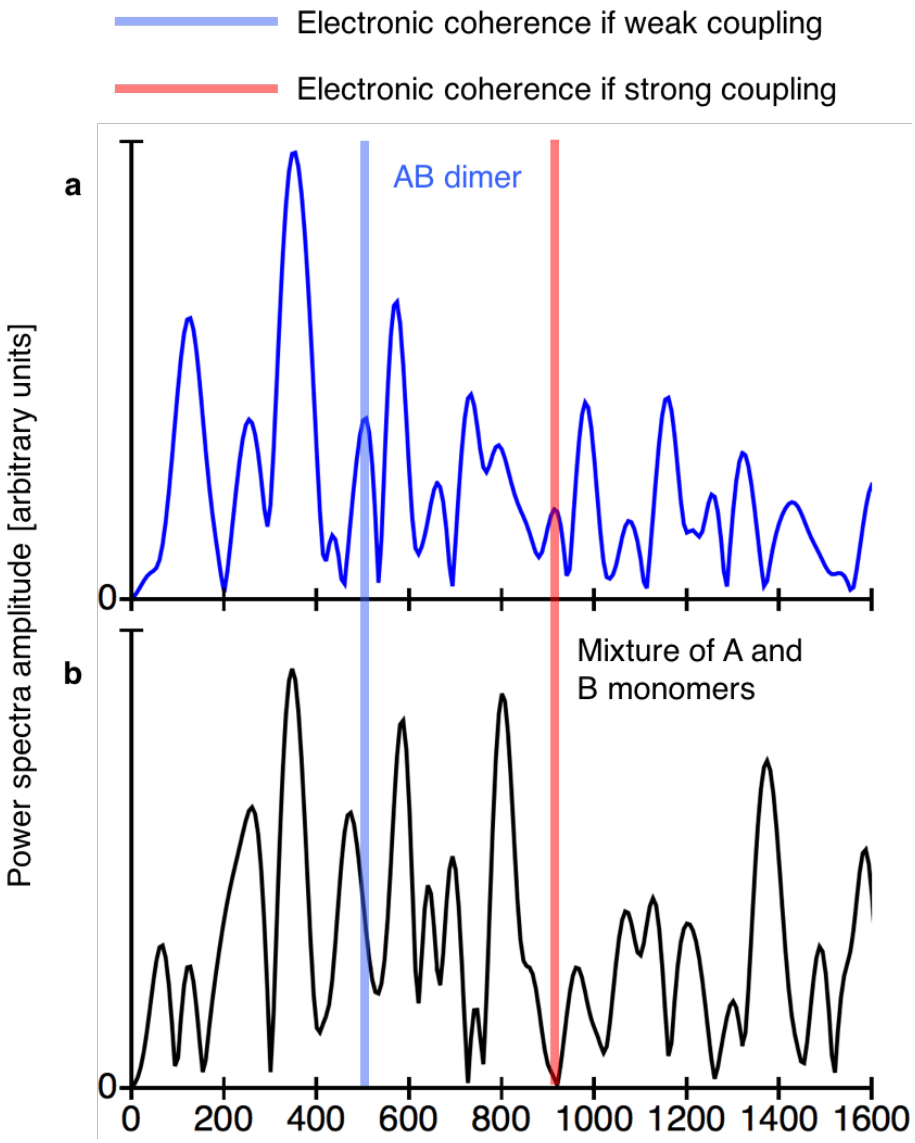

Figure 3.21: Experimental off-diagonal 2D oscillation power spectra of AB dimer and of a mixture of A and B monomers. a, Dimer power spectrum. **b**, Mixture of monomers power spectrum. The site energy difference, aka the frequency of electronic coherence if the dimers are weakly coupled, is shown in light blue while our eigenenergy difference, aka the frequency of electronic coherence if the dimers are strongly coupled, is shown in light red.

4

Ab Initio Simulations of AC and BC Fluorescein Dimers

4.1 Introduction

Here I present additional work on the AC and BC fluorescein dimers. What we believe to be an accidental swap of experimental absorption spectra led us to write up the work on the AB dimer by itself rather than having to deal with this issue. However, I have essentially the same level of data for the AC and BC dimers, thus I report and briefly discuss it here.

4.2 Site Energy Comparison

As with the AB dimer, we propagated QM/MM trajectories and calculated diabatized exicited states every 2.5 fs. We can now examine the validity of our diabatization by comparing our site energies across the three dimers, as seen in Table 4.1 and Table 4.2. The consistency of identical dye energies between dimers, e.g. the A dye in the AB dimer and the A dye in the AC dimer, is fantastic, especially for the more accurate SOS-CIS(D). Furthermore, while the SOS-CIS(D) AB dimer site energy gap was only in decent agreement with experiment (593 cm^{-1} vs 500 cm^{-1}), the gaps for the AC and BC dimers are incredibly within experimental error: 696.6 cm^{-1} vs 703 $\pm$ 10 cm^{-1} for the AC dimer and 199.8 cm^{-1} vs 195 $\pm$ 5 cm^{-1} for the BC dimer. This consistency of site energies and

	AB	AC	BC
$E_A[eV]$	3.555	3.584	
$E_B[eV]$	3.450		3.455
$E_C[eV]$		3.502	3.506
$\Delta E[cm^{-1}]$	850.7	657.0	411.0
$V_{AB}[cm^{-1}]$	448.1	434.2	450.4
$\lambda_A[cm^{-1}]$	820.4	844.5	
$\lambda_B[cm^{-1}]$	697.1		763.1
$\lambda_C[cm^{-1}]$		716.5	731.3

Table 4.1: Comparing CIS and experimental absolute energies, energy gaps, couplings, and reorganization energies for all three fluorescein dimers.

	AB	AC	BC
$E_A[eV]$	2.210	2.214	
$E_B[eV]$	2.137		2.147
$E_C[eV]$		2.128	2.123
$\Delta E[cm^{-1}]$	593.0	696.6	199.8
$V_{AB}[cm^{-1}]$	346.3	424.3	363.6
$\lambda_A[cm^{-1}]$	1062.8	1116.0	
$\lambda_B[cm^{-1}]$	966.9		980.0
$\lambda_C[cm^{-1}]$		1175.2	898.8

Table 4.2: Comparing SOS-CIS(D) and experimental absolute energies, energy gaps, couplings, and reorganization energies for all three fluorescein dimers.

couplings gives us substantial confidence in the accuracy of our system Hamiltonians.

4.3 Spectral Densities and Linear Spectra

We coarse grained our spectral densities and simulated linear spectra for both the AC and BC dimers exactly as described for the AB dimer. While transition dipoles required slightly larger rotations in order to correct relative peak heights (45 degrees for AC, 90 degrees for BC), the resulting spectra are in very good agreement with experiment (Figure 4.1). However, as I began to write up a paper about all three dimers, I realized that,

according to the labels in their original paper, I had matched simulated AC spectra with experimental BC data and vice versa. It turns out that the data I was sent by the experimentalists, in addition to being unlabeled, had the absorption data columns accidentally switched.

I immediately reexamined all of my calculations and ensured that they were all correctly labeled and consistent. I also examined the dipole fitting that we performed, but found that no possible dipole orientation exists that allows my simulated AC spectra to match their AC data or my simulated BC spectra to match their BC data. Furthermore, the peak splitting present in the experimental "AC" spectra perfectly matches our BC eigenenergy difference, and the peak splitting present in the experimental "BC" spectra perfectly matches our AC eigenenergy difference. Given the consistency of our site energies and our linear spectra, we find it incredibly unlikely that we coincidentally match AC data with *ab initio* calculations on the BC structure and vice versa, and thus are forced to conclude that experimental samples or data must have been switched somewhere within the research process. The experimentalists, however, remain "fairly confident" that their data has not been switched.

Unfortunately, this is not a simple matter of two lines being mislabeled and all the rest of the analysis being sound. The identity and labeling of the AC and BC dimers is critical to their weak coupling assumption which allows them to assign the frequencies of electronic coherence that their analysis is based on. Rather than publishing a paper calling into question both the assumption of weak coupling and their experimental procedures, we decided to write up a paper only on the AB dimer, for which we reproduce experimental spectra thanks to our strong coupling, thereby only having to dispute their coupling assumption and not their labeling.

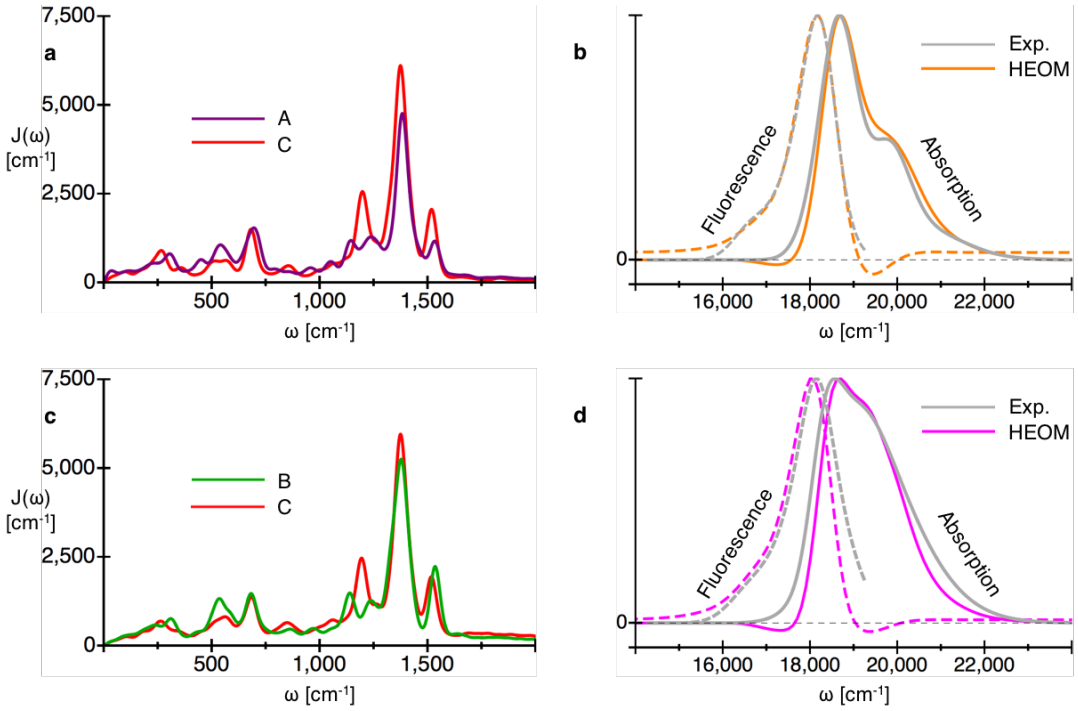

Figure 4.1: Spectral densities and linear spectra of AC and BC dimers. **a**, AC CIS spectral densities for the A dye (purple) and for the C dye (red). **b**, A comparison of simulated (orange) and experimental (gray) linear spectral, where absorption is shown with solid lines and fluorescence is shown with dashed lines. Simulated spectra include 270 cm^{-1} of inhomogeneous broadening, a 2040 cm^{-1} constant shift, and a 45 degree rotation of one transition dipole vector, but are otherwise entirely *ab initio*. **c**, BC CIS spectral densities for the B dye (green) and for the C dye (red). **d**, A comparison of simulated (magenta) and experimental (gray) linear spectral, where absorption is shown with solid lines and fluorescence is shown with dashed lines. Simulated spectra include 250 cm^{-1} of inhomogeneous broadening, a 2120 cm^{-1} constant shift, and a 90 degree rotation of one transition dipole vector, but are otherwise entirely *ab initio*.

4.4 Population and Coherence Dynamics

Equivalent population and coherence analysis as performed for the AB dimer are shown in Figure 4.2 (AC) and Figure 4.3 (BC). Once again, short time electronic coherence gives way to vibrationally driven coherence after about 100 fs. We note that the frequency of electronic coherence observed in the windowed FFT is shifted slightly off of the pure eigenenergy differences for both AC and BC dimers, likely due to coupling to strong vibrations within 100 cm^{-1} of the eigenenergy differences. In contrast, the AB

dimer eigenenergy difference happened to fall right in the area of the spectral densities without any strong peaks.

4.5 2D Spectroscopy

As with the AB dimer, we ran a 1 ps trajectory of 2D spectra simulations for both the AC and BC dimers. Once again, the computational complexity of 2D simulations prevents us from quantitatively comparing our results with experimental power spectra. However, once again, reexamination of experimental power spectra of both the dimers and the mixture of monomers reveals that our derived frequencies of electronic coherence allow for a more convincing assignment for both the AC dimer (Figure 4.9) and the BC dimer (Figure 4.15).

4.6 Supplementary Information

4.6.1 Coarse Graining Spectral Densities

Spectral density parameters are given in Table 4.3-4.6.

4.6.2 Linear Spectra, Inhomogeneous Broadening and Transition Dipole Vectors

AC and BC dimers required larger modifications to their transition dipole vectors in order to match experimental spectra than were necessary for the AB dimer. Transition dipole vectors are given in Table 4.7 and Table 4.8.

SiteA, Class1			**SiteC, Class1**		
$\lambda(cm^{-1})$	$\gamma(cm^{-1})$	$\Omega(cm^{-1})$	$\lambda(cm^{-1})$	$\gamma(cm^{-1})$	$\Omega(cm^{-1})$
252.0	26.0	18.0	168.0	60.0	0.0
55.0	43.0	106.0	32.0	25.0	91.0
110.0	65.0	219.0	28.0	35.0	175.0
51.0	30.0	304.0	18.0	30.0	223.0
24.0	30.0	446.0	88.0	33.0	262.0
62.0	40.0	539.0	13.0	23.0	358.0
12.0	50.0	630.0	32.3	40.0	507.0
69.5	35.0	692.0	20.0	33.0	567.0
2.0	20.0	800.0	48.0	24.0	680.0
4.0	35.0	860.0	14.0	35.0	852.0
7.0	28.0	956.0	2.2	30.0	995.0
8.0	25.0	1048.0	12.0	50.0	1060.0
24.0	33.0	1141.0	65.0	35.0	1195.0
34.0	45.0	1233.0	154.0	36.0	1373.0
118.0	34.0	1382.0	22.0	19.0	1520.0
12.0	20.0	1534.0			

SiteA, Class2			**SiteC, Class2**		
$\lambda(cm^{-1})$	$\gamma(cm^{-1})$	$\Omega(cm^{-1})$	$\lambda(cm^{-1})$	$\gamma(cm^{-1})$	$\Omega(cm^{-1})$
315.7	40.0	0.0	240.0	100.0	20.0
110.0	65.0	219.0	120.0	45.0	255.0
51.0	30.0	304.0	43.5	45.0	535.0
24.0	30.0	446.0	48.0	24.0	680.0
64.2	40.0	539.0	12.0	35.0	852.0
76.2	37.0	692.0	12.0	50.0	1060.0
7.4	28.0	956.0	65.0	35.0	1195.0
8.0	25.0	1048.0	154.0	36.0	1373.0
24.0	33.0	1141.0	22.0	19.0	1520.0
34.0	45.0	1233.0			
118.0	34.0	1382.0			
12.0	20.0	1534.0			

Table 4.3: AC dimer Class 1 and Class 2 CIS spectral density parameters.

SiteA, Class2.5 CIS			**SiteC, Class2.5 CIS**		
$\lambda(cm^{-1})$	$\gamma(cm^{-1})$	$\Omega(cm^{-1})$	$\lambda(cm^{-1})$	$\gamma(cm^{-1})$	$\Omega(cm^{-1})$
304.5	40.0	0.0	240.0	100.0	20.0
180.0	80.0	260.0	120.0	45.0	255.0
160.0	100.0	600.0	104.5	120.0	630.0
5.6	28.0	956.0	11.0	50.0	1060.0
7.4	25.0	1048.0	65.0	35.0	1195.0
24.0	33.0	1141.0	154.0	36.0	1373.0
33.0	45.0	1233.0	22.0	19.0	1520.0
118.0	34.0	1382.0			
12.0	20.0	1534.0			

SiteA, Class3 CIS			**SiteC, Class3 CIS**		
$\lambda(cm^{-1})$	$\gamma(cm^{-1})$	$\Omega(cm^{-1})$	$\lambda(cm^{-1})$	$\gamma(cm^{-1})$	$\Omega(cm^{-1})$
304.5	40.0	0.0	240.0	100.0	20.0
180.0	80.0	260.0	120.0	45.0	255.0
160.0	100.0	600.0	110.5	120.0	630.0
200.0	65.0	1373.0	246.0	60.0	1369.0

SiteA, Class3 SOS − CIS(D)			**SiteC, Class3 SOS − CIS(D)**		
$\lambda(cm^{-1})$	$\gamma(cm^{-1})$	$\Omega(cm^{-1})$	$\lambda(cm^{-1})$	$\gamma(cm^{-1})$	$\Omega(cm^{-1})$
170.0	40.0	0.0	260.0	100.0	20.0
260.0	90.0	250.0	180.0	50.0	255.0
206.0	110.0	550.0	190.0	150.0	610.0
480.0	85.0	1365.0	545.2	80.0	1350.0

Table 4.4: AC dimer Class 2.5 and Class 3 spectral density parameters.

SiteB, Class1			**SiteC, Class1**		
$\lambda(cm^{-1})$	$\gamma(cm^{-1})$	$\Omega(cm^{-1})$	$\lambda(cm^{-1})$	$\gamma(cm^{-1})$	$\Omega(cm^{-1})$
102.0	50.0	0.0	54.0	25.0	0.0
50.0	37.0	94.0	162.0	79.0	90.0
39.0	35.0	180.0	9.6	22.0	184.0
92.7	44.0	259.0	76.0	50.0	230.0
18.0	40.0	345.0	45.0	28.0	309.0
10.0	32.0	455.0	6.0	28.0	430.0
33.0	43.0	519.0	80.0	38.0	530.0
28.0	35.0	567.0	17.0	30.0	583.0
56.0	32.0	680.5	56.0	30.0	682.0
30.0	52.0	848.0	2.6	33.0	765.0
7.6	40.0	990.0	16.6	50.0	860.0
20.0	50.0	1060.0	9.0	33.0	970.0
65.0	35.0	1192.0	4.4	30.0	1050.0
2.0	20.0	1265.0	34.0	29.0	1133.0
154.0	36.0	1373.0	26.0	36.0	1235.0
24.0	22.0	1520.0	134.9	36.0	1373.0
			30.0	22.0	1535.0

SiteB, Class2			**SiteC, Class2**		
$\lambda(cm^{-1})$	$\gamma(cm^{-1})$	$\Omega(cm^{-1})$	$\lambda(cm^{-1})$	$\gamma(cm^{-1})$	$\Omega(cm^{-1})$
264.3	150.0	50.0	275.2	130.0	50.0
68.0	40.0	260.0	60.0	50.0	230.0
33.0	43.0	515.0	40.0	28.0	309.0
25.0	35.0	567.0	76.0	38.0	530.0
54.0	32.0	680.5	16.0	30.0	583.0
27.0	52.0	848.0	54.0	30.0	682.0
20.0	50.0	1055.0	14.0	50.0	860.0
65.0	35.0	1192.0	9.0	33.0	970.0
152.0	36.0	1373.0	32.0	29.0	1133.0
23.0	22.0	1520.0	24.0	36.0	1235.0
			134.9	36.0	1373.0
			28.0	22.0	1535.0

Table 4.5: BC dimer Class 1 and Class 2 CIS spectral density parameters.

SiteB, Class2.5 CIS			**SiteC, Class2.5 CIS**		
$\lambda(cm^{-1})$	$\gamma(cm^{-1})$	$\Omega(cm^{-1})$	$\lambda(cm^{-1})$	$\gamma(cm^{-1})$	$\Omega(cm^{-1})$
240.0	150.0	50.0	285.1	150.0	50.0
54.0	35.0	260.0	79.1	50.0	270.0
180.0	150.0	640.0	180.0	80.0	600.0
17.3	50.0	1055.0	32.0	29.0	1133.0
65.0	35.0	1192.0	24.0	36.0	1235.0
152.0	36.0	1373.0	134.9	36.0	1373.0
23.0	22.0	1520.0	28.0	22.0	1535.0
SiteB, Class3 CIS			**SiteC, Class3 CIS**		
$\lambda(cm^{-1})$	$\gamma(cm^{-1})$	$\Omega(cm^{-1})$	$\lambda(cm^{-1})$	$\gamma(cm^{-1})$	$\Omega(cm^{-1})$
240.0	150.0	50.0	280.0	150.0	50.0
54.0	35.0	260.0	79.1	50.0	270.0
200.0	200.0	640.0	180.0	80.0	600.0
237.3	63.0	1372.0	224.0	65.0	1370.0
SiteB, Class3 SOS − CIS(D)			**SiteC, Class3 SOS − CIS(D)**		
$\lambda(cm^{-1})$	$\gamma(cm^{-1})$	$\Omega(cm^{-1})$	$\lambda(cm^{-1})$	$\gamma(cm^{-1})$	$\Omega(cm^{-1})$
240.0	150.0	100.0	240.0	150.0	100.0
54.0	25.0	260.0	120.0	55.0	280.0
153.0	150.0	610.0	140.0	60.0	540.0
451.8	77.0	1357.0	480.0	65.0	1345.0

Table 4.6: BC dimer Class 2.5 and Class 3 spectral density parameters.

	$\mathbf{L_x}$	$\mathbf{L_y}$	$\mathbf{L_z}$
Site A	3.03666	0.207464	-2.10254
Site C	2.26202	0.177165	-1.57265
Site C tweaked	1.25829	2.00585.	-1.41938

Table 4.7: AC transition dipole vectors given in atomic units.

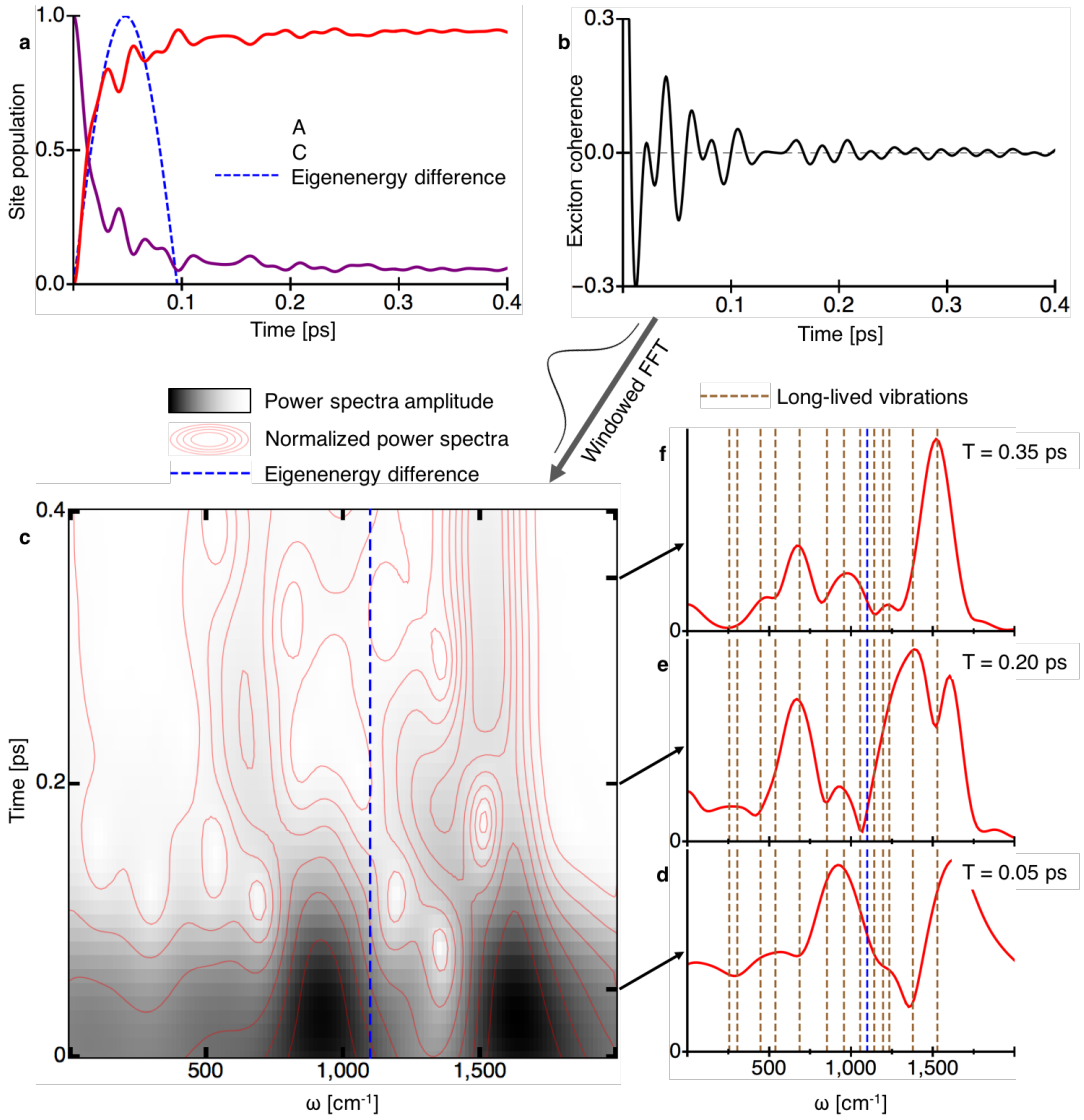

Figure 4.2: Population and coherence dynamics of the AC dimer. **a**, Transport dynamics simulated with HEOM and Class 2 spectral densities with the excitation initially locaized on the high-energy A dye (purple) and rapidly migrating to the C dye (Red) with an initial rise corresponding precisely to the frequency of electronic coherence (dashed blue). **b**, Direct propagation of exciton coherences. **c**, Windowed Fourier transform of the coherence dynamics, where a grey scale denotes absolute power spectra amplitude, red contour lines denote normalized power spectra amplitude to better reveal long-time vibrational effects, and the frequency of electronic coherence is shown in dashed blue. Note that the dark feature in the bottom middle of the panel denotes electronic coherence. **d**, Windowed FFT time slice at 0.05 ps, where strong high-frequency vibrations from both A and B spectral densities are shown in dashed brown. **e**, Windowed FFT time slice at 0.2 ps. **f**, Windowed FFT time slice at 0.35 ps.

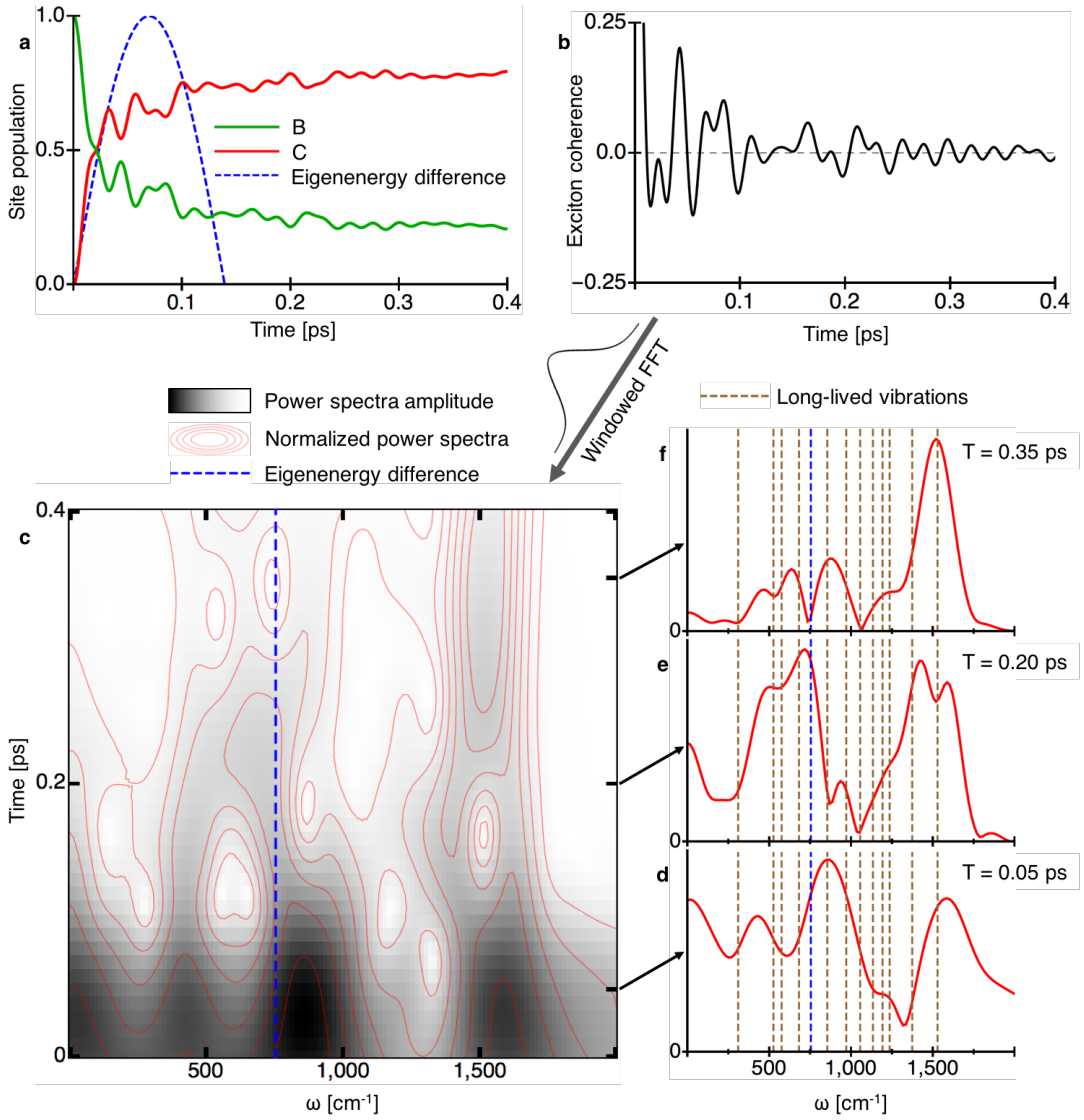

Figure 4.3: Population and coherence dynamics of the BC dimer. **a**, Transport dynamics simulated with HEOM and Class 2 spectral densities with the excitation initially locaized on the high-energy B dye (green) and rapidly migrating to the C dye (red) with an initial rise corresponding precisely to the frequency of electronic coherence (dashed blue). **b**, Direct propagation of exciton coherences. **c**, Windowed Fourier transform of the coherence dynamics, where a grey scale denotes absolute power spectra amplitude, red contour lines denote normalized power spectra amplitude to better reveal long-time vibrational effects, and the frequency of electronic coherence is shown in dashed blue. Note that the dark feature in the bottom middle of the panel denotes electronic coherence. **d**, Windowed FFT time slice at 0.05 ps, where strong high-frequency vibrations from both A and B spectral densities are shown in dashed brown. **e**, Windowed FFT time slice at 0.2 ps. **f**, Windowed FFT time slice at 0.35 ps.

	$\mathbf{L_x}$	$\mathbf{L_y}$	$\mathbf{L_z}$
Site B	3.475555	-0.83507	-0.198105
Site B tweaked	0.145058	0.977767	-3.44078
Site C	2.73403	-0.67989	-0.0779419

Table 4.8: BC transition dipole vectors given in atomic units.

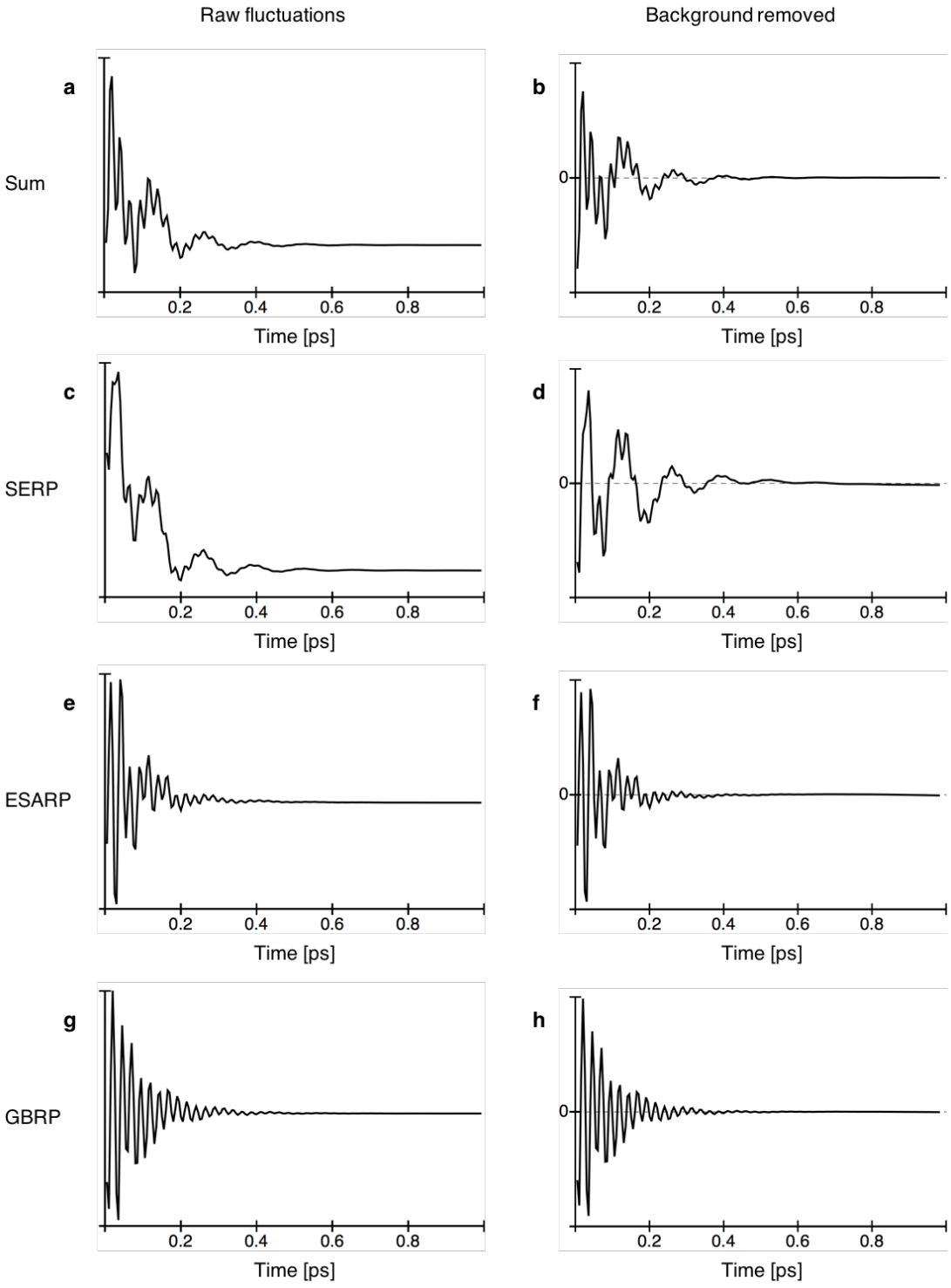

Figure 4.4: AC dimer off-diagonal 2D oscillations of each pathway. Oscillations of all pathways summed together shown with (**a**) and without (**b**) background. SERP pathway oscillations with (**c**) and without (**d**) background. ESARP pathway oscillatioins with (**e**) and without (**f**) background. GBRP pathway oscillations with (**g**) and without (**h**) background.

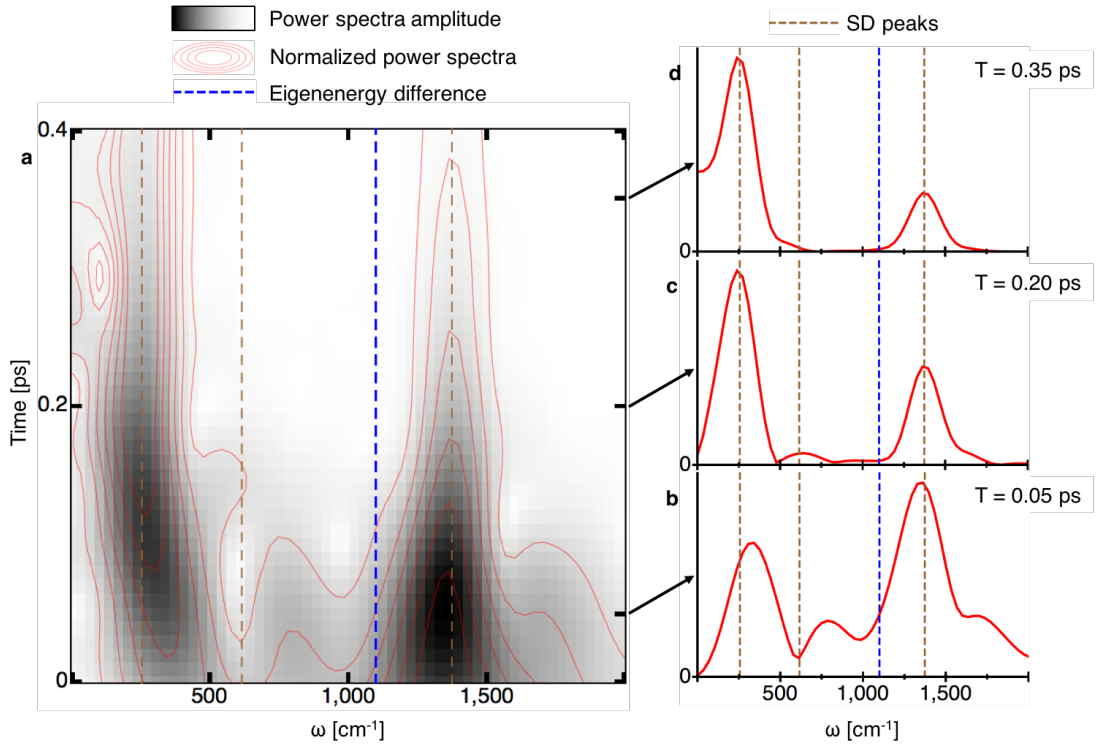

Figure 4.5: AC dimer windowed FFT of summed oscillations. a, Windowed Fourier transform of off-diagonal oscillations of all summed pathways calculated with Class 3 SDs, where a grey scale denotes absolute power spectra amplitude, red contour lines denote normalized power spectra amplitude to better reveal long-time vibrational effects, the frequency of electronic coherence is shown in dashed blue, and SD peak positions are shown in dashed brown. **b**, Windowed FFT time slice at 0.05 ps. **c**, Windowed FFT time slice at 0.2 ps. **d**, Windowed FFT time slice at 0.35 ps.

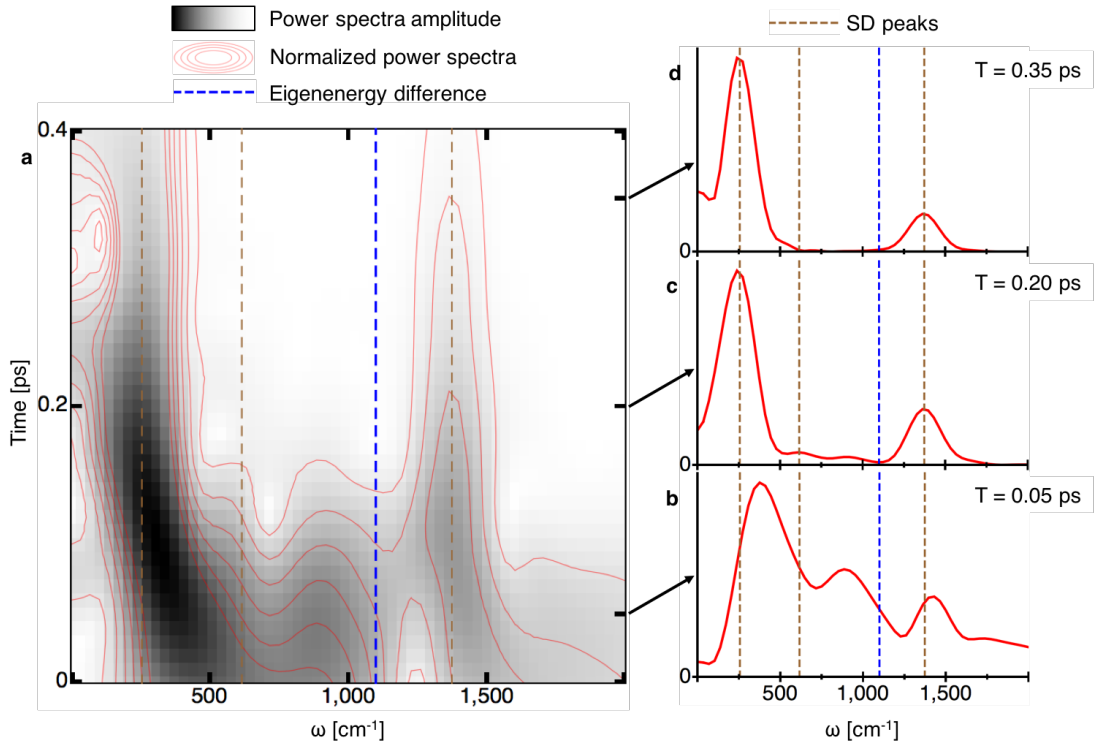

Figure 4.6: AC dimer windowed FFT of SERP oscillations. a, Windowed Fourier transform of off-diagonal oscillations of the SERP pathway calculated with Class 3 SDs, where a grey scale denotes absolute power spectra amplitude, red contour lines denote normalized power spectra amplitude to better reveal long-time vibrational effects, the frequency of electronic coherence is shown in dashed blue, and SD peak positions are shown in dashed brown. **b**, Windowed FFT time slice at 0.05 ps. **c**, Windowed FFT time slice at 0.2 ps. **d**, Windowed FFT time slice at 0.35 ps.

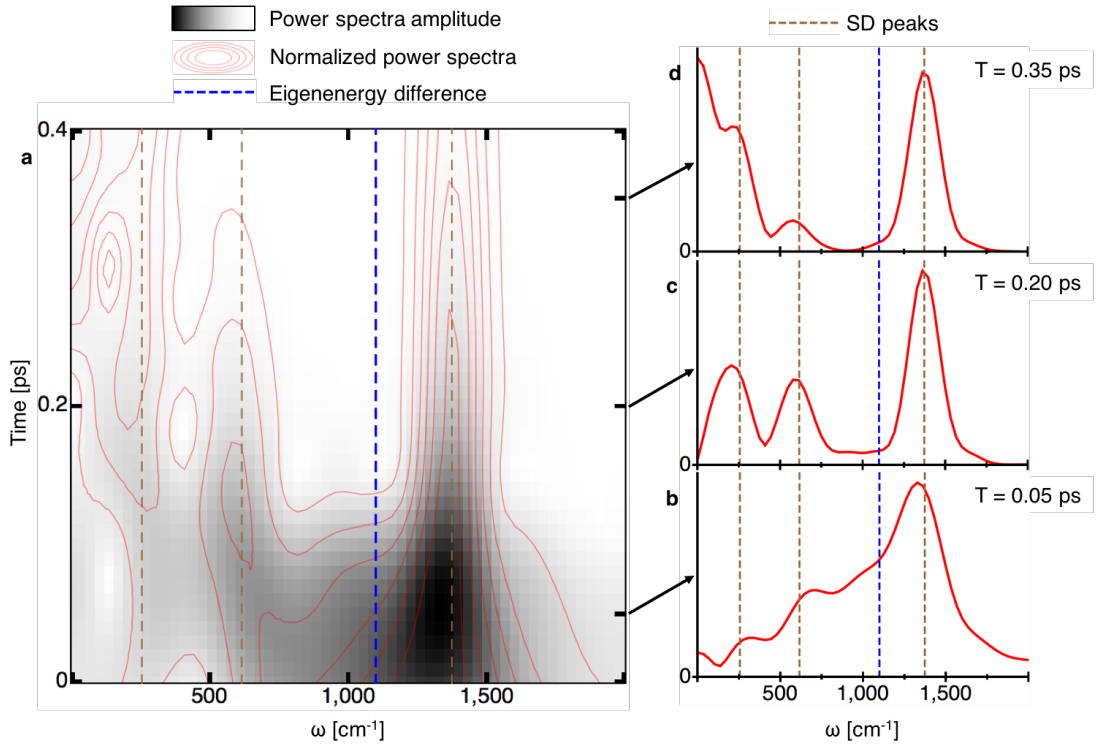

Figure 4.7: AC dimer windowed FFT of ESARP oscillations. a, Windowed Fourier transform of off-diagonal oscillations of the ESARP pathway calculated with Class 3 SDs, where a grey scale denotes absolute power spectra amplitude, red contour lines denote normalized power spectra amplitude to better reveal long-time vibrational effects, the frequency of electronic coherence is shown in dashed blue, and SD peak positions are shown in dashed brown. **b**, Windowed FFT time slice at 0.05 ps. **c**, Windowed FFT time slice at 0.2 ps. **d**, Windowed FFT time slice at 0.35 ps.

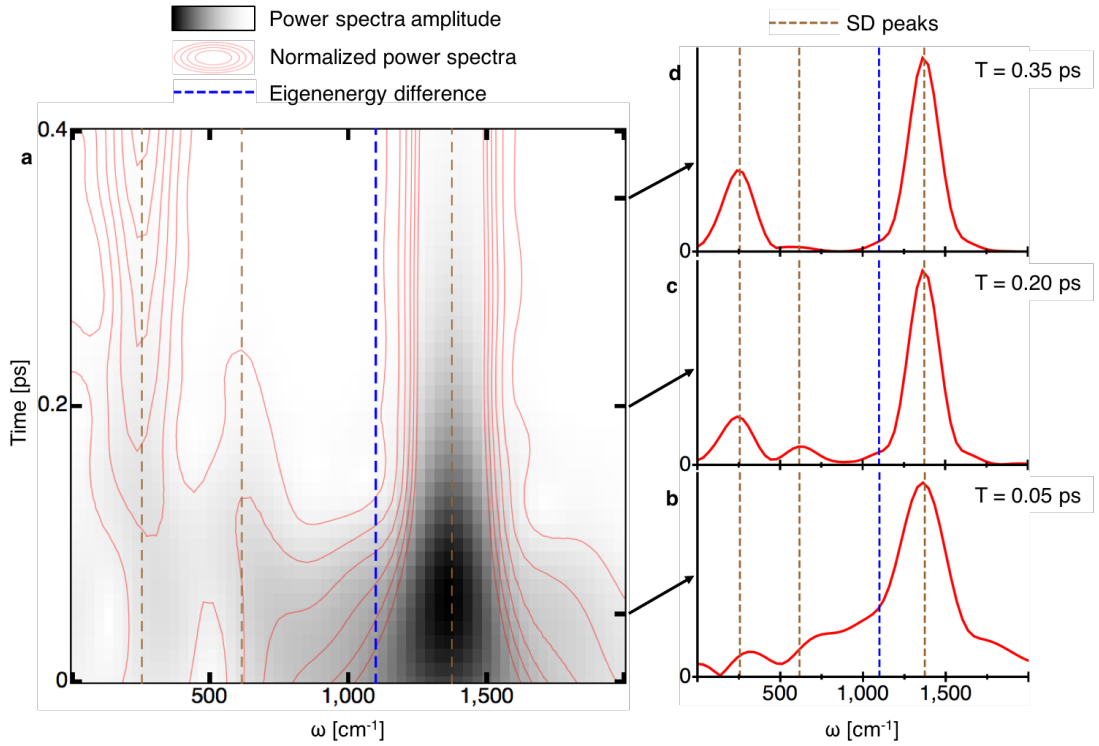

Figure 4.8: AC dimer windowed FFT of GBRP oscillations. a, Windowed Fourier transform of off-diagonal oscillations of the GBRP pathway calculated with Class 3 SDs, where a grey scale denotes absolute power spectra amplitude, red contour lines denote normalized power spectra amplitude to better reveal long-time vibrational effects, the frequency of electronic coherence is shown in dashed blue, and SD peak positions are shown in dashed brown. **b**, Windowed FFT time slice at 0.05 ps. **c**, Windowed FFT time slice at 0.2 ps. **d**, Windowed FFT time slice at 0.35 ps.

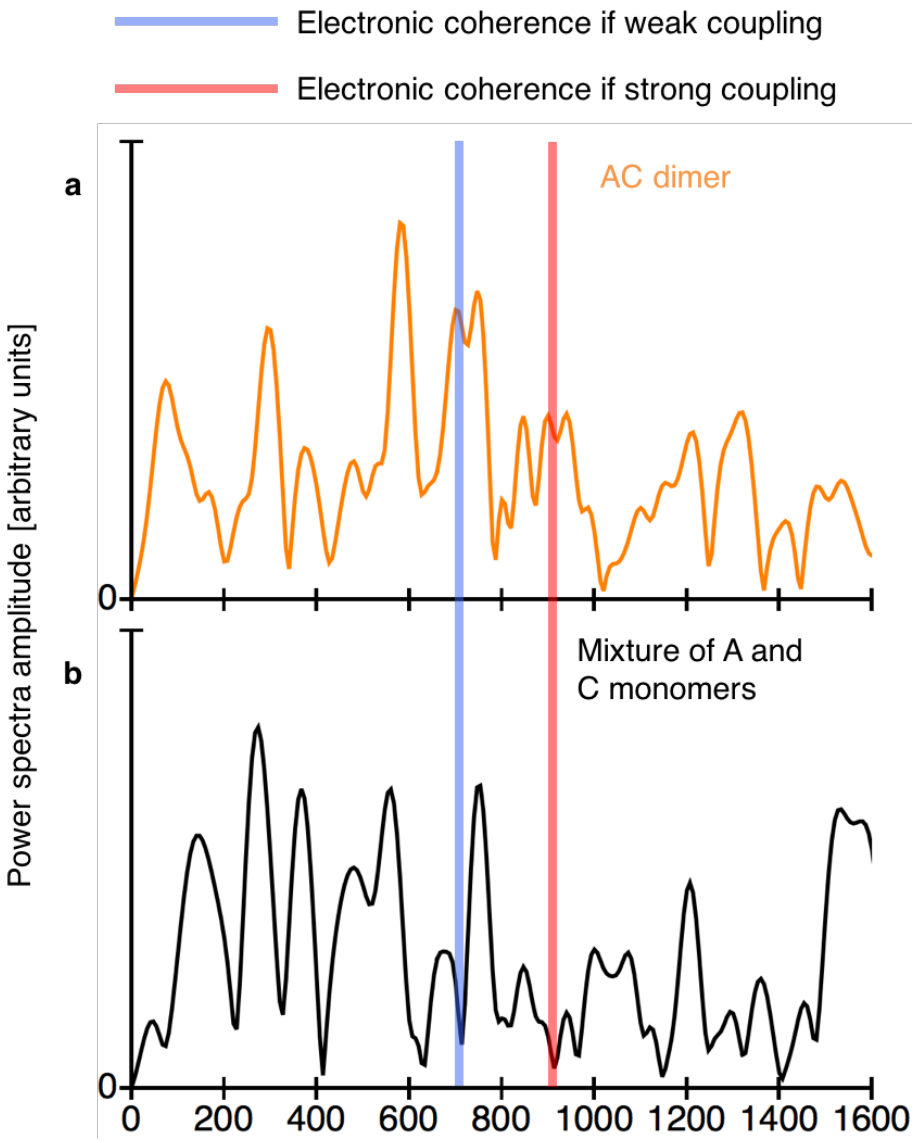

Figure 4.9: Experimental off-diagonal 2D oscillation power spectra of AC dimer and of a mixture of A and C monomers. a, Dimer power spectrum. **b**, Mixture of monomers power spectrum. The site energy difference, aka the frequency of electronic coherence if the dimers are weakly coupled, is shown in light blue while our eigenenergy difference, aka the frequency of electronic coherence if the dimers are strongly coupled, is shown in light red.

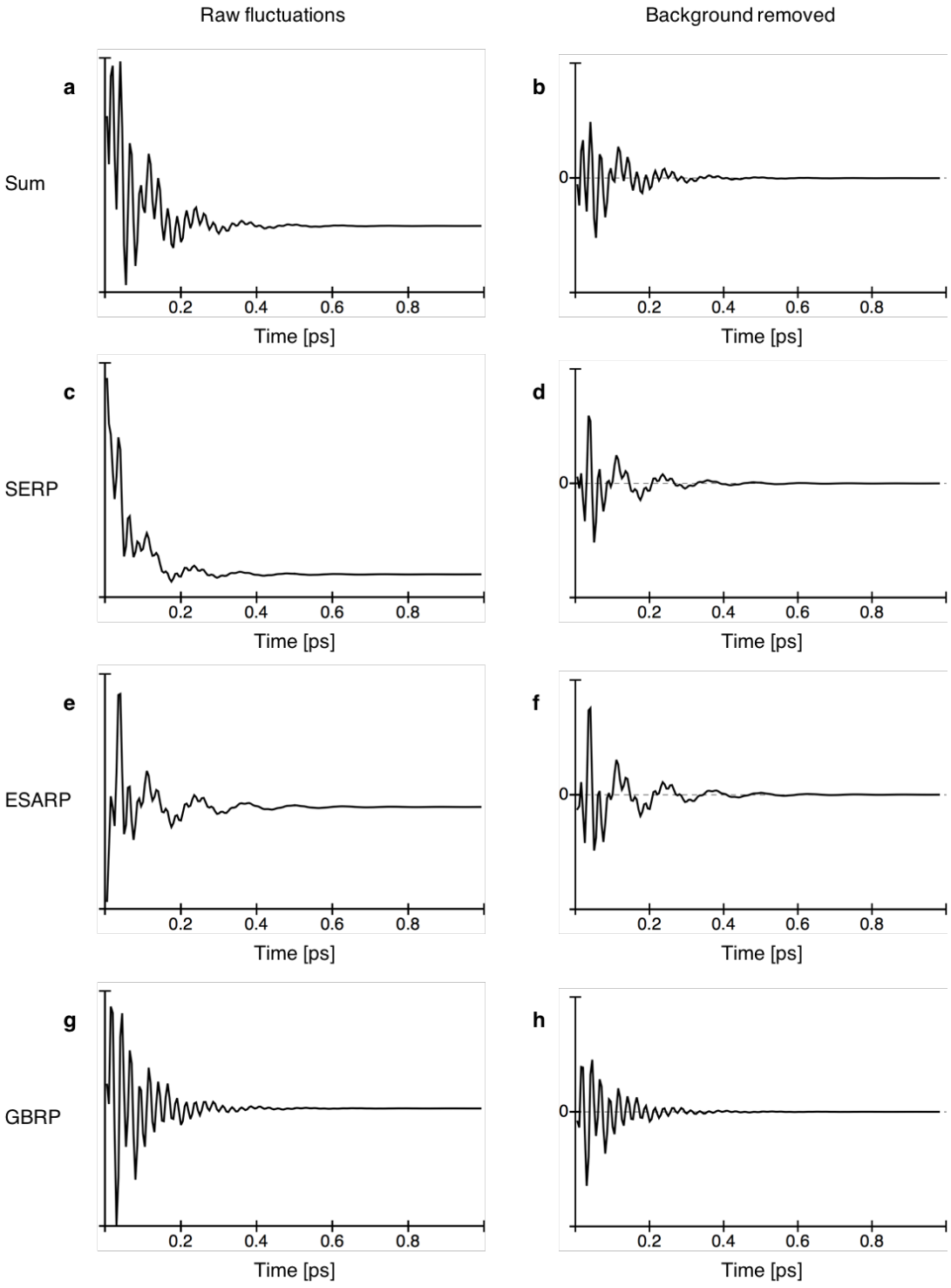

Figure 4.10: BC dimer off-diagonal 2D oscillations of each pathway. Oscillations of all pathways summed together shown with (**a**) and without (**b**) background. SERP pathway oscillations with (**c**) and without (**d**) background. ESARP pathway oscillatioins with (**e**) and without (**f**) background. GBRP pathway oscillations with (**g**) and without (**h**) background.

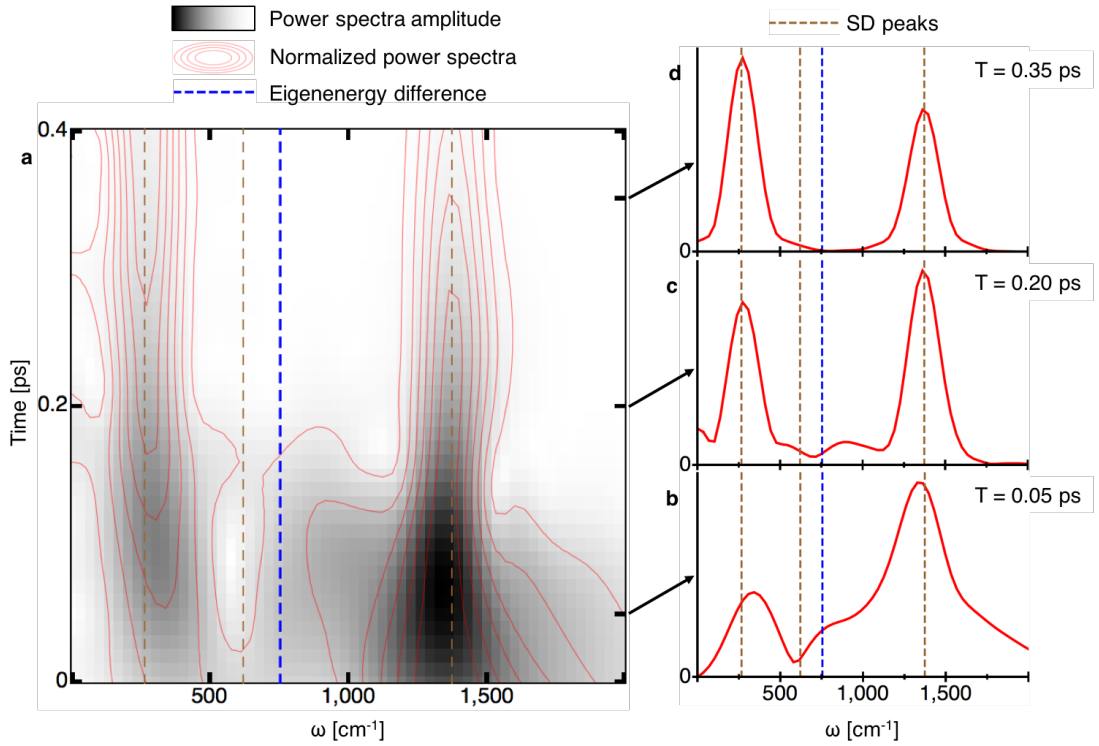

Figure 4.11: BC dimer windowed FFT of summed oscillations. a, Windowed Fourier transform of off-diagonal oscillations of all summed pathways calculated with Class 3 SDs, where a grey scale denotes absolute power spectra amplitude, red contour lines denote normalized power spectra amplitude to better reveal long-time vibrational effects, the frequency of electronic coherence is shown in dashed blue, and SD peak positions are shown in dashed brown. **b**, Windowed FFT time slice at 0.05 ps. **c**, Windowed FFT time slice at 0.2 ps. **d**, Windowed FFT time slice at 0.35 ps.

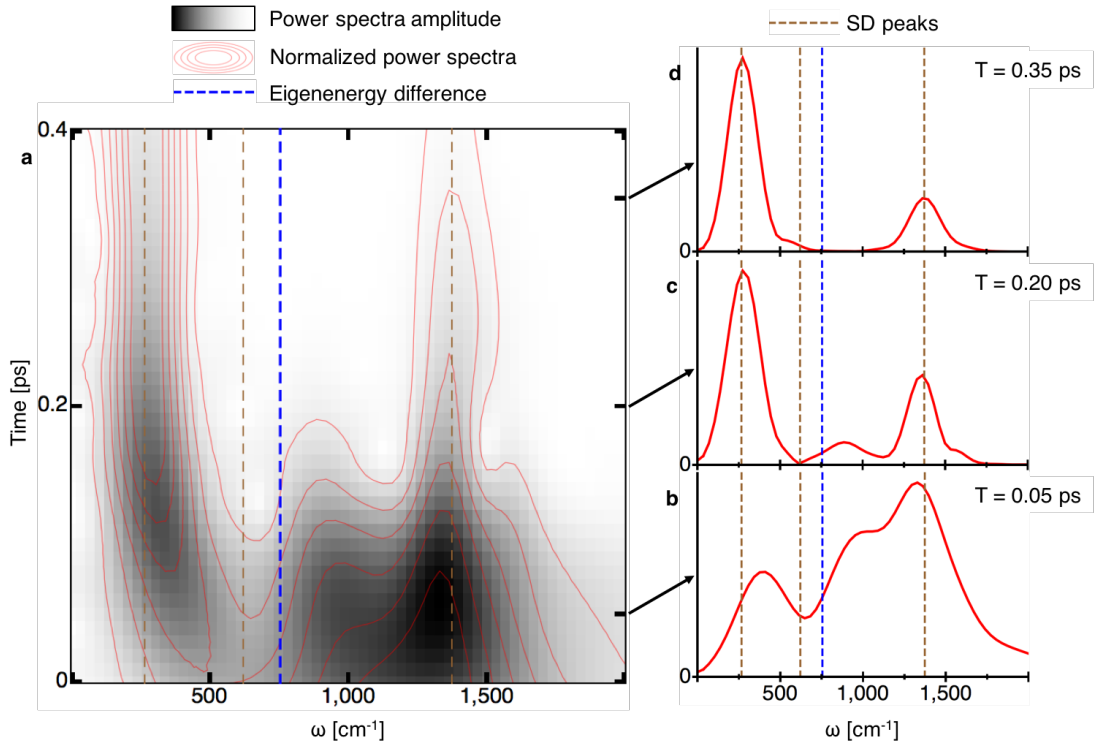

Figure 4.12: BC dimer windowed FFT of SERP oscillations. a, Windowed Fourier transform of off-diagonal oscillations of the SERP pathway calculated with Class 3 SDs, where a grey scale denotes absolute power spectra amplitude, red contour lines denote normalized power spectra amplitude to better reveal long-time vibrational effects, the frequency of electronic coherence is shown in dashed blue, and SD peak positions are shown in dashed brown. **b**, Windowed FFT time slice at 0.05 ps. **c**, Windowed FFT time slice at 0.2 ps. **d**, Windowed FFT time slice at 0.35 ps.

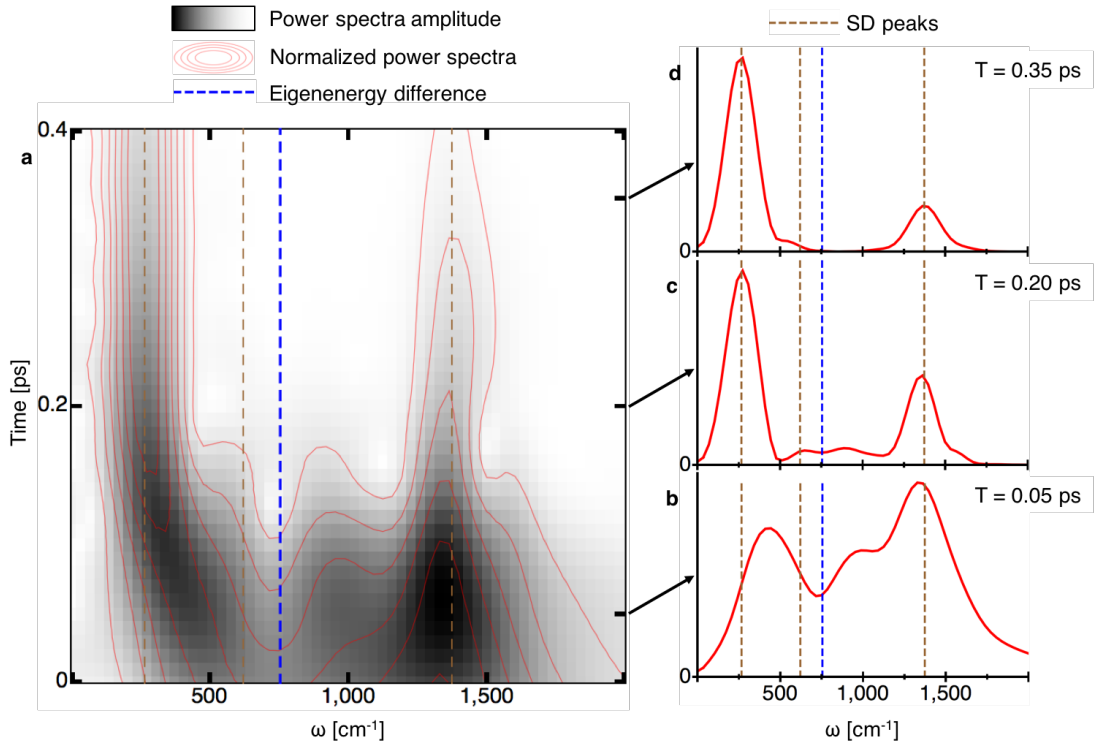

Figure 4.13: BC dimer windowed FFT of ESARP oscillations. a, Windowed Fourier transform of off-diagonal oscillations of the ESARP pathway calculated with Class 3 SDs, where a grey scale denotes absolute power spectra amplitude, red contour lines denote normalized power spectra amplitude to better reveal long-time vibrational effects, the frequency of electronic coherence is shown in dashed blue, and SD peak positions are shown in dashed brown. **b**, Windowed FFT time slice at 0.05 ps. **c**, Windowed FFT time slice at 0.2 ps. **d**, Windowed FFT time slice at 0.35 ps.

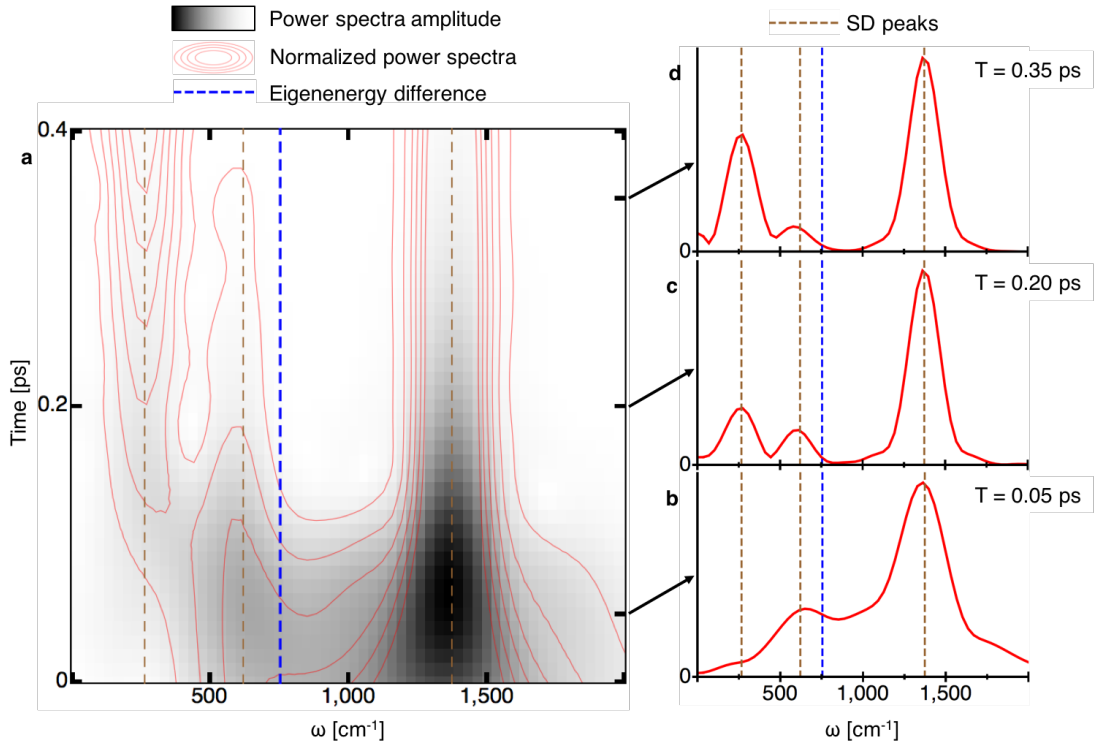

Figure 4.14: BC dimer windowed FFT of GBRP oscillations. a, Windowed Fourier transform of off-diagonal oscillations of the GBRP pathway calculated with Class 3 SDs, where a grey scale denotes absolute power spectra amplitude, red contour lines denote normalized power spectra amplitude to better reveal long-time vibrational effects, the frequency of electronic coherence is shown in dashed blue, and SD peak positions are shown in dashed brown. **b**, Windowed FFT time slice at 0.05 ps. **c**, Windowed FFT time slice at 0.2 ps. **d**, Windowed FFT time slice at 0.35 ps.

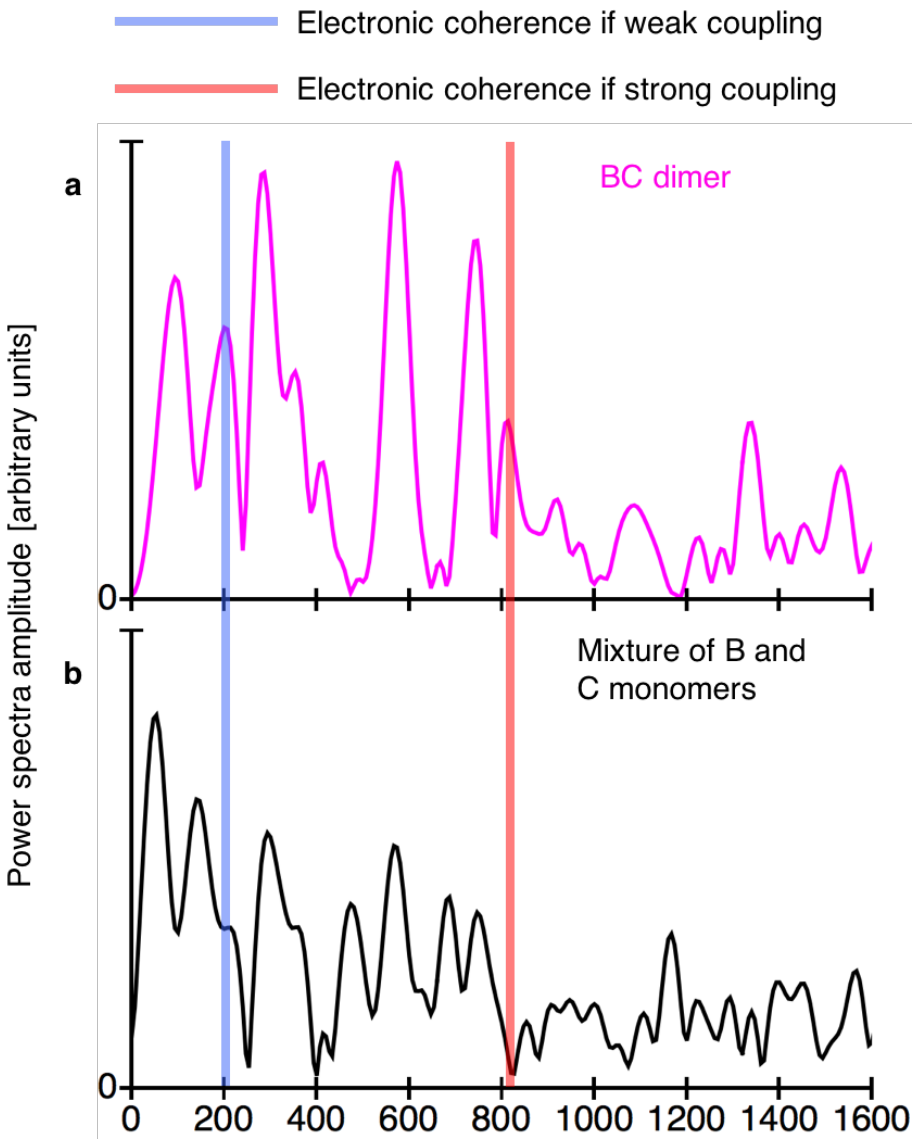

Figure 4.15: Experimental off-diagonal 2D oscillation power spectra of BC dimer and of a mixture of A and C monomers. a, Dimer power spectrum. **b**, Mixture of monomers power spectrum. The site energy difference, aka the frequency of electronic coherence if the dimers are weakly coupled, is shown in light blue while our eigenenergy difference, aka the frequency of electronic coherence if the dimers are strongly coupled, is shown in light red.

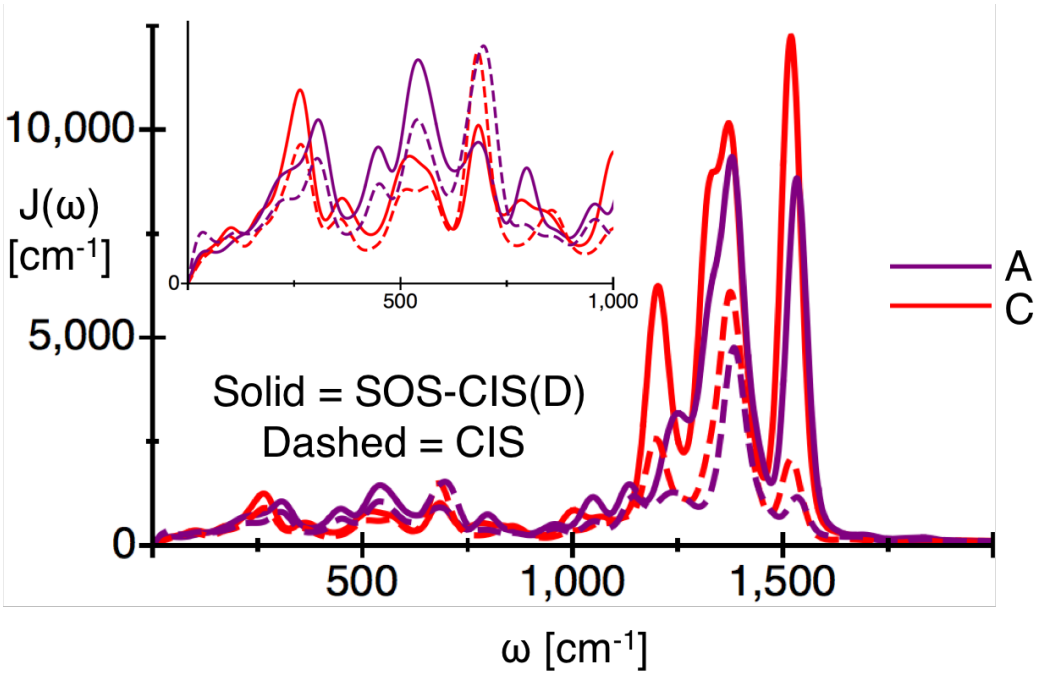

Figure 4.16: Comparing AC dimer CIS and SOS-CIS(D) spectral densities. A dye SDs are shown in purple and C dye SDs are shown in red while simultaneously SOS-CIS(D) SDs are depicted with solid lines and CIS SDs are depicted with dashed lines.

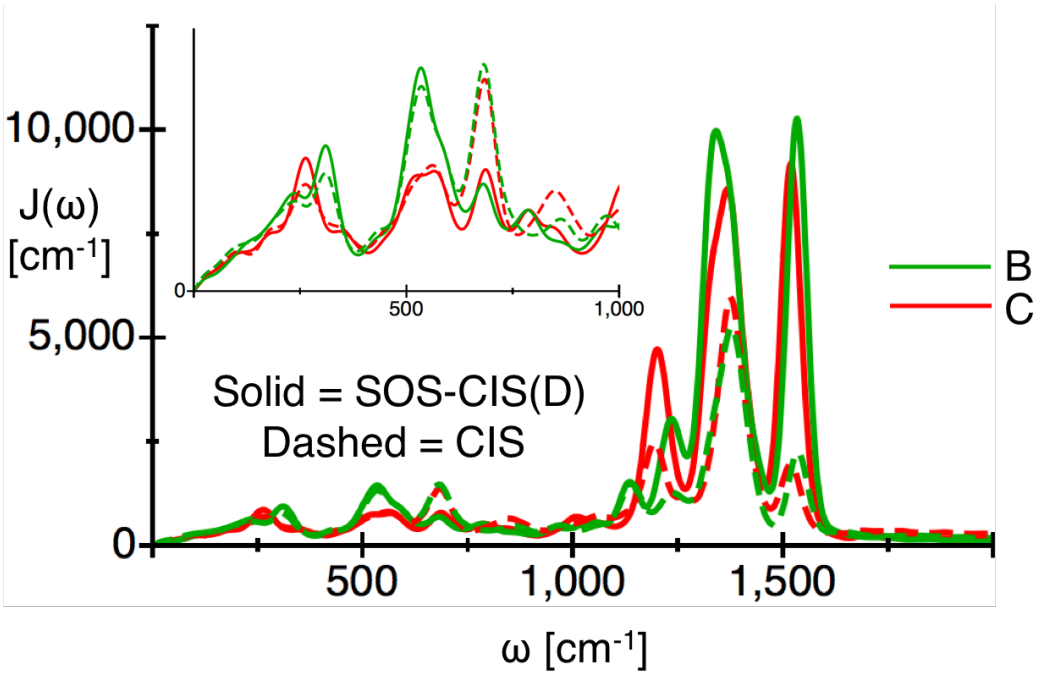

Figure 4.17: Comparing BC dimer CIS and SOS-CIS(D) spectral densities. B dye SDs are shown in red and C dye SDs are shown in green while simultaneously SOS-CIS(D) SDs are depicted with solid lines and CIS SDs are depicted with dashed lines.

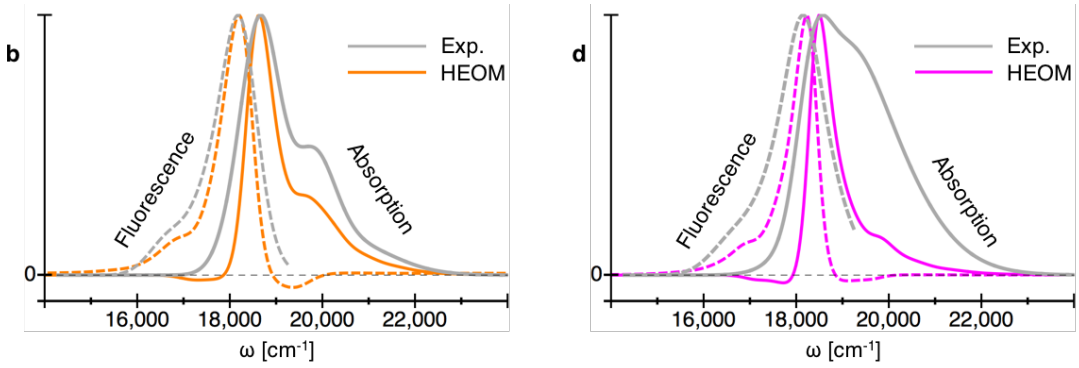

Figure 4.18: AC and BC absorption and fluorescence in the absence of inhomogeneous broadening or modifications to the transition dipole moments. AC dimer (**a**) and BC dimer (**b**) absorption (solid) and fluorescence (dashed) calculated with HEOM and Class 3 spectral densities versus experimental dimer spectra.

Conclusion

I have reported investigations into the presence, type, and functional importance of coherence in two controversial systems: phycobiliprotein PC645 and synthetic fluorescein heterodimers. In both cases, I avoided ubiquitous approximations by using AIMD instead of classical MD, TDDFT and SOS-CIS(D) excited state calculations instead of semiempirical ZINDO, and numerically exact HEOM exciton dynamics instead of Redfield. I carefully analyzed the impact of specific spectral density features in order to extract mechanistic insight into the importance of environmental vibrations to transport, coherence, and both linear and non-linear spectra.

One area of potential future study that I did not have time to explore is to isolate the additional physics captured by more sophisticated methods. While it is straightforward to compare HEOM and Redfield dynamics given a Hamiltonian and spectral densities, it is significantly more time- and resource-intensive to determine how spectral densities obtained from AIMD differ from those obtained from MD, or how an energy-gap trajectory calculated with TDDFT differs from one obtained with ZINDO. While the unprecedented spectroscopic agreement that I found and the level of mechanistic detail that I was able to resolve could be due to the high-quality methods I employed, one cannot be sure without a direct comparison. Unfortunately, this type of fundamental science is time-consuming and rarely appreciated.

Another critical future direction is to more thoroughly investigate the regimes of vibronic transport in a model vibronic dimer. While the vibronic dimer investigation included in the PC645 chapter was crucial for solidifying our mechanistic assignment, it was merely the beginning of a more comprehensive effort. Our goal is to clarify the regimes of vibronic transport, understand the physical mechanisms at play in each, and identify where commonly employed approximate methods can be trusted. Such a

fundamental investigation is particularly important given the recent explosion of interest in vibronic coherence and vibronically enhanced transport.

Regarding the sophisticated spectroscopy that defines much of the field of excitonics, additional work must be done to develop more reliable experimental techniques for probing energy transfer dynamics. 2D echo spectroscopy has thus far been the method of choice, but its greatest strength is also its biggest weakness. Simultaneously probing all possible excitation pathways coupled to a complex continuum of environmental vibrations makes reliable analysis almost impossible. As a result, I argue that attempts to interpret complex 2D echo spectra have yielded more confusion than understanding. Methods such as 2D fluorescence spectroscopy and full quantum process tomography resolve some of the problems inherent to 2D echo spectroscopy, but they also introduce issues of their own.

Despite the advantages inherent in theoretical descriptions of excitation energy transport, computational cost dramatically limits their application. Indeed, as I have reported here, only very small systems can be treated with reliably accurate methods, and even then it takes years of human and computational time to examine a single system. Furthermore, the vast majority of theoreticians investigating EET do not have the time or computational resources that I did, and thus employ methods and procedures that involve uncontrolled approximations that are a computational necessity. Therefore, an incredibly important area of study is the continued development of fast and efficient computational methods that remain precise and yield reliable results. This includes ensuring that the community has a better understanding of where approximate methods are reliable and where they break down. In concert, these advances would make larger and more important systems, such as the photosynthetic reaction center, computationally tractable and would also allow smaller systems to be treated en masse in screening applications.

Finally, after all of my research and experience in the field of excitonics, I am firmly convinced that long-lived oscillations observed in 2D spectra are reporting entirely on long-lived environmental vibrations. Furthermore, while spectroscopy may reveal

short-time signatures of vibronic coherence, neither electronic, vibronic, nor vibrational coherence play a functional role in photosynthetic light-harvesting or any other biological processes. Howevever, regardless of what occurs in natural systems, excitonics research should instead focus on designing next-generation materials for light-harvesting and energy transport using either incoherent or coherent mechanisms. While striving to learn from nature is noble and worthwhile, we should not let it limit our innovation.

References

[1] S. P. Long, X.-G. Zhu, S. L. Naidu, and D. R. Ort, Plant Cell Environ. **29**, 315 (2006).

[2] D. Zigmantas, E. L. Read, T. Manal, T. Brixner, A. T. Gardiner, R. J. Cogdell, and G. R. Fleming, Proc. Natl Acad. Sci. **103**, 12672 (2006).

[3] J. Huh, S. K. Saikin, J. C. Brookes, S. Valleau, T. Fujita, and A. Aspuru-Guzik, J. Am. Chem. Soc. **136**, 2048 (2014).

[4] R. E. Fenna and B. W. Matthews, Nature **258**, 573 (1975).

[5] G. S. Engel, T. R. Calhoun, E. L. Read, T.-K. Ahn, T. Mancal, Y.-C. Cheng, R. E. Blankenship, and G. R. Fleming, Nature **446**, 782 (2007).

[6] A. Ishizaki and G. R. Fleming, J. Chem. Phys. **130**, 234111 (2009).

[7] N. Christensson, H. F. Kauffmann, T. Pullerits, and T. Mancal, J. Phys. Chem. B **116**, 7449 (2012).

[8] V. Tiwari, W. K. Peters, and D. M. Jonas, Proc. Natl Acad. Sci. **110**, 1203 (2013).

[9] F. D. Fuller, J. Pan, A. Gelzinis, V. Butkus, S. S. Senlik, D. E. Wilcox, C. F. Yocum, L. Valkunas, D. Abramavicius, and J. P. Ogilvie, Nat. Chem. **6**, 706 (2014).

[10] V. I. Novoderezhkin, E. Romero, J. Prior, and R. van Grondelle, Phys. Chem. Chem. Phys. **19**, 5195 (2017).

[11] J. C. Dean, M. Tihana, Z. S. Toa, D. G. Oblinsky, and G. D. Scholes, Chem **1**, 858 (2016).

[12] Y. Tanimura and R. Kubo, J. Phys. Soc. Jpn. **58**, 101 (1989).

[13] Y. Tanimura, J. Chem. Phys. **137**, 22A550 (2012).

[14] C. Kreisbeck, T. Kramer, and A. Aspuru-Guzik, J. Chem. Theory Comput. **10**, 4045 (2014).

[15] D. Hayes, G. B. Griffin, and G. S. Engel, Science **340**, 1431 (2013).

[16] H.-P. Breuer and F. Petruccione, *The Theory of Open Quantum Systems* (Oxford University Press, USA, 2007).

[17] N. Shenvi, J. R. Schmidt, S. T. Edwards, and J. C. Tully, Phys. Rev. A **78**, 022502 (2008).

[18] T. C. Berkelbach, M. S. Hybertsen, and D. R. Reichman, J Chem Phys **138**, 4102 (2013).

[19] T. C. Berkelbach, M. S. Hybertsen, and D. R. Reichman, J. Chem. Phys. **138**, 114103 (2013).

[20] N. Singh and P. Brumer, Faraday Discuss. **153**, 41 (2011).

[21] S. Jang, M. D. Newton, and R. J. Silbey, J. Phys. Chem. B **111**, 6807 (2007).

[22] M. Mohseni, P. Rebentrost, S. Lloyd, and A. Aspuru-Guzik, J. Chem. Phys. **129**, 174106 (2008).

[23] M. B. Plenio and S. F. Huelga, New J. Phys. **10**, 113019 (2008).

[24] P. Rebentrost, M. Mohseni, I. Kassal, S. Lloyd, and A. Aspuru-Guzik, New J. Phys. **11**, 033003 (2009).

[25] J. Cao and R. J. Silbey, J. Phys. Chem. A **113**, 13825 (2009).

[26] A. Ishizaki and G. R. Fleming, Proc. Natl. Acad. Sci. **106**, 17255 (2009).

[27] A. Ishizaki and G. R. Fleming, J. Phys. Chem. B **115**, 6227 (2011).

[28] M. Sarovar, A. Ishizaki, G. R. Fleming, and K. B. Whaley, Nature Phys. **6**, 462 (2010).

[29] D. Abramavicius and S. Mukamel, J. Chem. Phys. **133**, 064510 (2010).

[30] J. Wu, F. Liu, Y. Shen, J. Cao, and R. J. Silbey, New J. Phys. **12**, 105012 (2010).

[31] J. Moix, J. Wu, P. Huo, D. Coker, and J. Cao, J. Phys. Chem. Lett. **2**, 3045 (2011).

[32] C. Kreisbeck, T. Kramer, M. Rodríguez, and B. Hein, J. Chem. Theory Comput. **7**, 2166 (2011).

[33] N. Skochdopole and D. A. Mazziotti, J. Phys. Chem. Lett. **2**, 2989 (2011).

[34] G. Ritschel, J. Roden, W. T. Strunz, A. Aspuru-Guzik, and A. Eisfeld, J. Phys. Chem. Lett. **2**, 2912 (2011).

[35] P. Rebentrost and A. Aspuru-Guzik, J. Chem. Phys. **134**, 101103 (2011).

[36] L. A. Pachón and P. Brumer, Phys. Chem. Chem. Phys. **14**, 10094 (2012).

[37] S. M. Vlaming and R. J. Silbey, J. Chem. Phys. **136**, 055102 (2012).

[38] F. Caruso, S. K. Saikin, E. Solano, S. F. Huelga, A. Aspuru-Guzik, and M. B. Plenio, Phys. Rev. B **85**, 125424 (2012).

[39] J. Zhu, S. Kais, P. Rebentrost, and A. Aspuru-Guzik, J. Phys. Chem. B **115**, 1531 (2011).

[40] J. Roden, A. Eisfeld, W. Wolff, and W. Strunz, Phys. Rev. Lett. **103**, 058301 (2009).

[41] C. Olbrich and U. Kleinekathöfer, J. Phys. Chem. B **114**, 12427 (2010).

[42] C. Olbrich, T. L. C. Jansen, J. Liebers, M. Aghtar, J. Strümpfer, K. Schulten, J. Knoester, and U. Kleinekathöfer, J. Phys. Chem. B **115**, 8609 (2011).

[43] B. Hein, C. Kreisbeck, T. Kramer, and M. Rodríguez, New J. Phys. **14**, 023018 (2012).

[44] N. Christensson, H. F. Kauffmann, T. Pullerits, and T. Mančal, J. Phys. Chem. B **116**, 7449 (2012).

[45] A. W. Chin, J. Prior, R. Rosenbach, F. Caycedo-Soler, S. F. Huelga, and M. B. Plenio, Nature Phys. **9**, 113 (2013).

[46] C. Kreisbeck and T. Kramer, J. Phys. Chem. Lett. **3**, 2828 (2012).

[47] S. Valleau, A. Eisfeld, and A. Aspuru-Guzik, J. Chem. Phys. **137**, 224103 (2012).

[48] M. Tuckerman, *Statistical Mechanics: Theory and Molecular Simulation* (OUP Oxford, 2010).

[49] E. Runge and E. K. Gross, Phys. Rev. Lett. **52**, 997 (1984).

[50] S. Mallat, *A Wavelet Tour of Signal Processing, Third Edition: The Sparse Way*, 3rd ed. (Academic Press, 2008).

[51] W. T. Freeman, T. R. Jones, and E. C. Pasztor, IEEE Comput. Graph. Appl. **22**, 56 (2002).

[52] A. J. Patti, M. I. Sezan, and A. Murat Tekalp, IEEE Trans. Image Process. **6**, 1064 (1997).

[53] M. Elad and A. Feuer, IEEE Trans. Image Process. **6**, 1646 (1997).

[54] K. G. Puschmann and F. Kneer, Astron. Astrophysic. **436**, 373 (2005).

[55] C. W. Mccutchen, J. Opt. Soc. Am. **57**, 1190 (1967).

[56] D. Kouame and M. Ploquin, in *ISBI '09* (2009) pp. 249–252.

[57] J. Ma, IEEE Trans Instrum Meas **59**, 1600 (2010).

[58] D. L. Donoho, IEEE Trans. Inform. Theory **52**, 1289 (2006).

[59] A. Oka and L. Lampe, in *ICUWB 2009* (2009) pp. 279–284.

[60] M. A. Herman and T. Strohmer, IEEE Trans Signal Process **57**, 2275 (2009).

[61] C. Qiu, W. Lu, and N. Vaswani, in *ICASSP 2009* (2009) pp. 393–396.

[62] M. Lustig, D. Donoho, and J. M. Pauly, Magnetic Resonance in Medicine **58**, 1182 (2007).

[63] M. Nagahara, D. E. Quevedo, and J. Ostergaard, in *CDC 2012* (2012) pp. 1362–1367.

[64] T. Tuma, S. Rooney, and P. Hurley, in *ICECCS 2009* (IEEE, 2009) pp. 210–219.

[65] A. Shabani, R. L. Kosut, M. Mohseni, H. Rabitz, M. A. Broome, M. P. Almeida, A. Fedrizzi, and A. G. White, arXiv (2009), 0910.5498v2 .

[66] M. Mishali and Y. C. Eldar, IEEE J Sel Topics Signal Process **4**, 375 (2010).

[67] M. F. Duarte, M. A. Davenport, D. Takhar, J. N. Laska, T. Sun, K. F. Kelly, and R. G. Baraniuk, IEEE Signal Processing Mag **25**, 83 (2008).

[68] W. K. Coulter, C. J. Hillar, and F. T. Sommer, "Adaptive compressed sensing - a new class of self-organizing coding models for neuroscience," (2009), arXiv:0906.1202 .

[69] E. J. Candès and C. Fernandez-Granda, Comm. Pure Appl. Math. (2013).

[70] J. M. Bioucas-Dias and M. A. Figueiredo, IEEE Trans. Image Process. **16**, 2992 (2007).

[71] J. M. Bioucas-Dias and M. A. T. Figueiredo, in *ICIP 2007* (2007) pp. I–105–I – 108.

[72] S. I. E. Vulto, M. A. de Baat, R. J. W. Louwe, H. P. Permentier, T. Neef, M. Miller, H. van Amerongen, and T. J. Aartsma, J. Phys. Chem. B **102**, 9577 (1998).

[73] J. Adolphs and T. Renger, Biophys. J. **91**, 2778 (2006).

[74] M. Mohseni, A. Shabani, S. Lloyd, and H. Rabitz, arXiv (2011), 1104.4812v1 .

[75] X. Chen, J. Cao, and R. J. Silbey, J. Chem. Phys. (2013).

[76] J. Yuen-Zhou, J. J. Krich, and A. Aspuru-Guzik, J. Chem. Phys. **136**, 234501 (2012).

[77] S. Shim, P. Rebentrost, S. p. Valleau, and A. n Aspuru-Guzik, Biophys. J. **102**, 649 (2012).

[78] A. Kolli, A. Nazir, and A. Olaya-Castro, J. Chem. Phys. **135**, 154112 (2011).

[79] S. Jang, J. Chem. Phys. **135**, 034105 (2011).

[80] Y. Tanimura and R. Kubo, Journal of the Physical Society of Japan **58**, 101 (1989).

[81] C. Kreisbeck and T. Kramer, "Exciton dynamics lab for light-harvesting complexes (gpu-heom)," (2013).

[82] P. Rebentrost and A. Aspuru-Guzik, J. Chem. Phys. **134**, 101103 (2011).

[83] A. Pereverzev and E. R. Bittner, J Chem Phys **125**, 4906 (2006).

[84] C. Timm, Phys. Rev. B **83**, 115416 (2011).

[85] D. Ahn, Phys. Rev. B **50**, 8310 (1994).

[86] B. Heinz-Peter, B. Kappler, and F. Petruccione, Decoherence: Theoretical, Experimental, and Conceptual Problems , 233 (2000).

[87] A. Shabani and D. A. Lidar, Phys. Rev. A **71**, 020101 (2005).

[88] A. Smirne and B. Vacchini, Phys. Rev. A **82**, 022110 (2010).

[89] A. Kolli, A. Nazir, and A. Olaya-Castro, J. Chem. Phys. **135**, 154112 (2011).

[90] U. Kleinekathöfer, J. Chem. Phys. **121**, 2505 (2004).

[91] P. H. Berens, S. R. White, and K. R. Wilson, J. Chem. Phys. **75**, 515 (1981).

[92] E. J. Candes, J. Romberg, and T. Tao, IEEE Trans. Inform. Theory **52**, 489 (2006).

[93] X. Andrade, J. N. Sanders, and A. Aspuru-Guzik, Proc. Natl. Acad. Sci. **109**, 13928 (2012).

[94] J. N. Sanders, S. K. Saikin, S. Mostame, X. Andrade, J. R. Widom, A. H. Marcus, and A. Aspuru-Guzik, J. Phys. Chem. Lett. **3**, 2697 (2012).

[95] W. D. Cornell, P. Cieplak, C. I. Bayly, I. R. Gould, K. M. Merz, D. M. Ferguson, D. C. Spellmeyer, T. Fox, J. W. Caldwell, and P. A. Kollman, J. Am. Chem. Soc. **117**, 5179 (1995).

[96] M. Ceccarelli, P. Procacci, and M. Marchi, J. Comput. Chem. **24**, 129 (2003).

[97] A. D. Becke, Phys. Rev. A **38**, 3098 (1988).

[98] B. Miehlich, A. Savin, H. Stoll, and H. Preuss, Chem. Phys. Lett. **157**, 200 (1989).

[99] C. Lee, W. Yang, and R. G. Parr, Phys. Rev. B **37**, 785 (1988).

[100] Y. Shao, L. F. Molnar, Y. Jung, J. Kussmann, C. Ochsenfeld, S. T. Brown, A. T. Gilbert, L. V. Slipchenko, S. V. Levchenko, and D. P. O'Neill, Phys. Chem. Chem. Phys. **8**, 3172 (2006).

[101] G. D. Scholes, G. R. Fleming, L. X. Chen, A. Aspuru-Guzik, A. Buchleitner, D. F. Coker, G. S. Engel, R. van Grondelle, A. Ishizaki, D. M. Jonas, J. S. Lundeen, J. K. McCusker, S. Mukamel, J. P. Ogilvie, A. Olaya-Castro, M. A. Ratner, K. B. Spano, Frank C aknd Whaley, and X. Zhu, Nature **543**, 647 (2017).

[102] G. D. Scholes, G. R. Fleming, A. Olaya-Castro, and R. van Grondelle, Nat. Chem. **3**, 763 (2011).

[103] J. R. Caram, N. H. C. Lewis, A. F. Fidler, and G. S. Engel, J. Chem. Phys. **136**, 104505 (2012).

[104] T. P. J. Kruger and R. van Grondelle, Phys. B: Phys. Cond. Mat. **480**, 7 (2016).

[105] F. Muh, M. E.-A. Madjet, J. Adolphs, A. Abdurahman, B. Rabenstein, H. Ishikita, E.-W. Knapp, and T. Renger, Proc. Natl Acad. Sci. **104**, 16862 (2007).

[106] E. Romero, R. Augulis, V. I. Novoderezhkin, M. Ferretti, J. Thieme, D. Zigmantas, and R. van Grondelle, Nat. Phys. **10**, 676 (2014).

[107] A. W. Chin, J. Prior, R. Rosenbach, F. Caycedo-Soler, S. F. Huelga, and M. B. Plenio, Nat. Phys. **9**, 113 (2013).

[108] C. Kreisbeck and T. Kramer, J. Phys. Chem. Lett. **3**, 2828 (2012).

[109] A. Kolli, E. J. O'Reilly, G. D. Scholes, and A. Olaya-Castro, J. Chem. Phys. **137**, 174109 (2012).

[110] V. Perlik, J. Seibt, L. J. Cranston, R. J. Cogdell, C. N. Lincoln, J. Savolainen, F. Sanda, T. Mancal, and J. Hauer, J. Chem. Phys. **142**, 212434 (2015).

[111] F. Novelli, A. Nazir, G. H. Richards, A. Roozbeh, K. E. Wilk, P. M. G. Curmi, and J. A. Davis, J. Phys. Chem. Lett. **6**, 4573 (2015).

[112] A. Marin, A. B. Doust, G. D. Scholes, K. E. Wilk, P. M. Curmi, I. H. van Stokkum, and R. van Grondelle, Biophys. J. **101**, 1004 (2011).

[113] T. Mirkovic, A. B. Doust, J. Kim, K. E. Wilk, C. Curutchet, B. Mennucci, R. Cammi, P. M. G. Curmi, and G. D. Scholes, Photochem. Photobiol. Sci. (2007).

[114] V. I. Novoderezhkin, M. A. Palacios, H. van Amerongen, and R. van Grondelle, J. Phys. Chem. B **108**, 10363 (2004).

[115] S. Shim, P. Rebentrost, S. Valleau, and A. Aspuru-Guzik, Biophys. J. **102**, 649 (2012).

[116] L. Viani, M. Corbella, C. Curutchet, E. J. O'Reilly, A. Olaya-Castro, and B. Mennucci, Phys. Chem. Chem. Phys. **16**, 16302 (2014).

[117] C. Olbrich, J. Strumpfer, K. Schulten, and U. Kleinekathofer, J. Phys. Chem. Lett. **2**, 1771 (2011).

[118] A. M. Rosnik and C. Curutchet, J. Chem. Theory Comput. **11**, 5826 (2015).

[119] H. Pengfei and D. F. Coker, J. Phys. Chem. Lett. **2**, 825 (2011).

[120] G. R. Fleming and M. Cho, Annual Review of Physical Chemistry (1996).

[121] M. Aghtar, U. Kleinekathofer, C. Curutchet, and B. Mennucci, J. Phys. Chem. B **121**, 1330 (2017).

[122] M. K. Lee and D. F. Coker, J. Phys. Chem. Lett. **7**, 3171 (2016).

[123] M. O. Sinnokrot and C. D. Sherrill, J. Chem. Phys. **115**, 2439 (2001).

[124] C. T. Falzon, D. P. Chong, and F. Wang, J. Comput. Chem. **27**, 163 (2005).

[125] A. D. Laurent, C. Adamo, and D. Jacquemin, Phys. Chem. Chem. Phys. **16**, 14334 (2014).

[126] R. Send, M. Kuhn, and F. Furche, J. Chem. Theory Comput. **7**, 2376 (2011).

[127] C. Kreisbeck and A. Aspuru-Guzik, Chem. Sci. **7**, 4174 (2016).

[128] J. Strumpfer and K. Schulten, J. Chem. Phys. **131**, 225101 (2009).

[129] H. Sumi, J. Phys. Chem. B **103**, 252 (1999).

[130] G. D. Scholes and G. R. Fleming, The Journal of Physical Chemistry B **104**, 1854 (2000).

[131] S. Jang, M. D. Newton, and R. J. Silbey, Phys. Rev. Lett. **92**, 218301 (2004).

[132] T. Mirkovic, E. E. Ostroumov, J. M. Anna, R. van Grondelle, Govindjee, and G. D. Scholes, Chem. Rev. **117**, 249 (2017).

[133] V. Novoderezhkin, A. Marin, and R. van Grondelle, Phys. Chem. Chem. Phys. **13**, 17093 (2011).

[134] D. I. G. Bennett, K. Amarnath, and G. R. Fleming, J. Am. Chem. Soc. **135**, 9164 (2013).

[135] G. Raszewski and T. Renger, J. Am. Chem. Soc. **130**, 4431 (2008).

[136] K. Amarnath, D. I. G. Bennett, A. R. Schneider, and G. R. Fleming, Proc. Natl Acad. Sci. **113**, 1156 (2016).

[137] T. Forster, in *Modern quantum chemistry. Istanbul lectures. Part III: Action of light and organic crystals*, edited by O. Sinanoglu (New York and London: Academic Press, 1965) pp. 93–137.

[138] G. R. Fleming and M. Cho, Ann. Rev. Phys. Chem. **47**, 109 (1996).

[139] X. J. Jordanides, M. J. Lang, X. Song, and G. R. Fleming, J. Phys. Chem. B **103**, 7995 (1999).

[140] A. Ishizaki, T. R. Calhoun, G. S. Schlau-Cohen, and G. R. Fleming, Phys. Chem. Chem. Phys. **12**, 7319 (2010).

[141] Y. Fujihashi, G. R. Fleming, and A. Ishizaki, J. Chem. Phys. **142**, 212403 (2015).

[142] M. C. So, G. P. Wiederrecht, J. E. Mondloch, J. T. Hupp, and O. K. Farha, Chem. Commun. **51**, 3501 (2015).

[143] E. A. Hemmig, C. Creatore, B. Wunsch, L. Hecker, P. Mair, M. A. Parker, S. Emmott, P. Tinnefeld, U. F. Keyser, and A. W. Chin, Nano Lett. **16**, 2369 (2016).

[144] C. Kreisbeck, T. Kramer, M. Rodriguez, and B. Hein, J. Chem. Theory Comput. **7**, 2166 (2011).

[145] A. G. Dijkstra, C. Wang, J. Cao, and G. R. Fleming, J. Phys. Chem. Lett. **6**, 627 (2015).

[146] S. J. Harrop, K. E. Wilk, R. Dinshaw, E. Collini, T. Mirkovic, C. Y. Teng, D. G. Oblinsky, B. R. Green, K. Hoef-Emden, R. G. Hiller, G. D. Scholes, and P. M. G. Curmi, Proc. Natl Acad. Sci. **111**, E2666 (2014).

[147] R. B. D.A. Case and P. Kollman, FIXME!!!!!!!! (2016).

[148] M. Valiev, E. J. Bylaska, N. Govind, and K. Kowalski, Comput. Phys. **181**, 1477 (2010).

[149] U. C. Singh and P. A. Kollman, J. Comput. Chem. **7**, 718 (1986).

[150] C. Lee, W. Yang, and R. G. Parr, Phys. Rev. B **37**, 785 (1988).

[151] A. D. Becke, J. Chem. Phys. **98**, 5648 (1993).

[152] P. J. Stephens, F. J. Devlin, and C. F. Chabalowski, J. Phys. Chem. **98** (1994).

[153] H. J. C. Berendsen, J. P. M. Postma, W. F. van Gunsteren, A. DiNola, and J. R. Haak, J. Chem. Phys. **81**, 3684 (1984).

[154] T. Morishita, J. Chem. Phys. **113**, 2976 (2000).

[155] T. Mancal and L. Valkunas, New J. Phys **12**, 065044 (2010).

[156] F. Fassioli, A. Olaya-Castro, and G. D. Scholes, J. Phys. Chem. Lett. **3**, 3136 (2012).

[157] K. M. Pelzer, T. Can, S. K. Gray, D. K. Morr, and G. S. Engel, J. Phys. Chem. B **118**, 2693 (2014).

[158] A. Ishizaki and G. R. Fleming, Proc. Natl. Acad. Sci. **106**, 17255 (2009).

[159] G. D. Scholes, G. R. Fleming, A. Olaya-Castro, and R. van Grondelle, Nat. Chem. **3**, 763 (2011).

[160] A. Halpin, P. J. M. Johnson, R. Tempelaar, R. S. Murphy, J. Knoester, T. L. C. Jansen, and R. J. D. Miller, Nat. Chem. **6**, 196 (2014).

[161] E. Collini, C. Y. Wong, K. E. Wilk, P. M. G. Curmi, P. Brumer, and G. D. Scholes, Nature **463**, 644 (2010).

[162] S. M. Blau, D. I. G. Bennett, C. Kreisbeck, G. D. Scholes, and A. Aspuru-Guzik, arXiv.org (2017), 1704.05449v1 .

[163] A. Halpin, P. J. M. Johnson, and R. J. D. Miller, Science **344**, 1099 (2014).

[164] J. B. Foresman, M. Head-Gordon, J. A. Pople, and M. J. Frisch, J. Phys. Chem. **96**, 135 (1992).

[165] Y. M. Rhee and M. Head-Gordon, J. Phys. Chem. A **111**, 5314 (2007).

[166] C.-P. Hsu, Z.-Q. You, and H.-C. Chen, J. Phys. Chem. C **112**, 1204 (2008).

[167] D. Hayes, G. B. Griffin, and G. S. Engel, Science **344**, 1099 (2014).

[168] A. Dreuw and M. Head-Gordon, Chem. Rev. **105**, 4009 (2005).

[169] S. Jurinovich, L. Viani, C. Curutchet, and B. Mennucci, Phys. Chem. Chem. Phys. **17**, 30783 (2015).

[170] A. V. Akimov and O. V. Prezhdo, J. Phys. Chem. Lett. **4**, 3857 (2013).

[171] T. J. Zuehlsdorff, P. D. Haynes, F. Hanke, M. C. Payne, and N. D. M. Hine, J. Chem. Theory Comput. **12**, 1853 (2016).

[172] B. Lunkenheimer and A. Kohn, J. Chem. Theory Comput. **9**, 977 (2013).

[173] I. H. Nayyar, E. R. Batista, S. Tretiak, A. Saxena, D. L. Smith, and R. L. Martin, J. Phys. Chem. Lett. **2**, 566 (2011).

[174] C. Kreisbeck, T. Kramer, and A. Aspuru-Guzik, J. Phys. Chem. B **117**, 9380 (2013).

[175] G. A. Lott, A. Perdomo-Ortiz, J. K. Utterback, J. R. Widom, A. Aspuru-Guzik, and A. H. Marcus, Proc. Natl Acad. Sci. **108**, 16521 (2011).

[176] L. A. Pachon, A. H. Marcus, and A. Aspuru-Guzik, J. Chem. Phys. **142**, 212442 (2015).

[177] J. Yuen-Zhou, J. J. Krich, M. Mohseni, and A. Aspuru-Guzik, Proc. Natl Acad. Sci. **108**, 17615 (2011).

[178] J. Yuen-Zhou, D. H. Arias, D. M. Eisele, C. P. Steiner, J. J. Krich, M. G. Bawendi, K. A. Nelson, and A. Aspuru-Guzik, ACS Nano **8**, 5527 (2014).

[179] M. D. Hanwell, D. E. Curtis, D. C. Lonie, T. Vandermeersch, E. Zurek, and G. R. Hutchison, Journal of Cheminformatics **4**, 17 (2012).

[180] A. K. Rappe, C. J. Casewit, K. S. Colwell, W. A. Goddard, and W. M. Skiff, J. Am. Chem. Soc. **114**, 10024 (1992).

[181] J. P. Perdew, K. Burke, and M. Ernzerhof, Phys. Rev. Lett. **77**, 3865 (1996).

[182] W. L. Jorgensen and J. Tirado-Rives, J. Am. Chem. Soc. **110**, 1657 (1988).

[183] W. L. Jorgensen, D. S. Maxwell, and J. Tirado-Rives, J. Am. Chem. Soc. **118**, 11225 (1996).

[184] A. Laio, J. VandeVondele, and U. Rothlisberger, J. Chem. Phys. **116**, 6941 (2002).

[185] P. J. Berryman, D. A. Faux, and D. J. Dunstan, Phys. Rev. B **76**, 104303 (2007).

[186] R. C. Rizzo and W. L. Jorgensen, J. Am. Chem. Soc. **121**, 4827 (1999).

[187] W. L. Jorgensen and P. Schyman, J. Chem. Theory Comput. **8**, 3895 (2012).

[188] K. Kahn and T. C. Bruice, J. Comput. Chem. **23**, 977 (2002).

[189] R. Car and M. Parrinello, Phys. Rev. Lett. **55**, 2471 (1985).

[190] C. Braga and K. P. Travis, J. Chem. Phys. **123**, 134101 (2005).

[191] Y. Shao, Z. Gan, E. Epifanovsky, A. T. Gilbert, M. Wormit, J. Kussmann, A. W. Lange, A. Behn, J. Deng, X. Feng, D. Ghosh, M. Goldey, P. R. Horn, L. D. Jacobson, I. Kaliman, R. Z. Khaliullin, T. Ku, A. Landau, J. Liu, E. I. Proynov, Y. M. Rhee, R. M. Richard, M. A. Rohrdanz, R. P. Steele, E. J. Sundstrom, H. L. W. III, P. M. Zimmerman, D. Zuev, B. Albrecht, E. Alguire, B. Austin, G. J. O. Beran, Y. A. Bernard, E. Berquist, K. Brandhorst, K. B. Bravaya, S. T. Brown, D. Casanova, C.-M. Chang, Y. Chen, S. H. Chien, K. D. Closser, D. L. Crittenden, M. Diedenhofen, R. A. D. Jr., H. Do, A. D. Dutoi, R. G. Edgar, S. Fatehi, L. Fusti-Molnar, A. Ghysels, A. Golubeva-Zadorozhnaya, J. Gomes, M. W. Hanson-Heine, P. H. Harbach, A. W. Hauser, E. G. Hohenstein, Z. C. Holden, T.-C. Jagau, H. Ji, B. Kaduk, K. Khistyaev, J. Kim, J. Kim, R. A. King, P. Klunzinger, D. Kosenkov, T. Kowalczyk, C. M. Krauter, K. U. Lao, A. D. Laurent, K. V. Lawler, S. V. Levchenko, C. Y. Lin, F. Liu, E. Livshits, R. C. Lochan, A. Luenser, P. Manohar, S. F. Manzer, S.-P. Mao, N. Mardirossian, A. V. Marenich, S. A. Maurer, N. J. Mayhall, E. Neuscamman, C. M. Oana, R. Olivares-Amaya, D. P. ONeill, J. A. Parkhill, T. M. Perrine, R. Peverati, A. Prociuk, D. R. Rehn, E. Rosta, N. J. Russ, S. M. Sharada, S. Sharma, D. W. Small, A. Sodt, T. Stein, D. Stück, Y.-C. Su, A. J. Thom, T. Tsuchimochi, V. Vanovschi, L. Vogt, O. Vydrov, T. Wang, M. A. Watson, J. Wenzel, A. White, C. F. Williams, J. Yang, S. Yeganeh, S. R. Yost, Z.-Q. You, I. Y. Zhang, X. Zhang, Y. Zhao, B. R. Brooks, G. K. Chan, D. M. Chipman, C. J. Cramer, W. A. G. III, M. S. Gordon, W. J. Hehre, A. Klamt, H. F. S. III, M. W. Schmidt, C. D. Sherrill, D. G. Truhlar, A. Warshel, X. Xu, A. Aspuru-Guzik, R. Baer, A. T. Bell, N. A.

Besley, J.-D. Chai, A. Dreuw, B. D. Dunietz, T. R. Furlani, S. R. Gwaltney, C.-P. Hsu, Y. Jung, J. Kong, D. S. Lambrecht, W. Liang, C. Ochsenfeld, V. A. Rassolov, L. V. Slipchenko, J. E. Subotnik, T. V. Voorhis, J. M. Herbert, A. I. Krylov, P. M. Gill, and M. Head-Gordon, Mol. Phys. **113**, 184 (2015).

[192] F. Weigend, M. Haser, H. Patzelt, and R. Ahlrichs, Chem. Phys. Lett. **294**, 143 (1998).

[193] F. Weigend, A. Kohn, and C. Hattig, J. Chem. Phys. **116**, 3175 (2002).

[194] J. Hausinger and M. Grifoni, Phys. Rev. A **81**, 022117 (2010).

[195] M. Thorwart, L. Hartmann, I. Goychuk, and P. Hänggi, J. Mod. Op. **47**, 2905 (2000).

[196] A. Garg, J. N. Onuchic, and V. Ambegaokar, J. Chem. Phys. **83**, 4491 (1985)

This thesis was typeset using LaTeX, which was originally developed by Leslie Lamport and based on Donald Knuth's TeX. The body text is set in 12 point Latin Modern font. A template that can be used to format a dissertation with a similar look & feel is available at http://dissertate.io/.